Università degli Studi di Palermo

dipartimento di ingegneria unipa

PhD Mechanical, Manufacturing, Management and Aerospace Innovation (M3AI)

Department of Engineering (DI)

MODELING OF TRANSCATHETER AORTIC VALVE INTERVENTION

IL DOTTORE

ENG. CHIARA CATALANO

IL COORDINATORE

CH.MA PROF. GIOVANNA LO NIGRO

IL TUTOR

CH.MO PROF. SALVATORE PASTA

CYCLE XXXVII

ACADEMIC YEAR 2023-2024

Abstract

Transcatheter aortic valve implantation (TAVI) has revolutionized the management of aortic valve diseases, providing a minimally invasive option for patients who are ineligible for open-heart surgery. Since its inception, TAVI has undergone significant advancements, extending its use to patients with intermediate and low surgical risk. However, the procedure is not devoid of risks, as complications such as paravalvular leakage, conduction disturbances, coronary obstruction, and structural valve deterioration can occur, potentially leading to fatal consequences.

To address these challenges, this thesis focuses on the development of high-fidelity, patient-specific computational models capable of predicting the structural and hemodynamic performance of TAVI and its associated risks across various clinical scenarios. The modeling workflow was designed in compliance with the Verification, Validation, and Uncertainty Quantification (VVUQ) framework outlined by the ASME V&V 40-2018 standard, ensuring that the developed numerical model is sufficiently credible for clinical applications. The computational platform integrates finite element analysis (FEA) for structural simulation and fluid-structure interaction (FSI) for hemodynamic assessment, simulating the TAVI procedure and its biomechanical interaction with patient-specific anatomy. Advanced material calibration techniques were employed to accurately replicate the mechanical properties of native tissues of the investigated patient population, and a parametric modeling approach based on anatomical landmarks was used to reconstruct native valve leaflets. Validation of the patient-specific TAVI models against clinical data revealed a high correlation between model predictions and clinical outcomes, confirming the accuracy of the model in predicting key parameters such as valve orifice area, pressure gradients, and stent deformation.

In addition to in-silico modeling, experimental methods such as 3D printing and Particle Image Velocimetry (PIV) were employed to investigate the role of transcatheter aortic valves (TAVs) in complex clinical scenarios, including transcatheter mitral valve replacement (TMVR) and valve-in-valve procedures. These investigations yielded critical insights into procedural success. For instance, TMVR models highlighted the importance of dynamic variations in the estimated neo-left ventricular outflow tract (neo-LVOT) area throughout the cardiac cycle, and how these variations are influenced by patient anatomy and procedural factors such as implantation depth, annular stiffness, and calcification degree. By accounting

for these variables, these models can help clinicians in optimizing device selection and procedural planning, improving patient-specific outcomes.

Overall, the computational platform developed in this thesis, in conjunction with experimental techniques, offers a robust tool for enhancing the safety and efficacy of TAVI procedures and supporting the development of next-generation TAVI devices. This work advances the field of personalized medicine by offering a reliable *in-silico* tool that can assist traditional clinical assessments and accelerates the development and optimization of new heart valve technologies.

Acknowledgments

This project has received funding from the European Union's Horizon 2020 research and innovation program under grant agreement No 101017523.

Contents

Nomenclature 10
List of Figures 12
List of Tables 15
Introduction 16
Clinical Background 18
2.1 The aortic valve and root: anatomy and hemodynamic 18
2.2 Aortic valve diseases 19
2.3 Diagnosis and therapeutic alternatives 21
2.3.1 Diagnostic tools 21
2.3.2 Treatment options for aortic valve diseases 22
2.4 Transcatheter aortic valve implantation 24
State of the art 28
3.1 Computational approaches 28
3.1.1 TAVI FEA models 28
3.1.2 CFD TAVI models 29
3.2 Challenging TAVI scenarios 30
3.2.1 Life-threatening complications 30
3.2.2 Emerging and specialized applications 31
3.3 VVUQ standard 32
3.4 Conclusions 34
Patient-specific benchmark TAVI model 35
4.1 Study population 35
4.2 Patient-specific model platform development 37
4.3 S3 device and delivery models 39
4.4 TAVI Integration 41
4.5 Discussion 45
Patient-specific material calibration 46
5.1 FEA of pre-TAVI scenario 46
5.2 Inverse Analysis 48
5.3 Results for the aortic wall 49
5.4 Results for the calcified aortic valve 51
5.6 Discussion 52
5.7 Challenges and Future Directions 53
Verification and validation of high-fidelity TAVI computational models 54
6.1 V&V Requirements 54

6.2 Case study 1: patient-specific TAVI structural model 57
6.2.1 Apply the ASME V&V 40 Framework 57
6.2.2 Discretization error assessment 58
6.2.3 Numerical solver error assessment 59
6.2.4 Numerical Code Verification 60
6.3 Case study: patient-specific TAVI SPH models 61
6.3.1 Patient-specific FSI TAVI model description 61
6.3.2 Model output of interest 64
6.3.3 Apply the ASME V&V 40 Framework 65
6.3.4 Results 66
6.4 Discussion 70
6.5 Challenges and Future Directions 71
Transcatheter mitral valve replacement simulations 72
7.1 Background and Challenges 72
7.2 Modeling TMVR 74
7.3 Case study 1: In-silico and in-vitro assessment of neo-LVOT area in ViR, ViV and ViMAC 74
7.3.1 Patient study population 75
7.3.2 Patient-specific model 75
7.3.3 Band ring, bioprosthesis and Sapien 3 Ultra models 77
7.3.4 Simulation of TMVR procedures 78
7.3.5 3D Printing 79
7.3.6 Results and findings 80
7.4 Case study 2: Valve-in-Ring TMVR procedure with LHHM 82
7.4.1 LHHM Adaptation 82
7.4.2 Band ring and Sapien 3 Ultra models 84
7.4.3 Simulation of TMVR procedure 84
7.4.4 Results 85
7.5 Discussion 86
7.6 Limitations 89
Particle Image Velocimetry Analysis in valve-in-MHV 91
8.1 Introduction 91
8.2 Pulse duplicator system 92
8.3 Backlight PIV 94
8.4 Results 95
8.4 Discussion 97
Conclusions and Outlook 99

List of Publications..... 102
Appendix..... 104
Bibliography..... 108

Nomenclature

Abbreviations

AML	Anterior Mitral Leaflet
AR	Aortic Regurgitation
AS	Aortic Stenosis
AV	Aortic Valve
AVA	Aortic Valve Area
ASME	American Society of Mechanical Engineering
BAV	Bicuspid Aortic Valve
BHV	Biological Heart Valve
BMF	Blood-Mimicking Fluid
BMHV	Bileaflet Mechanical Heart Valve
CAD	Computer-Aided Design
CAVD	Calcific Aortic Valve Disease
CCT	Cardiac Computed Tomography
CFD	Computational Fluid Dynamics
Co-Cr	Chromium-Cobalt
CoU	Context of Use
DAQ	Data Acquisition
DE	Discretization Error
DVI	Doppler Velocity Index
ECDF	Empirical Cumulative Distribution Function
EOA	Effective Orifice Area
FEA	Finite Element Analysis
FEM	Finite Element Method
FSI	Fluid Structure Interaction
GAG	Glycosaminoglycan
GOA	Geometric Orifice Area
LCC	Left-Coronary Cusp
LDL	Low-Density Lipoproteins
LHHM	Living Heart Human Model
LV	Left Ventricle
LVDT	Linear Variable Differential Transformer
LVOT	Left Ventricular Outflow
MAC	Mitral Annular Calcification
MHV	Mechanical Heart Valve
MR	Mitral Regurgitation
MRI	Magnetic Resonance Imaging
MV	Mitral Valve
NCC	Non-Coronary Cusp
NCV	Numerical Code Verification
Ni-Ti	Nitinol
NSE	Numerical Solver Error
PE	Polyethylene
PET	Polyethylene Terephthalate
PG	Pressure Gradient
PIV	Particle Image Velocimetry
PPI	Permanent Pacemaker Implantation
PPM	Prosthesis-Patient Mismatch
PVL	Paravalvular Leakage

PTV	Particle Tracing Velocimetry
QoI	Question of Interest
RBP	Rated Burst Pressure
RCC	Right-Coronary Cusp
RE	Relative Error
RF	Regurgitant Fraction
RI	Refractive Index
RSS	Reynolds Shear Stress
S3 ULTRA	Sapien 3 ULTRA
SA	Sensitivity Analysis
SAVR	Surgical Aortic Valve Replacement
SJM	St. Jude Medical
SLA	Stereolithography
SPH	Smoothed Particle Hydrodynamics
STJ	Sinotubular junction
STL	STereo Lithography interface format
SV	Stroke Volume
TAVI	Transcatheter Aortic Valve Implantation
TAV	Transcatheter Aortic Valve
TEE	Transesophageal Echocardiography
TEHV	Tissue Engineered Heart Valve
THV	Transcatheter Heart Valve
TKE	Turbulent Kinetic Energy
TMVR	Transcatheter Mitral Valve Replacement
TTE	Transthoracic Echocardiography
UQ	Uncertainty Quantification
V&V	Verification & Validation
VIC	Valve Interstitial Cell
ViMAC	Valve-in-MAC
ViR	Valve-in-Ring
ViV	Valve-in-Valve
VTI	Velocity-Time Integral
VVUQ	Verification, Validation, and Uncertainty Quantification

List of Figures

Figure 2.1. Schematic and histologic section of an aortic valve leaflet and its layers. With permission from Chin et al. (2023).

Figure 2.2. Aortic valve and root detected from CT in axial (A) and coronal (B) view.

Figure 2.3. Currently available mechanical and biological valves. With permission from Rajiah et al. (2019).

Figure 2.4. Commercially available transcatheter heart valves. With permission from Vinayak et al. (2024).

Figure 3.1. V&V workflow. Reprinted from ASME V&V 40-2018, by permission of The American Society of Mechanical Engineers. All rights reserved.

Figure 4.1 Patient-specific platform for TAVI integration.

Figure 4.2. Residual stress distribution of the aortic wall with supraphysiological (left) and physiological (right) material properties.

Figure 4.3 A) Real S3 Ultra device (left) and S3 Ultra numerical model (right).

Figure 4.4. Implantation view and device positioning with the centre marker. With permission from Kronzon et al. (2015).

Figure 4.5. Representation of the balloon axis and coordinate system orientation with respect to stenotic valve leaflets.

Fig. 4.6. Simulation workflow for the three-step TAVI simulation process.

Figure 4.7. Deformed configuration of calcified valve, S3 frame, and balloon after crimping, recoil and implantation.

Figure 4.8. Simulation results from SIM-2 showing the undeformed (left) and deformed (right) S3 frame with skirt and valve leaflets.

Figure 4.9. Undeformed (left) and actual (right) configuration resulted from SIM-3.

Figure 5.1. Pressure waveform employed for the development of patient-specific pressure boundary conditions.

Figure 5.2. Grasshopper algorithm for orifice valve area estimation.

Figure 5.3. Comparison of peak systolic configuration between predictions and CT imaging for each patient and corresponding Jaccard index.

Figure 5.4. Pearson's analysis between optimized Young's moduli and CT-derived strain measurements.

Figure 5.5. Qualitative assessment of the level of agreement between predicted and actual pre-TAVI configuration.

Figure 5.6. Pearson's analysis between optimized Young's moduli and CT-derived valve orifice area measurements.

Figure 5.7. Bar chart of minimum (1) and maximum (2) S3 diameters at inflow, midflow and outflow derived from simulation results and CT imaging (left). CT scans showing the location of the measurements (right).

Figure 6.1. investigated element type (left) and orifice area comparison between the investigated typology and the real CT measurements.

Figure 6.2. comprehensive patient-specific SPH TAVI model workflow.

Figure 6.3. Solid mesh of aorta and reservoirs and particle distribution (left); Patient- specific TAVI SPH full model (right).

Figure 6.4. Physiological pressure and flow rate waveforms derived from patient-specific clinical data.

Figure 6.5. GOA computed over time.

Figure 6.6. Flow velocities for a representative patient case at A) acceleration, B) systole,

C) deceleration and D) diastole phases.

Figure 6.7. Empirical CDF plots for both the actual measurements and the predictions of

(A) EOA, (B) peak PG, (C) mean PG, (D) inflow diameter, (E) midflow diameter and (F) outflow diameter.

Figure 6.8. Predictions probability confidence against associated REs computed among the different variables.

Figure 7.1. LVOT narrowing process following THV implantation in mitral position. With permission from Blanke et al. (2017).

Figure 7.2. Sagittal view of LVOT obstruction and its neo-LVOT area for three TMVR patients with ViR, ViV and ViMAC.

Figure 7.3. Neo-LVOT area fluctuations over an entire cardiac beat for three representative cases of ViMAC, ViR and ViV.

Figure 7.4. Blood pressure map at end-systolic phase with computed pressure drops across the LVOT for three representative cases.

Figure 7.5. 3D printed models and related CT imaging of the left heart for the patient with ViR.

Figure 7.6. LHHM system and views of the mitral valve, chordae and ischemic region.

Figure 7.7. Contact pressure and area over an entire cardiac beat exerted on A) bad ring and B) MV.

Figure 7.8. Blood flow velocity and pressure distribution at end-systole showing subaortic flow stenosis in the neo-LVOT with the drop computed across neo-LVOT area.

Figure 8.1. Schematic view of the pulse duplicator and backlight PIV systems.

Figure 8.2. Phase-averaged velocity distribution for the SJM MHV, CoreValve THV and valve-in-MHV at CO=5 L/min.

Figure 8.3. From left, TKE, RSS, velocity vectors and vorticity contours at 5L/min for SJM MHV, CoreValve and valve-in-MHV configurations.

List of Tables

Table II. Inflation parameters for the S3 device with different diameters. Table III. Credibility factors and associated level of rigor employed.

Table IV. Baseline reference simulation main parameters.

Table V. Particle discretization and material properties of the fluid domain.

Table VI. Simulations run for NSE assessments and outputs of interest with related REs. Table VII. Output of interest and corresponding area metric (M).

Table VIII. Demographic data, device size and post-TMVR measurement of neo-LVOT. Table IX. Material parameters adopted for the device, left atrium, aorta and calcifications. Table X. Material parameters adopted for mitral valve (MV) and left ventricle (LV).

Table XI. Material parameters for mitral valve (MV), left ventricle (LV) and ischemic region.

Table XII. Main hemodynamic parameters for the different valve configurations under various test conditions.

Chapter 1

Introduction

The treatment of aortic valve (AV) diseases has seen significant advancements over the past few decades with the introduction of transcatheter aortic valve implantation (TAVI). This procedure has revolutionized the management of aortic stenosis (AS) in the high-surgical risk patients, providing a less invasive alternative to surgical aortic valve replacement (SAVR). Since its first successful human application in 2002 [1], TAVI has rapidly evolved from an experimental procedure to a standard of care for a wide range of people, led by continuous technological and clinical advancements.

Despite its success, challenges persist, particularly in the areas of preprocedural planning, device selection, and post-operative outcomes. The complexity of patient cases, including those with severe calcifications, bicuspid aortic valves (BAV), or concomitant coronary artery disease, requires a more sophisticated approach for the preoperative planning and device optimization. In this context, computational modeling and in-vitro testing have emerged as critical tools in addressing these challenges, allowing for the simulation and analysis of various TAVI scenarios before the real clinical implementation.

This thesis aims to enhance the understanding of TAVI by integrating computational and experimental methodologies. By focusing on patient-specific modeling and verification and validation (V&V) activities application, this research seeks to improve the accuracy and reliability of TAVI models, ultimately contributing to better clinical outcomes and to possibly reduce the time-to-market linked to the commercialization of new valve devices.

In the framework of the Horizon 2020 project “SimInSitu”, the computational models resulted from this work will serve as a foundation for the development of a sophisticated in-silico platform for the short- and long-term prediction of in-situ tissue-engineered heart valves (TEHV). The goal is to overcome the limitations associated with traditional trial-and-error processes, which are challenging, costly, and time-consuming. By doing so, the project aims to develop reliable in-silico models to accelerate the development of new heart valve devices and facilitate their translation into clinical practice and market.

This research contributes to the growing body of knowledge in TAVI by introducing new approaches to improve the reliability of computational models and deepen the understanding of transcatheter therapies, with the ultimate goal of enhancing their overall efficacy.

Thesis Outline

Chapter 2 – Clinical background will provide a comprehensive overview of the structure and function of the aortic valve and the pathophysiology of aortic valve diseases.

Chapter 3 – State of the Art will review current methodologies in TAVI, highlighting key innovations in in-silico techniques.

Chapter 4 – Patient-specific benchmark TAVI model will describe the development process of the patient-specific TAVI platform which will be the subject of chapters 5 and 6.
Chapter 5 – Patient-specific material calibration will explore the technical aspects of material properties and their integration into patient-specific TAVI computational models.
Chapter 6 – Verification and validation of high-fidelity TAVI computational models will explore the methodologies used to verify and validate patient-specific structural and fluid dynamical TAVI models, emphasizing the importance of credibility assessment when informing clinical decision.

Chapter 7 – Transcatheter mitral valve replacement simulations will expand on the computational challenges and solutions associated with TMVR procedure, where the aortic THV is used in mitral position as “off-label” application.

Chapter 8 – Backlight particle image velocimetry analysis in valve-in-MHV will present experimental findings of a backlight PIV study, regarding the hemodynamic assessment of a valve-in-MHV intervention.

Chapter 9 – Conclusions and Outlook will summarize the key findings of the research and discuss potential future directions in the field of TAVI in-silico modeling.

Chapter 2

Clinical Background

The present chapter provides a comprehensive analysis of the anatomical and physiological aspects of the aortic valve (AV). Furthermore, it addresses its physiopathology and the diverse therapeutic alternatives, emphasizing transcatheter aortic valve implantation (TAVI) procedures to contextualize the experimental and computational analyses presented in Chapters 4-8.

2.1 The aortic valve and root: anatomy and hemodynamic

The aortic valve (AV), situated between the left ventricle and the aorta, plays a crucial role in regulating the flow of the systemic circulation, assuring the effective distribution of oxygenated blood throughout the whole body. It is composed of three semilunar cups, or leaflets, contained within a connective tissue sleeve. The aortic tissue comprises three distinct layers (Figure 2.1), i.e., the fibrosa, the spongiosa and the ventricularis. Specifically, the side adjacent to the aorta is termed the fibrosa and is the major fibrous layer within the belly of the leaflet. The layer covering the ventricular side of the valve is called the ventricularis, which is thinner and smooth and is composed of both collagen and elastin. The central portion of the valve, called the spongiosa, contains variable loose connective tissue, proteins, and glycosaminoglycans (GAGs) and is normally not vascularized [2].

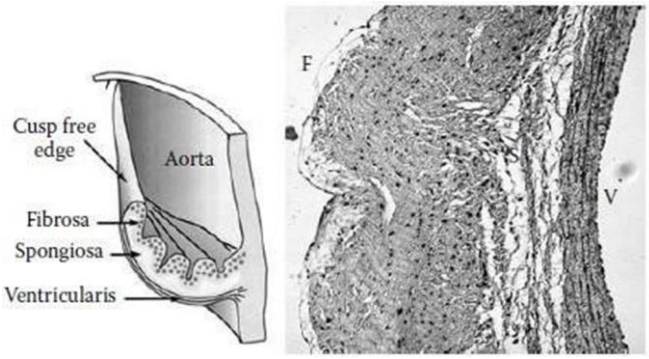

Figure 2.1. Schematic and histologic section of an aortic valve leaflet and its layers. With permission from Chin et al. (2023).

As shown in Figure 2.2, the aortic valve is located in the aortic root, which stretches from the base of the aortic valve cusps, i.e., the aortic annulus, to the sinotubular junction (STJ) where the ascending aorta starts. Small outpouchings of the aortic root, known as the sinuses of Valsalva, are situated behind each cusp. These sinuses are essential for the valve's opening and closing dynamic by facilitating vortex generation during systole, which forces the leaflets open, and by inhibiting leaflet attachment to the aortic wall during diastole [3].

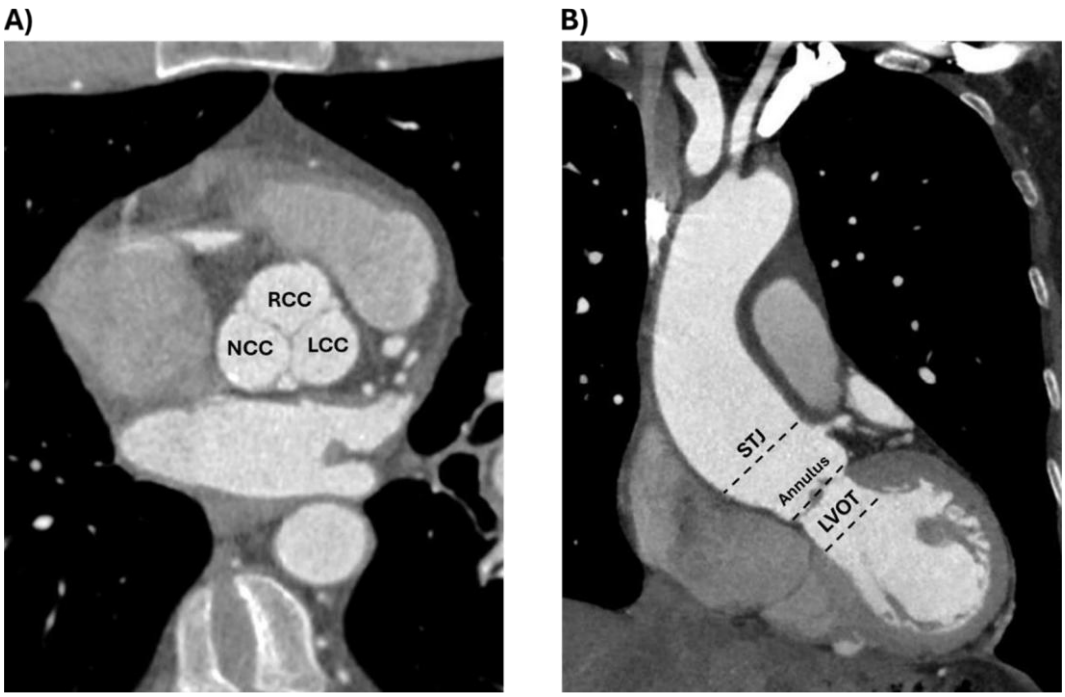

Figure 2.2. Aortic valve and root detected from CT in axial (A) and coronal (B) view. Note: RCC=right-coronary cusp; LCC=left-coronary cusp; NCC=non-coronary cusp.

During systole, the left ventricle contracts, increasing its pressure until it exceeds the pressure in the aorta, causing the aortic valve to open. Once the valve opens, the cusps are displaced outward toward the walls of the aorta, allowing the transit of blood from the left ventricle into the aorta. In diastole, when the valve closes, the cusps overlap slightly, forming a coaptation surface known as the lunula, which helps to ensure a tight seal and prevent backflow of blood into the ventricle. A vortical flow is generated into the sinus behind the valve cups before rejoining the mainstream in the ascending aorta. As anticipated by Leonardo Da Vinci and confirmed by in-vivo magnetic resonance [4], these vortices effecting partial reverse flow in the proximal aorta, would aid closure of the aortic valve in diastole by accommodating the increasing volume behind the valve cusps as they approach closure [5]. Aortic valves experience an exceptional workload, undergoing up to 100,000 cycles of opening and closing on a daily basis [6]. From a hemodynamic perspective, the aortic valve must stand significant pressures while controlling the passage of blood from the left ventricle into the aorta. Any perturbation in the structure or operation of the valve can cause hemodynamic imbalances which can give rise to a wide range of clinical disorders.

2.2 Aortic valve diseases

Considering the high frequency of operation of the AV, it is not unexpected that it becomes prone to deterioration with time, rendering it susceptible to conditions such as aortic stenosis (AS) and aortic regurgitation (AR), which significantly contribute to cardiovascular morbidity and mortality [7].

AS is the most prevalent valve disorder in Europe and North America, requiring surgery or transcatheter intervention. Its incidence is rapidly rising as a result of the rapidly aging population [8]. The predominant aetiology of AS is calcific degeneration. Primary clinical manifestations of AS involve dyspnea, angina, syncope and fatigue. The prognosis for untreated severe AS is unfavorable, with a mortality rate of up to 50% within the initial year of symptom occurrence, and over 90% within five years [9]. The calcific degeneration of the AV is considered an active, multifactorial process driven by mechanical stress, inflammation, and metabolic factors [10]. With this burden estimated to rise from 2.5 million in 2000 to 4.5 million in 2030, calcific aortic valve disease (CAVD) is the most prevalent valvular heart disease in the aging population [11]. This pathological process involves the progressive accumulation of calcium on the valve cusps, resulting in increased stiffness and compromised valve movement. Mechanical stresses, in conjunction with risk factors such as advanced age, male gender, diabetes, metabolic syndrome, hypertension, and renal disease, can contribute to endothelial damage in the aortic valve. The damage promotes the penetration of low-density lipoproteins (LDLs) into the fibrosa layer of the valve, leading to an inflammatory reaction, and resulting in the development of fibrosis in the valve tissue. In addition, inflammatory cells can cause an osteogenic change in valve interstitial cells (VICs), which leads to the production of calcium deposits in the valves [11, 12]. From a hemodynamic viewpoint, this calcification decreases the valve's opening area during systole, leading to an impairment of its capacity to effectively close during diastole. Consequently, this condition can result in elevated pressure gradients across the valves during systole and the backflow of blood into the left ventricle during diastole. In response to these abnormal hemodynamic conditions, the heart adapts by remodelling the myocardium, often resulting in ventricular hypertrophy. Without intervention, CAVD can eventually lead to heart failure. Bicuspid aortic valve (BAV) disease, the most common congenital heart defect, predisposes affected individuals to high rates and early onset of CAVD, aortic insufficiency, and ascending aorta and/or aortic root dilation compared to tricuspid aortic valve patients [13-16]. Inflammatory mechanisms, especially those linked to rheumatic heart disease, can also result in calcific degeneration. Under these circumstances, persistent inflammation and formation of scar tissue led to the gradual accumulation of calcium. Metabolic diseases such as chronic renal disease can lead to AV calcification by impairing the regulation of calcium and phosphate metabolism, therefore promoting calcification in the valve tissue [17].

In contrast, the phenomenon of regurgitation results in an augmented blood volume that the left ventricle is required to manage, therefore causing ventricular dilatation and a gradual decline in total cardiac efficiency. It imposes a persistent high-volume demand on the heart,

potentially leading to heart failure if not well controlled. Common clinical manifestations of AR include fatigue and diminished exercise capacity, palpitations, dyspnea, and signs of cardiac failure, such as persistent coughing and swelling [18].

2.3 Diagnosis and therapeutic alternatives

2.3.1 Diagnostic tools

Typically, the diagnosis of AV disorders requires a combination of clinical evaluation, imaging examinations, and, in certain cases, invasive procedures.

Thoracic auscultation is a crucial method to confirm the diagnosis of suspected heart valve dysfunction. It has been shown a correlation between the intensity of murmurs and AV diseases. While a diastolic murmur indicates AR, a systolic murmur denotes atrial AS [19]. Echocardiography is the gold standard for evaluating aortic valve diseases and providing prognostic information. It is essential for establishing the diagnosis and severity of AS, evaluating valve structure, left ventricular function, and wall thickness. Using Doppler techniques, echocardiography enables clinicians to measure blood flow velocity and assess valve kinematics by detecting the oscillation in frequency between emitted and reflected ultrasound signals. Transthoracic echocardiography (TTE) is the conventional non-invasive method used to get data on the direction, velocity, and kinematics of blood flow at the heart valve. Transesophageal echocardiography (TEE) provides higher-resolution images by precisely placing the ultrasound probe into the patient's esophagus, making it particularly valuable for pre-procedural planning [20].

AS severity is determined by evaluating the mean pressure gradient (PG), the peak transvalvular velocity, and aortic valve area (AVA) according to the current standards. AVA can be computed by solving the continuity equation. The procedure entails quantifying the diameter of the left ventricular outflow tract (LVOT) and determining the "velocity-time integral" (VTI) of both the LVOT and the AV [20]. A straightforward evaluation of severe AS can typically be made in presence of AVA smaller than 1 cm^2, a peak transvalvular velocity exceeding 4 m/s, and a mean PG greater than 40 mmHg. Nevertheless, when there is a discrepancy between the clinical observations and the usual standard criteria for severe AS assessment (e.g., AVA, peak velocity, or PG), clinical decision-making should incorporate additional parameters. These parameters encompass the patient's functional condition, stroke volume, Doppler velocity index (DVI), extent of valve calcification, left

ventricular function, presence or absence of left ventricular hypertrophy, and flow conditions.

In such complex scenarios, advanced imaging techniques as magnetic resonance imaging (MRI) and cardiac computed tomography (CCT) can provide crucial supplementary understanding. CCT, in particular, is valuable for assessing the degree of valve calcification, which can provide further information on the severity of AS and train the development of treatment strategies [8].

Although less commonly used today, cardiac catheterization can also still be employed when non-invasive imaging is inconclusive. This technology enables the direct measurement of PGs across the aortic valve, therefore providing accurate hemodynamic data [21].

Upon assessment of stenosis as "severe", it is imperative to contemplate clinical intervention. The selection of therapy is contingent upon the medical status of the patient, which should be evaluated in accordance with recognized professional standards. The guidelines recommend that patient-specific factors such as age, comorbidities, and surgical risk should be considered when determining the most appropriate intervention, which may include surgical aortic valve replacement (SAVR) or transcatheter aortic valve implantation (TAVI) [8]. Achieving the optimal outcome for the patient requires a patient-centered and multidisciplinary decision-making process that includes cardiologists, cardiothoracic surgeons, and other specialists.

2.3.2 Treatment options for aortic valve diseases

The therapeutic strategy for aortic valve disorders is mostly influenced by the extent of the disease, the symptoms exhibited, and the patient's general health status and predisposing factors. The primary objective of clinical interventions for AS is to restore the functionality of the calcified native aortic valve. Notwithstanding continuous study, the existing drugs have not yet demonstrated the ability to prevent the initiation or advancement of AS, thereby establishing aortic valve replacement as the ultimate therapy for severe patients. In a successful procedure, the prosthetic valve efficiently replaces the dysfunctional valve, restoring normal hemodynamic within the heart. Heart valve prostheses, shown in Figure 2.3, are currently categorized based on the materials used in their realization: mechanical heart valves (MHVs) and biological heart valves (BHVs). MHVs are surgically implanted, while BHVs can be implanted either surgically or via minimally invasive transcatheter techniques.

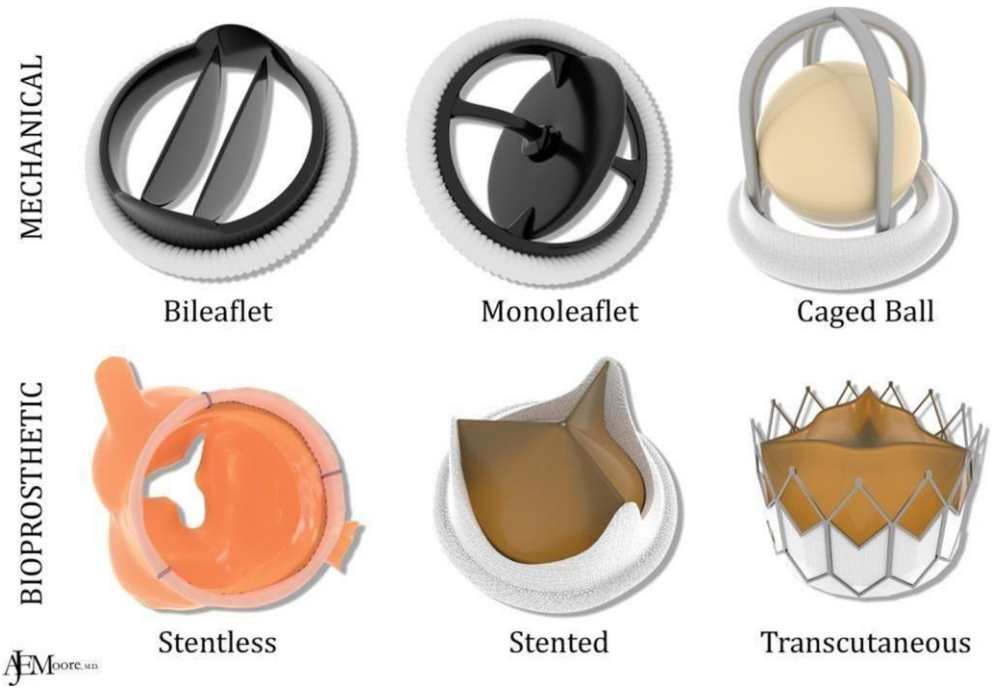

Figure 2.3. Currently available mechanical and biological valves. With permission from Rajiah et al. (2019).

MHVs are manufactured from durable materials like pyrolytic carbon and titanium, known for their long lifespan, often lasting 20 to 30 years, making them particularly suitable for younger patients. However, because of their ability to cause blood clot formation, patients with MHVs require lifelong anticoagulation therapy, typically with vitamin K antagonists as warfarin, to prevent these clots. Despite this therapy, there remains a strong risk of thromboembolism, which affects up to 4% of patients each year [23, 24].

BHVs are derived from biological tissues, usually obtained from bovine pericardium or porcine aortic valves. Therefore, the main benefit of BHVs is their reduced thrombogenicity, therefore obviating the necessity for prolonged anticoagulation treatment. Nevertheless, BHVs have a shorter lifespan compared to MHVs, often lasting 10 to 15 years. This is mostly attributed to the progressive degradation of the valves caused by calcification and tissue wear. As a result, BHVs are preferable for elderly individuals or those for whom the hazards linked to anticoagulation treatment are substantial [25].

Generally, both mechanical and biological heart valves are not devoid of difficulties. The issues related to prosthetic heart valves comprise structural valvular degradation, non-structural malfunction, valve thrombosis, embolism, bleeding and endocarditis.

These issues are thought to be linked to non-physiological blood flow patterns in proximity to cardiac valves. Indeed, the abnormal flow pattern has long been recognized for their potential to trigger thrombus formation [26]. Regions of high shear stress cause tearing of the blood elements, thus possibly leading to hemolysis and platelet activation. Recirculation

and flow stagnation regions increase the exposure time between blood elements, in particular activated platelets, thereby promoting thrombus formation.

Historically, SAVR has been the fundamental therapy for severe aortic valve disease. The therapeutic intervention entails invasive open-heart surgery, wherein the patient is placed under general anaesthesia and the heart is accessible via a thoracotomy. A cardiopulmonary bypass, facilitated by a heart-lung machine, temporarily takes over the cardiac pumping and pulmonary oxygenation activities. Considering recent progress in medical technology, less invasive alternatives such as transcatheter aortic valve implantation (TAVI) have become increasingly popular, particularly for individuals who are more vulnerable to open-heart surgery [27, 28].

Concerns regarding mortality and valve failure remain, especially in younger patients, due to potential device degeneration or an exaggerated inflammatory response, which can accelerate the calcification of valve leaflets. Nevertheless, studies have shown that TAVI is equivalent to SAVR in patients with intermediate surgical risk, providing a less invasive alternative while maintaining similar outcomes in this patient population. [29, 30]. Importantly, there are no significant differences in clinical outcomes and post-intervention hemodynamic between patients with severe aortic stenosis and a small aortic annulus who undergo TAVI compared to those who receive SAVR. Evidence of this equivalency has been established after a median follow-up period of two years, suggesting that both treatments provide similar outcomes in treating this specific group of patients [31]. A 10-year follow-up period in the NOTION trial, which compared TAVI to SAVR, revealed no significant changes in clinical outcomes between the two groups [32]. Undoubtedly, although both SAVR and TAVI are important in the management of aortic valve disease, the progressing capabilities of TAVI justify a more thorough investigation.

2.4 Transcatheter aortic valve implantation

TAVI is a minimally invasive procedure that has revolutionized the management of aortic valve disease, especially in high-risk and inoperable patients. During TAVI, a bioprosthetic valve is crimped and delivered via a catheter, typically inserted through the femoral artery, and deployed within the damaged aortic valve without the need for open-heart surgery. The native calcified leaflets are not excised but rather pushed aside by the expanding prosthesis, which anchors itself in the aortic annulus. Intricate structural and hemodynamic factors are involved in the interaction between the transcatheter aortic valve (TAV) and the native

anatomy. Figure 2.4 shows the different main transcatheter valves available in commerce. Some transcatheter heart valves (THVs), e.g., Edwards Sapien family, are balloon-expandable with chromium-cobalt (Co-Cr) stent, while others, e.g., Medtronic's CoreValve, are self-expandable owing to their shape-memory nitinol (Ni-Ti) stents.

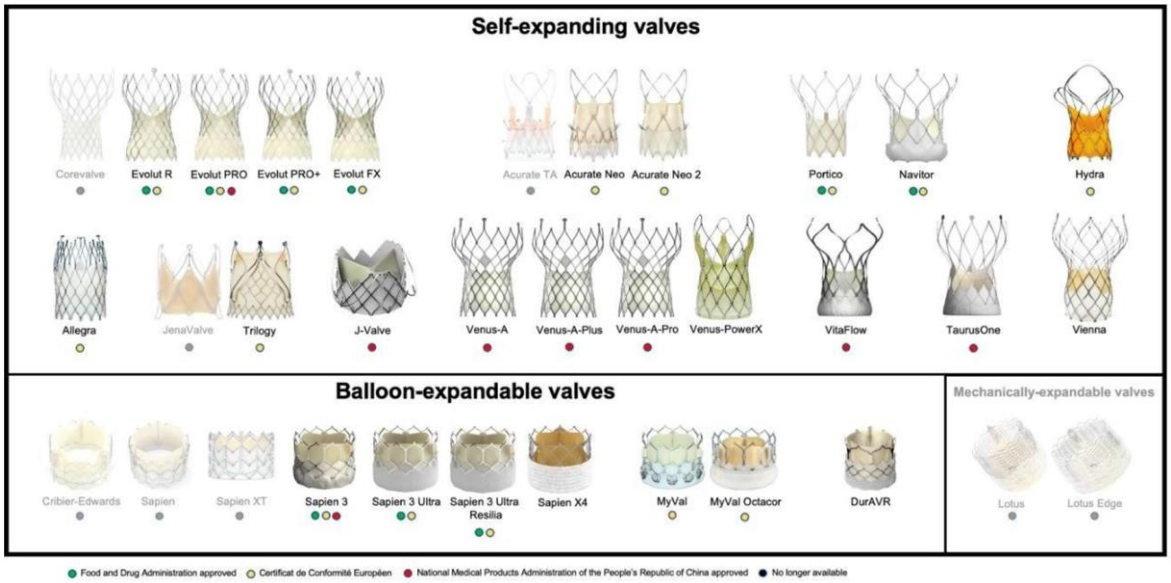

Figure 2.4. Commercially available transcatheter heart valves. With permission from Vinayak et al. (2024).

Both types of valves have demonstrated efficacy, though their selection depends on patient-specific anatomical and clinical factors. Unlike surgical valves, which are sewn into place, TAVs rely on radial force to remain positioned, and their design must account for both the physiological flow of blood and the mechanical stresses imposed by the calcified native valve. Self-expanding valves provide a larger orifice area and lower gradients. Their gradual deployment and supra-annular design allow for enhanced blood flow but are associated with a higher likelihood of pacemaker implantation due to increased pressure on the conduction system. On the other hand, balloon-expandable valves allow for more precise positioning and deployment, allowing a faster procedure. However, these valves tend to have a smaller effective orifice area, which can result in higher residual gradients [34].

Although TAVI was initially approved for high-risk patients with severe aortic stenosis, over the past decade, advancements in valve technology and procedural safety have significantly expanded its use to broader patient groups, including intermediate and low-risk populations and bicuspid patients [35]. In addition to its use in treating native aortic stenosis, TAVs have also been employed in Valve-in-Valve (ViV) procedures, which involve the replacement of a failing bioprosthetic or previously implanted transcatheter valve.

Though the TAVI procedure has been a real game changer in heart surgery, it is not devoid of complications, which are presently challenging to anticipate before the procedure. While TAVI has shown encouraging short- and mid-term results, there are still outstanding questions regarding the long-term durability of THVs. The ongoing expansion of TAVI into younger and lower-risk groups necessitates a growing emphasis on the durability of the devices. Current long-term data is still limited, as TAVI technology has been around for a shorter time compared to surgical valve replacements. Studies such as the PARTNER and Evolut low-risk trials are ongoing to provide more insight into the long-term performance of TAVI valves, with five- and ten-year data awaited to confirm their durability [36].

Early-generation TAVI devices were associated with a significant risk of paravalvular leakage (PVL), a condition characterized by the leakage of blood around the periphery of the implanted valve. Typically, it is due to the incomplete sealing of the valve prosthesis, under-sizing of the transcatheter valve, or poor positioning during deployment. Research has shown that advanced valve models, such as the Edwards Sapien 3 and Medtronic Evolut PRO, incorporate skirts or sealing cuffs that aim to minimize PVL, but these modifications do not entirely eliminate the risk [37].

Another notable complication is the development of conduction disturbances, as atrioventricular block or left bundle branch block, which may necessitate permanent pacemaker implantation (PPI). This risk is primarily related to the close anatomical proximity between the aortic annulus and the cardiac conduction system. The mechanical compression of the conduction pathways during valve deployment, particularly with self-expandable valves like the CoreValve, contributes to this issue [38].

Some THVs can occasionally cause the obstruction in the coronary arteries, particularly if the prosthesis or calcified native leaflets interfere with the coronary ostia. Thrombosis is also a major concern following TAVI, particularly due to the altered hemodynamic conditions and potential for stagnation or abnormal flow patterns around the prosthesis. Thrombus formation may impair leaflet mobility and increase the risk of embolic events.

Understanding the correlation between these complications and their underlying mechanical and hemodynamical causes is crucial for improving TAVI outcomes. Factors as the calcification profile of the native valve, the geometric and mechanical characteristics of the aortic root, unphysiological flow, turbulence and blood coagulability all contribute to the onset of complications. Conditions such as hypertension, coronary artery disease, and heart failure can further complicate the procedure [38].

To address these challenges, in-silico patient-specific models have emerged as a valuable research tool for improving pre-procedural planning and valve design. These models enable virtual simulations of valve deployment tailored to the patient's unique anatomy, allowing for predictions of valve performance and the likelihood of complications. Additionally, they provide insights into the blood flow dynamics around TAVs, which is essential for reducing complications like thrombosis and haemolysis. There is a growing focus on optimizing valve design to ensure more physiological flow patterns and to minimize the risk of blood cell damage, ultimately enhancing the safety and longevity of TAVI devices.

Chapter 3

State of the art

The investigation of heart valve biomechanics and hemodynamic has significantly evolved thanks to the advancements in both computational (in-silico) and experimental (in-vitro) methodologies. These methodologies provide an exhaustive examination of cardiac valve functionality in both healthy and pathological states, yielding critical insights that can enhance the design and execution of valve replacement therapies. This chapter provides an in-depth review of the current state-of-the-art in TAVI modeling. Results of this research have been published in [39, 40].

3.1 Computational approaches

In-silico modeling has emerged as an essential instrument to comprehend heart valve disorders and advance prosthetic device designs. The use of computational tools as finite element analysis (FEA), computational fluid dynamics (CFD) and fluid-structure interaction (FSI) analysis for TAVI assessment is gaining prominence and is crucial for enhancing clinical results of the treatment. The virtual deployment of the bioprosthesis in patient-specific models may offer a realistic assessment of postprocedural structural and hemodynamic function, hence potentially improving pre-TAVI planning.

3.1.1 TAVI FEA models

The patient-specific TAVI simulation workflow comprises the anatomical segmentation of the anatomies of interest. i.e., the aortic root and calcified valve leaflets, succeeded by the modeling of the biomechanical tissue response (e.g., material parameters), boundary conditions (e.g., constraints from the sub-valvular structure and contact between the device stent frame and aortic wall), loading conditions (e.g., the degree of balloon expansion), and analysis settings (e.g., the physics governing the deployment of the transcatheter heart valve). Crimping is executed by progressively diminishing the THV stent diameter, while expansion is performed in accordance with valve technology, involving either the inflation of a balloon positioned coaxially with the device or the incremental withdrawal of the sleeve catheter to facilitate the placement of the self-expandable THV. Upon achieving the solution, the actual configuration of the implanted bioprosthesis and the intramural stress applied to the aorta wall can be quantitatively visualized, providing important insights for preoperative planning.

The ideal device selection relies on various patient characteristics, including annular diameter and shape, degree and distribution of calcification, left ventricular outflow tract configuration, height of the coronary ostium relative to the valve annulus, and aortic angle [41, 42]. The dimensions of the device significantly influence the radial forces applied to the aortic wall. Insufficient radial forces may result in PVL and/or stent migration [43], whereas excessive radial expansion might cause cardiac conduction problems or aortic rupture [44]. THVs were precisely modelled in numerous studies mimicking the TAVI procedure utilizing the self-expandable CoreValve [45-49] and the balloon-expandable Sapien 3 [49-52].

Computational modeling was employed to enhance the characteristics of nitinol utilized in self-expanding devices [53, 54]. Material descriptors were derived from the fitting of the stress-strain response obtained from experimental radial force testing. Challenges remain in simulating the full crimping of the prosthesis to clinical catheter sizes due to mesh deformation issues, which are often bypassed by stopping the simulation before reaching the actual catheter diameter. Furthermore, many studies did not incorporate the modeling of valve leaflets and sealing skirts. Bailey et al. [55] have unequivocally shown that the bioprosthesis valve leaflets must be incorporated into the simulation, as the tissue experiences significant stress and deformation that could jeopardize the device's durability. Pasta and collaborators [56] identified disparities in the performance of the Sapien 3 compared to the Evolut Pro THV devices, whereas Nappi et al. [57] disclosed variances between the CoreValve and Sapien 3 THVs.

3.1.2 CFD TAVI models

The left heart CFD has played a pivotal role in evaluating the hemodynamic following TAVI. A multitude of investigations have employed CFD analysis [48, 56, 58-62]. This technique utilizes the deformed configuration resulting from the structural simulation of TAVI to perform flow analysis through either steady [46, 53, 63, 64] or transient [47-49] analyses. The configuration of CFD-related TAVI modeling is simpler than that of FSI analysis; nonetheless, these simulations depend on rigid geometries, which may fail to adequately represent the intricacies of host-device interactions inside the fluid domain. It has been shown [65, 66] that the aortic wall of patients undergoing TAVI exhibits stiffness and may be characterized by a linear elastic material model (i.e., Young's modulus of 4.5 MPa and Poisson's ratio of 0.45) in contrast to the healthy hyperelastic aorta, therefore validating the presumption of stiff aorta and device components in CFD simulations of TAVI.

FSI overcomes the constraints of stiff components, facilitating interactions between geometry and the fluid domain to yield more accurate results. Both Lagrangian-Eulerian and

immersed boundary methods have been adopted. The Lagrangian-Eulerian method [48, 50, 67, 68] necessitates distinct meshes for the fluid and solid subdomains, posing challenges for simulating the TAVI operation, where valve leaflets exhibit transient contact. The immersed boundary formulation incorporates the solid subdomain entirely into the fluid subdomain, yielding a more appropriate model for significant structural deformations and transient interactions between structures [69].

Another FSI methodology is smoothed particle hydrodynamics (SPH), which employs a meshless technique to simulate the fluid domain [51, 56, 59, 61, 70]. Unlike conventional methods, SPH utilizes a point cloud to depict geometry, assigning material properties to each point [71]. Although numerous efforts have been made to apply the meshless SPH method for simulating cardiovascular issues, limited research has concentrated on the aortic valve [56, 60-62]. Recently, Laha and colleagues [72] simulated valve dynamics within a patient-specific anatomy using SPH, proposing an innovative framework to estimate wall shear stress and other significant hemodynamic parameters.

The proficiency of SPH modeling, in contrast to the FSI technique, lies in the use of the general contact algorithm to account for the interaction between the fluid and the structural domain.

3.2 Challenging TAVI scenarios

3.2.1 Life-threatening complications

Following the advent of percutaneous treatments, PVL has been regarded as the "Achilles heel" of TAVI according to multiple reports [73-75]. It induces regurgitation during diastole due to the interstice between the deployed valve and the annulus. Gaps experience significant pressure gradients, possibly leading to platelet activation and thrombus formation and/or the dispersion of emboli in the bloodstream, hence elevating the risk of stroke. PVL can be anticipated through the evaluation of (i) inadequate prosthesis apposition to the native annulus, (ii) insufficient expansion, and (iii) improper device location [76]. These risk factors could be partially expected by means of pre-TAVI CT. Most simulations focus on evaluating PVL from structural and fluid-dynamic viewpoints. The standard computational approach initially replicates the TAVI method, followed by the execution of CFD or FSI to quantify PVL [46-52, 59, 63, 66, 77]. Among these, Mao et al. [47] observed a strong correlation between predicted and echocardiographic measurements of PVL while modeling the CoreValve in patient-specific models. Basri et al. [50] employed a FSI simulation method to investigate the correlations between regurgitation and the extent of leaflet calcification, specifically concerning geometric orifice area openings in relation to hemodynamic flow

within a patient-specific aortic model. The simulations indicated that the minimal percentage of geometric orifice area opening correlated with the greatest probability of PVL. Prisco et al. [78] demonstrated that mathematical modeling utilizing CFD can forecast the position and precisely quantify the PVL. The data indicated that the prevalence of leakage diminishes as the volume of the area occupied by PVL increases, illustrating that the native aortic valve has a role in mitigating regurgitation and preventing PVL.

Coronary obstruction is an uncommon yet lethal consequence with TAVI [79]. Wald et al. [68] conducted a hemodynamic assessment of TAVI cases, examining the association among orifice area, systolic blood velocity, vortex location, pressure drop, and coronary flow by simplified 2D numerical simulations. They successfully predicted the risk of coronary obstruction in comparison to clinical measures. Heitkemper and colleagues [79] colleagues have established the fractional obstruction index of coronary obstruction to enhance risk prediction in patients receiving TAVI.

A significant high-risk consequence of TAVI is also conduction anomalies, including atrioventricular block. These anomalies may arise from either acute or persistent contact injury to the atrioventricular conduction tissue [80]. CFD simulations offer insights into modified flow patterns that may lead to conduction anomalies, facilitating the prediction and management of these issues. Hamdan et al. [81] recently examined the idea that the length of the membranous septum, as assessed by CT, is a significant pre-procedural anatomical predictor of conduction problems associated with TAVI. McGee et al. [82] proposed a link between the numerically projected implantation depth of the Lotus device and the emergence of conduction disruptions. They found that the wall stress increased near the bundle of His as a function of the implantation depth and conductance interference. Rocatello and collaborators [83] proposed that the likelihood of conduction problems is associated with the contact pressure applied by the THV stent frame on the aortic wall.

3.2.2 Emerging and specialized applications

Despite the exclusion of patients with bicuspid aortic valve (BAV) from all clinical studies, the clinical viability of TAVI in this intricate patient demographic has been established [84, 85]. Patient-specific simulations are essential for assessing the interplay between the oval bicuspid annulus and device performance. Pasta et al. [51, 59] employed FEA to assess the deformed configuration and contact pressure of the Sapien 3 in relation to the stenotic bicuspid valve. They also implemented the SPH methodology for the assessment of PVL. The model accurately predicted the elliptical configuration of the implanted THV as confirmed by post-TAVI CT imaging. Comparable investigations simulated the use of THV

devices in patients with bicuspid aortic valve anatomy to evaluate the risk of PVL associated with the CoreValve device [45, 46, 63] further confirming the potential TAVI feasibility in this patient population.

The valve-in-valve (ViV) procedure entails the implantation of a THV within the pre-existing biological valve. Scuoppo and collaborators [60] conducted a computational analysis to assess the risk of device obstruction on the resultant coronary flow following TAVI-in-TAVI for various deployment options. The findings indicated that a substantial implantation depth and an undersized second transcatheter device could markedly diminish coronary flow up to 20% of the anticipated level prior to TAVI.

3.3 VVUQ standard

Despite the success of various computational studies in tackling significant obstacles in modeling TAVI, the literature is lacking in patient-specific models that adhere to a stringent methodology to validate their predictive accuracy [86]. Computational simulations necessarily involve risks, and when a computational model aims to inform clinical or regulatory decisions, it is essential that the model is sufficiently credible to support its predictive capabilities.

For in-silico models to be reliable, they must adhere to a structured process as outlined by the ASME V&V 40 standard [87], a risk-based framework delineating credibility standards for computational models to ensure both accuracy and relevance to real-world clinical situations. Regulatory agencies are presently evaluating data from modeling and simulations to expedite the market entry of biomedical devices and to decrease the associated costs of device design and animal testing. Consequently, due to the absence of established modeling techniques, there is an increasing interest in quantifying these models and evaluating their reliability [86].

ASME has released the V&V 40-2018 technical standard titled “Assessing Credibility of Computational Modeling through Verification and Validation: Application to Medical Devices,” which delineates the model credibility evaluation process and specifies the minimum qualifications required by regulatory agencies. Verification, validation, and uncertainty quantification (VVUQ) can be used to establish trust in the predictive capability of a computational model. Verification activities allow to confirm that a computational model aligns with the mathematical description, while validation is conducted to evaluate whether the model accurately reflects the real-world system for a certain application. Uncertainty quantification is finally employed to assess the influence of modifications in

numerical and physical parameters on the simulation results [88, 89]. Overall, the ASME V&V 40-2018 standard presents a risk-based methodology for determining the credibility criteria of computational modeling tailored to a specific context of use, delineating the precise role and objective of the computer model in addressing a particular inquiry. The overarching V&V process, schematized in Figure 3.1, starts with the definition of the 'Question of Interest' (QoI), followed by defining the 'Context of Use' (CoU) and associated model risk assessment. Risk analysis evaluates the interplay between model influence and decision consequences, with the model's role in clinical decisions being commensurate with the gravity of negative outcomes. The established model risk level guides the establishment of the rigor of output comparison. Simulation and experimental results are then used to evaluate the credibility of the in-silico model with respect to the specific COU.

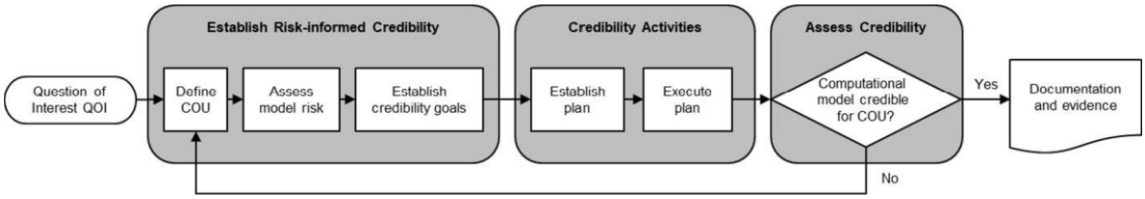

Figure 3.1. V&V workflow. Reprinted from ASME V&V 40-2018, by permission of The American Society of Mechanical Engineers. All rights reserved.

Limited research has conducted VVUQ on cardiovascular issues. Luraghi and collaborators [90] conducted verification analysis to simulate an idealized tri-leaflet heart valve model, examining the effects of element type, formulation, and damping factor. Similarly, Tango et al. [91] corroborated a fluid-structure interaction model of the aortic valve and root by juxtaposing the projected velocity field with that obtained from an in-vitro flow analysis. Recently, Bosi et al. [52] validated a computational model of TAVI utilizing both Sapien XT and CoreValve devices by comparing it with post-procedural clinical fluoroscopy and echocardiography images. They observed a strong correlation between the predicted and image-derived device sizes.

The advancement of CFD/FSI models for TAVI necessitates the validation of these models against experimental data, which is essential for maximizing their influence on therapeutic interventions. In this context, various in-vitro methodologies for arterial flow measurements, such as particle image velocimetry (PIV), have been recognized as effective instruments for validating fluid dynamic models [92]. A further problem is the VVUQ analysis for patient-specific geometries, which is presently a focus of rigorous regulatory science research associated with the advancement of digital twins.

3.4 Conclusions

In-silico methodologies can offer a robust and reliable approach to investigating the biomechanics and fluid dynamics of heart valves, particularly in the context of TAVI. Computational modeling techniques such as FEA, CFD, and FSI provide valuable insights into the mechanical performance and hemodynamic outcomes of THVs devices. These methods enable realistic simulations of patient-specific anatomies, allowing for better pre-procedural planning, optimization of device selection, and prediction of potential complications such as PVL, coronary obstruction, and conduction abnormalities.

Future research must focus on refining the accuracy of these simulations by addressing limitations such as the crimping process, the behavior of valve leaflets, and the effect of sealing skirts. Additionally, implementation of VVUQ processes is essential to enhance model's credibility and ensure their reliability for clinical and regulatory use.

Chapter 4

Patient-specific benchmark TAVI model

This chapter introduces the development of the patient-specific benchmark TAVI model, which will become the basis for material calibration and verification & validation (V&V) activities. By providing a detailed description of the components involved and the techniques adopted, it lays the groundwork for the subsequent activities presented in Chapters 5 and 6.

4.1 Study population

Twenty patients, aged between 75 and 91 years, who underwent TAVI at IRCCS ISMETT hospital, were enrolled in this study following the acquisition of ethical approval and informed consent. Upon hospital admission, demographic data, brachial cuff pressure measurements, and Doppler echocardiography data were collected to assess the severity of AS (Table I). ECG-gated CT imaging with contrast agent was performed for each patient, resulting in two distinct sets of CT images representing the systole and diastole phases before TAVI procedure. The TAVI procedure was performed via transfemoral access under general anesthesia, with the implantation of the 23-mm Sapien 3 Ultra (S3) device (Edwards Lifesciences, Irvine, USA) positioned toward the left ventricle for one-third of its length. No pre-dilation or overexpansion of the device was conducted. Follow-up angio-CT scans were obtained one-month post-procedure.

Table I. Clinical demographic, CT-related measurement and Jaccard index and Young's modulus after optimization.

	Age (yrs)	**Sex**	**P_{sys} (mmHg)**	**P_{dias} (mmHg)**	**HR (bpm)**	**CO (ml/min)**	**$Strain_{Ann}$ (%)**	**$Strain_{Sinus}$ (%)**	**$Strain_{STJ}$ (%)**	**Orifice Area (mm2)**	**JI (%)**	**E (MPa)**
#1	79	M	162.0	48.0	92.0	5336.0	3.4	1.4	4.8	140.2	91.5	6.1
#2	90	F	140.0	75.0	87.0	4611.0	3.6	0.7	5.3	86.5	86.9	6.2
#3	85	F	160.0	90.0	65.0	3174.0	1.8	3.1	0.3	119.0	90.1	6.2
#4	83	F	143.0	60.0	67.0	4690.0	5.8	5.2	1.9	87.8	83.7	6.3
#5	86	F	107.0	59.0	91.0	5005.0	7.4	8.6	3.7	105.4	85.2	5.2
#6	85	F	150.0	52.0	61.0	3416.0	8.0	3.6	6.8	70.8	86.9	3.8
#7	85	F	138.0	78.0	74.0	2442.0	2.0	1.8	1.8	119.8	88.6	6.2
#8	89	M	120.0	58.0	63.0	3591.0	1.7	1.8	4.3	112.8	86.7	6.2
#9	91	F	138.0	55.0	69.0	2415.0	4.6	8.5	6.1	108.4	84.2	7.7
#10	83	F	110.0	52.0	65.0	4485.0	1.9	0.4	1.8	102.2	85.3	7.4
#11	75	M	100.0	55.0	64.0	4575.0	4.3	1.6	7.2	104.3	86.7	6.2
#12	85	F	151.0	54.0	67.0	2881.0	9.1	3.6	4.0	97.8	85.9	3.4
#13	86	F	119.0	58.0	62.0	3162.0	3.5	3.7	4.2	109.4	86.5	5.9
#14	84	M	123.0	78.0	68.0	3808.0	3.2	4.1	4.4	125.7	90.3	5.0
#15	79	M	126.0	60.0	61.0	3104.0	8.2	8.5	7.9	165.2	84.9	3.9
#16	75	M	128.0	47.0	62.0	3968.0	1.8	2.1	1.8	140.8	85.7	7.5
#17	82	M	113.0	64.0	81.0	6399.0	7.4	7.7	8.2	100.8	86.9	4.9
#18	78	M	136.0	67.0	60.0	5100.0	3.5	2.8	3.1	138.6	89.9	5.9
#19	82	M	105.0	55.0	65.0	3185.0	6.2	6.1	6.4	145.2	88.5	4.9
#20	85	F	118.0	58.0	88.0	4210.0	4.8	5.1	5.2	98.5	85.1	3.6
Mean	83		129.4	61.2	70.6	3977.9	4.6	4.0	4.5	114.0	87.0	5.6
SD	4		18.3	11.2	10.9	1046.3	2.4	2.7	2.2	23.1	2.2	1.3

Note: M/F=male/female; Psys= systolic pressure; Pdias= diastolic pressure; HR= heart rate; CO=cardiac output; JI=Jaccard Index.

4.2 Patient-specific model platform development

The patient-specific model, shown in Figure 4.1, accounted for the aortic root and its calcified valve. Specifically, the anatomical regions of interest included: i) the left ventricular outflow tract (LVOT), ii) the sinus of Valsalva, iii) the ascending aorta from the STJ junction to the distal aorta, iv) native aortic valve leaflets, and v) calcific plaques.

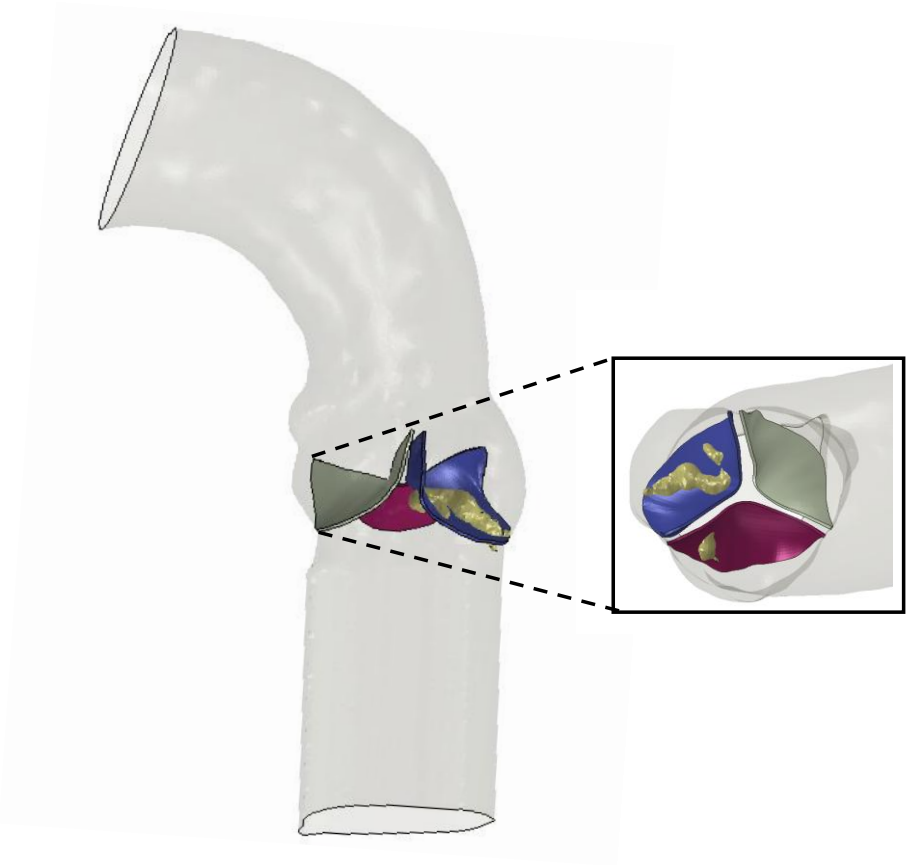

Figure 4.1 Patient-specific platform for TAVI integration.

The pre-TAVI CT scans at diastole were employed to reconstruct the anatomies using the Mimics medical imaging software (v21, Materialise, Belgium), as done in previous studies [93, 94]. Semi-automatic thresholding, followed by manual refinement and smoothing were adopted while preserving boundaries of interest. In all cases, 10 cycles of smoothing iterations with smooth factor of 0.4 were performed. The resulting part was then exported as STereo Lithography interface format (STL) file and edited in the Computer-Aided Design (CAD) software Rhinoceros (v.7.0, McNeel & associates). The distal and proximal ends of the aorta were cut with a plane normal to the aortic centerline and extended to reduce the effect of transient flow in flow simulations.

Since the reconstruction represented the diastolic phase, the stress-free configuration needed to be derived. This was accomplished in Abaqus/Explicit software using a method developed by Krishnan and collaborators [95]. Initially, the aortic root was assumed to have a supra-

physiological stiffness (i.e., Young's modulus, E=1000 MPa; Poisson's ratio, v=0.45), so that the application of systolic pressure would not deform the geometry. The aortic root wall was then subjected to systolic pressure, and the stress distribution for the individual elements of the aortic wall was determined and used as input for the second step. In the second step, the stress distribution results from the first step were specified as the initial wall stress. The supra-physiological material properties were then replaced by physiological properties (i.e., neo-Hookean model). The zero-pressure geometry was finally calculated by gradually reducing the inner surface pressure load to 0 mmHg. The resulting stress distribution at the end of the unloading step (i.e., at 0 mmHg) was very low, representing the residual stress distribution of the aortic vessel (Figure 4.2). For boundary conditions, the proximal and distal ends of the aortic wall were fixed in all directions with respect to the general reference system.

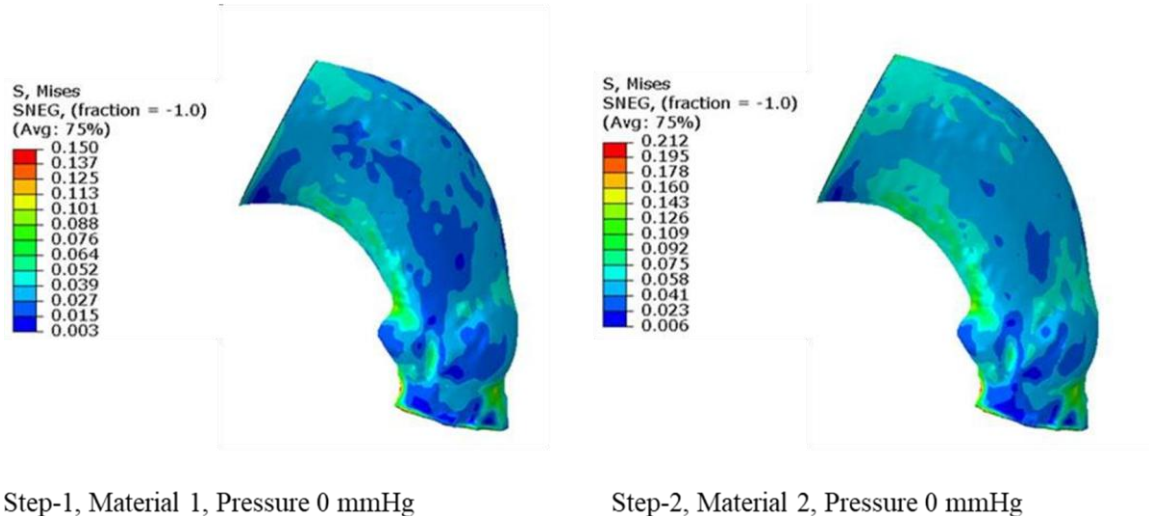

Figure 4.2. Residual stress distribution of the aortic wall with supraphysiological (left) and physiological (right) material properties.

Due to the thin structure of the aortic valve leaflets, segmentation from the CT scans was not feasible. Therefore, a parametric model based on anatomical landmarks was developed to derive the native valve, as done in prior studies [96]. The leaflets were designed using anatomical measurements and third-order NURBS curves in Rhinoceros CAD software (Rhinoceros v.7, McNeel & Associates, USA). The free margins of the leaflets were manually delineated using spline curves in the axial plane of the diastolic images. The leaflet-to-sinus connections were delineated with spline curves created on the aortic root surface. Each leaflet's belly was modeled using a curve limited by both the leaflet-free edge and the leaflet-to-sinus curves. A control point at the mid-level was used to define the curvature of the native valve leaflets via a spline curve. The leaflet-to-sinus curves were

mapped onto the aortic root surface, and the final configuration of the native valve leaflets was constructed using a multi-patch surface network.

Calcific plaques segmentation was fully automated by thresholding with HU>800, with difference occurring from patient to patient. Once the mask was generated, the 3D part was calculated without any manual editing or smoothing.

To enhance the credibility of TAVI simulations, the patient-specific model was developed in compliance with ASME V&V40 criteria. A distinct study, described in the following chapters, focuses on material calibration and the V&V of the proposed computational framework. The aorta wall was discretized with triangular shell elements (S3R) of 0.8 mm size, whilst the calcification was discretized with tetrahedral solid elements (C3D4) of 0.5 mm size. An unstructured prismatic mesh (C3D6) was created for native valve leaflets by extruding triangular shell pieces (0.6 mm in size) in four layers through the thickness. The aorta wall was presumed to have a thickness of 2 mm, while the native valve leaflets exhibited a consistent thickness of 0.5 mm [66]. Mesh convergence analysis was conducted for four patients, establishing the minimal mesh refinement value for each anatomical component as the best configuration for the entire patient cohort.

The biomechanical response of the aortic root and leaflets was represented by a neo-Hookean model with a Poisson's ratio of ν=0.475 and material parameters moduli determined through inverse analysis. A neo-Hookean material model was also employed for the calcific plaques with C1=67.7 MPa and n=D1=7.5E-3 MPa [66].

4.3 S3 device and delivery models

The Sapien 3 Ultra (S3) by Edwards Lifesciences is a balloon-expandable stent frame made of cobalt-chromium (Co-Cr) with a trileaflet bovine pericardial tissue valve and a sealing skirt made of polyethylene terephthalate (PET). With its high radial stiffness, the S3 maintains a constant opening in the aorta, preventing significant deformation even within complex biomechanical environments, such as calcified leaflets, the aortic root, and during transient pressure changes. The sealing skirt helps reduce paravalvular leaks, ensuring improved procedural outcomes and durability.

Similarly to the patient-specific model, the S3 device model was validated in accordance with ASME V&V40 criteria. Various modeling methodologies and element mesh types were deeply investigated to enhance computational efficiency while maintaining structural performance. Figure 4.3 shows the S3 Ultra model alongside the real device. The stent framework was simulated using surface components to depict the external device covering

and beam elements to illustrate the internal structure. Following discretization analysis, the S3 geometry was meshed using 22,974 surface elements (SFM3D4R) connected to 5,718 beam elements (B31). The stent frame's cobalt-chromium material was modeled utilizing a combination of isotropic elasticity and Johnson-Cook plasticity to address hardening and rate-dependent material characteristics. The elastic model exhibited a Young's modulus of

238.54 GPa and a Poisson's ratio of 0.29. The plasticity model was characterized by a yield stress of A=465.0 MPa, a hardening parameter of B=2.140, a coefficient of n=0.73, and a density of 7,650 kg/m³. The valve leaflets for the S3 model were acquired via a forming simulation procedure. This entailed fabricating the leaflets in a flat orientation and subsequently transforming them into their definitive functional configuration through a series of geometric procedures, as delineated by Bailey et al. [55]. The device valve leaflets were modeled using 1,457 structured elements (C3D8R) and a single solid-element layer throughout the thickness. The Ogden constitutive law, represented by a second-order polynomial, was utilized to characterize the biomechanical behavior of pericardial tissue, employing parameters m1=0.96 MPa, a1=-56.5, m2=3.57 MPa, a2=1.87, and D=0.027 MPa. The device skirt was designed using a neo-Hookean material model (C1=1.7 MPa and D=0.65 MPa) and was affixed to the stent frame to simulate the device suture. To avoid high-frequency oscillations, a Rayleigh damping coefficient of 250 was implemented on the device skirt, and a viscous pressure of 6.55E-06 MPa was supplied to the inner surface of the valve leaflet. The balloon was modeled using 82,322 unstructured shell components (S3), with shape derived from Bailey et al. [55] and neo-Hookean material properties (C1=36.5 MPa and D=1.36E-3 MPa).

Figure 4.3 A) Real S3 Ultra device (left) and S3 Ultra numerical model (right).

4.4 TAVI Integration

Prior to implantation, the device is placed on the folded balloon catheter and crimped to a specified diameter so that it can fit inside the sheath. Device positioning is then accomplished using radiopaque valve-related alignment markers on the balloon catheter, which define the working length. A 3-mm center marker, located at the midpoint of the balloon catheter, is used for deployment (i.e., the Commander delivery system). The distal end of the balloon marker is aligned with the base of the aortic valve cusps, representing the aortic annulus circumference by the three hinge points on the aortic annulus (Figure 4.4).

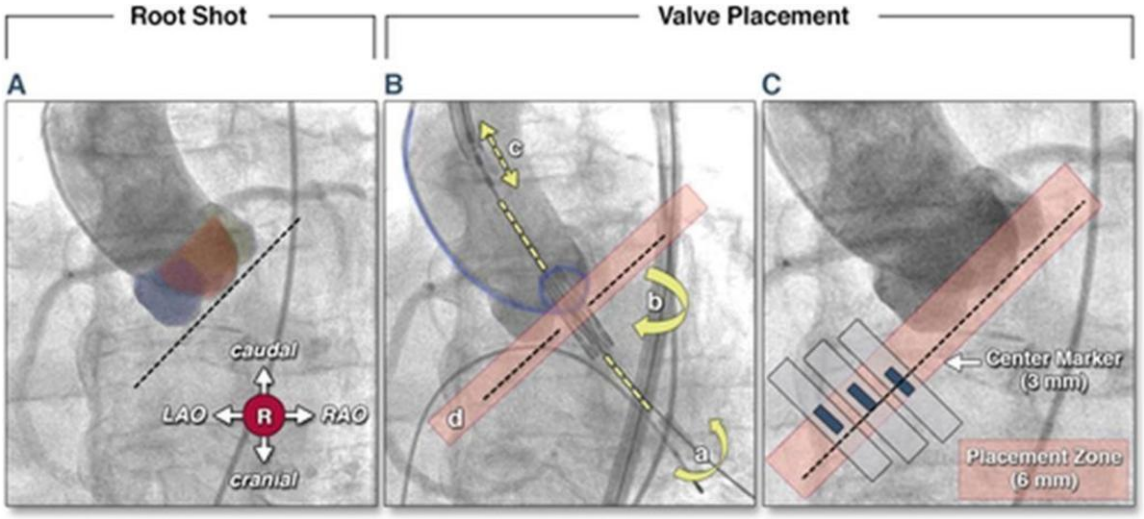

Figure 4.4. Implantation view and device positioning with the centre marker. With permission from Kronzon et al. *(2015).*

According to manufacturer's guidelines, the S3 device is placed with 80-90% in the aorta while the remaining 10-20% faces the LVOT. The balloon axis is aligned perpendicular to the aortic valve plane. Balloon inflation, controlled by a specified fluid volume, is used to deploy the device in the human host. The fluid volume required for balloon inflation varies based on the size of the device, as outlined in Table II.

Table II. Inflation parameters for the S3 device with different diameters.

Nominal Balloon Diameter	Nominal Inflation Volume	Rated Burst Pressure (RBP)
20 mm	11 mL	7 atm
23 mm	17 mL	7 atm
26 mm	23 mL	7 atm
29 mm	33 mL	7 atm

To replicate this clinical procedure, an automatic framework based on Python was developed by our partner 4Realsim to align the device in the patient-specific model. The patient-specific model served as input for the Python script. To enable the automated integration of the patient-specific platform with the S3 TAVI system, the three hinge points were identified for each patient by detecting their coordinates from the CT scans. The balloon axis was computed as the axis of the circle defined by these three hinge points, intersecting the annulus at its centre. A cylindrical reference system was then created, with the center of the aortic annulus as the origin and the -z axis aligned along the balloon axis. Figure 4.5 illustrates the orientation of the balloon axis relative to the stenotic valve leaflets.

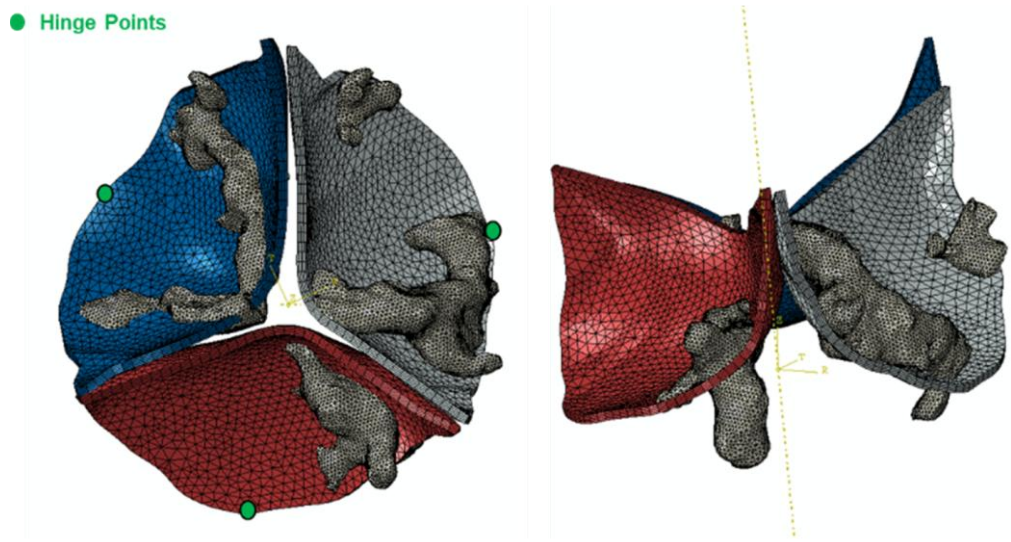

Figure 4.5. Representation of the balloon axis and coordinate system orientation with respect to stenotic valve leaflets.

The script then automatically positioned the device system at the level of the balloon radiomarker (i.e., at the midpoint of the balloon) and aligned the delivery system with the aortic annulus. Two parameters, the balloon axial position shift and the radiomarker shift, were defined to control the relative position between the device and the patient model. The balloon axial position shift ensured the alignment of the balloon and catheter with the S3 device, while the radiomarker shift adjusted the entire S3 system along the balloon axis (-z direction) to ensure proper positioning on the aortic annulus. The final implantation depth, derived by post-TAVI CT scans, was used, ensuring optimal placement.

The integration process was standardized across all patient models and device sizes by using consistent terminology for each anatomical part, datum feature, and mesh. The device selection, size, implantation depth, and balloon inflation volume were all parameterized, allowing the script to adjust the model automatically based on user input. To model the

complex delivery of the S3 system into the aortic root, several contact conditions were defined. These included tangential behavior modelled with a penalty friction formulation and normal behavior with hard contact.

The TAVI simulation workflow follows three distinct simulations, which are schematized in Figure 4.6.

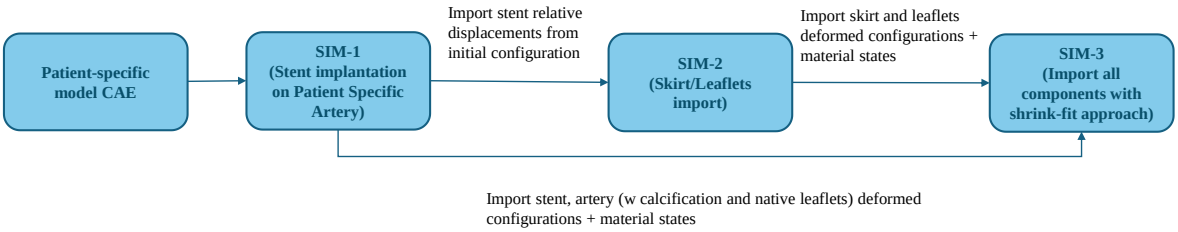

Fig. 4.6. Simulation workflow for the three-step TAVI simulation process.

In SIM-1, the metallic stent frame is crimped onto the folded balloon to achieve the nominal crimped diameter, followed by the stent's recoil. The final stage involves balloon inflation and deflation, deploying the device. This process is executed using a fluid cavity approach in combination with a VUAMP subroutine, which controls the stent expansion to its nominal diameter based on the inflation volume. Additionally, a cylindrical surface is employed to displace calcified plaques and native leaflets, preventing undesired penetration during the assembly of other device components. A 0-velocity boundary condition is applied to the stent to ensure stability. Figure 4.7 illustrates the key steps of the device deployment during SIM-1.

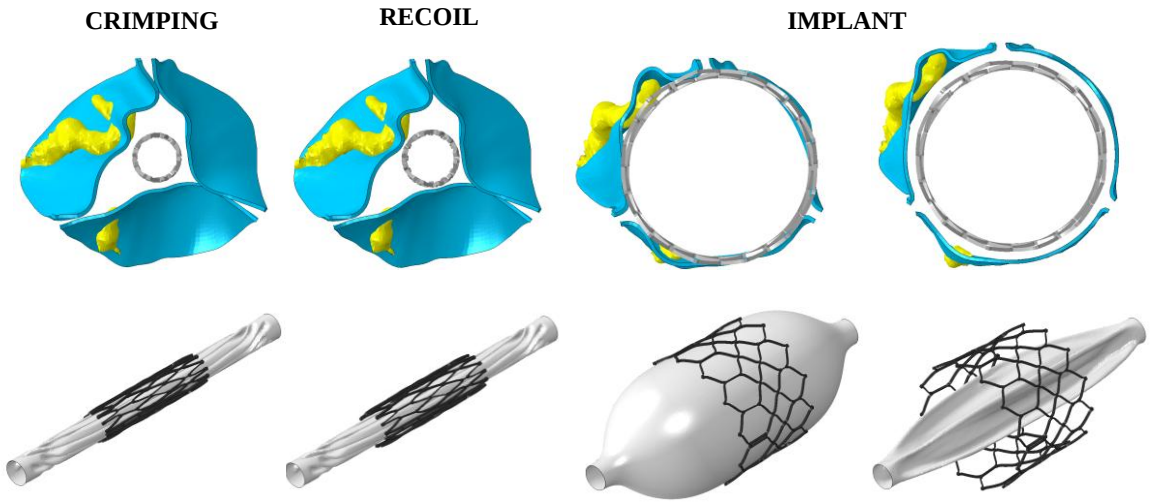

Figure 4.7. Deformed configuration of calcified valve, S3 frame, and balloon after crimping, recoil and implantation.

In SIM-2, the deformed configuration of the device, including the valve leaflets and skirt, is imported, as these components were not included in SIM-1. During this single-step

simulation, the S3-related leaflets and skirt are introduced, and constraints are established between the stent, leaflets, and skirt. The nodal displacements from SIM-1 are first applied to the stent in its undeformed state. As the simulation progresses, these displacements guide the stent to its final deformed configuration. Since the leaflets and skirt are constrained to the stent from the beginning, they deform accordingly throughout the process (Figure 4.8).

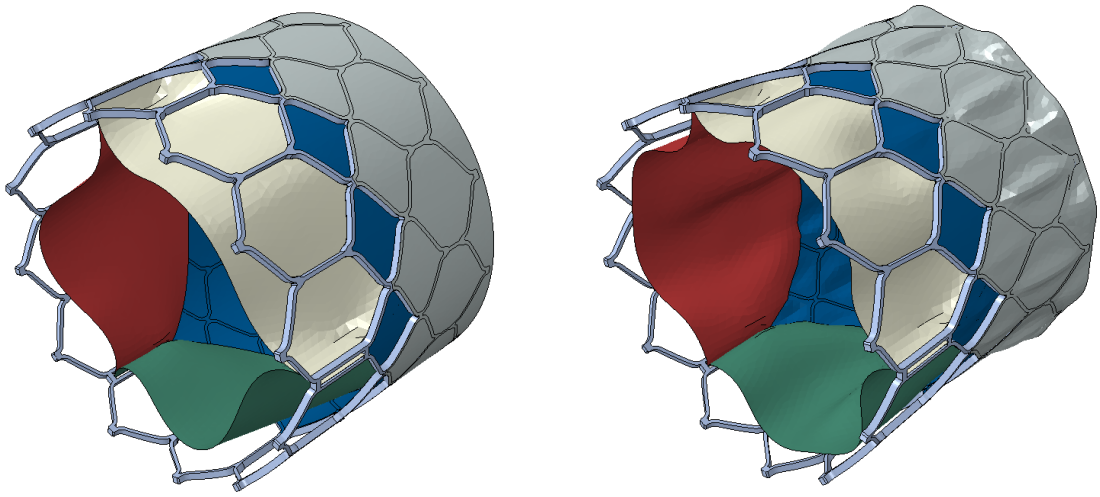

Figure 4.8. Simulation results from SIM-2 showing the undeformed (left) and deformed (right) S3 frame with skirt and valve leaflets.

In SIM-3, the entire device is fitted into the patient-specific platform, with all components imported in their deformed state from SIM-1 and SIM-2. The surface used in SIM-1 to displace calcifications and native leaflets is returned to its original dimension, allowing the anatomical parts to elastically recoil and make contact with the S3 skirt. High-friction contact is established between the skirt, stent, native leaflets, aorta, and calcifications to prevent slippage during flow analysis. The components are imported using a shrink-fit approach, resolving overclosure and enhancing friction between the device and the patient-specific anatomy (Figure 4.9).

Figure 4.9. Undeformed (left) and actual (right) configuration resulted from SIM-3.

4.5 Discussion

This chapter delineates the workflow employed for modeling patient-specific TAVI simulations. It outlines the reconstruction of individualized anatomical structures and the incorporation of the Sapien 3 Ultra device with its associated delivery system.

A novel parametric method was introduced to reconstruct the morphology of stenotic valve leaflets, which may be undetectable on CT scans. Following the development of the patient-specific platform, Python scripting facilitated the automatic integration of the TAVI system for each patient, thereby expediting the replication of the procedure the entire patient cohort. Additionally, this parametric approach facilitated the straightforward translation of the device along the patient's centerline, enabling corrections to the implantation depth based on clinical observations. These advancements may greatly accelerate the creation of patient-specific models for larger cohorts, enabling the simulation and validation of the proposed in-silico method.

Most relevant patient specific TAVI FEM models studies, such as the ones from Auricchio et al. [98], Bosi et al. [66], Bianchi and collaborators [49] did not include all TAVI components. Hence, the computational platform proposed in this study can be considered as beyond current state of the art. The creation of high-fidelity in-silico models encompassed multiple factors that affect the overall behaviour and efficacy of the TAVI procedure. Patient-specific material properties, boundary conditions, and loading scenarios were carefully incorporated to simulate realistic device-tissue interactions, ensuring that the model accurately reflected the mechanical response of the anatomy and device during deployment. The next step in refining this model has involved material calibration, which is crucial to ensure that the simulated material properties, i.e., those of the valve leaflets, stent frame, and surrounding tissues, accurately represent their behaviour under physiological conditions. The following chapter will focus on the material calibration processes applied to these components, which is essential for enhancing the predictive accuracy and clinical relevance of the in-silico TAVI model.

Chapter 5

Patient-specific material calibration

Despite the promising outcomes of current computational methods [49, 51, 99], the actual material properties of TAVI patients remain largely unknown and uncertain. This knowledge gap arises because tissue samples cannot be obtained for ex-vivo biomechanical evaluation, and the current material descriptors lack reliability, likely due to age-related changes in the vessel wall [100]. As a result, realistic material properties specific to TAVI patients are unavailable for use in numerical simulations. To develop a truly accurate and reliable computational model of TAVI, it is crucial to incorporate patient-specific material properties.

This chapter explores the techniques employed to non-invasively estimate patient-specific material properties of the aortic root and calcified valve leaflets. A regression analysis which reduces the discrepancy between predictions and CT-derived measurements of aortic wall strain and valve orifice area was established. The suggested material calibration strategy is validated at two stages. Prior to TAVI, the quantitative predictions of the vessel's systolic configuration and valve orifice area were juxtaposed with the actual angio-CT results. Following TAVI simulations, predicted device diameters were compared with post-procedural CT-derived values (see Chapter 6). The results of this study were published in [65, 101].

5.1 FEA of pre-TAVI scenario

The patient-specific model platform described in Chapter 4 was employed to set up a computational model of the cardiac beat before TAVI. The latter was used for the development of the inverse analysis aimed at estimating the patient-specific material properties using in-vivo imaging.

Patient-specific simulations of this pre-TAVI scenario were carried out in the Abaqus\Explicit solver (v.2021hf7, Dassault Systèmes, FR). Boundary conditions were estimated by scaling physiological pressure curves starting from the acquired patient clinical data. Specifically, the systolic and diastolic pressures were used to scale the maximum and minimum of the curve respectively, while the heart rate was involved in scaling its duration as shown in Figure 5.1.

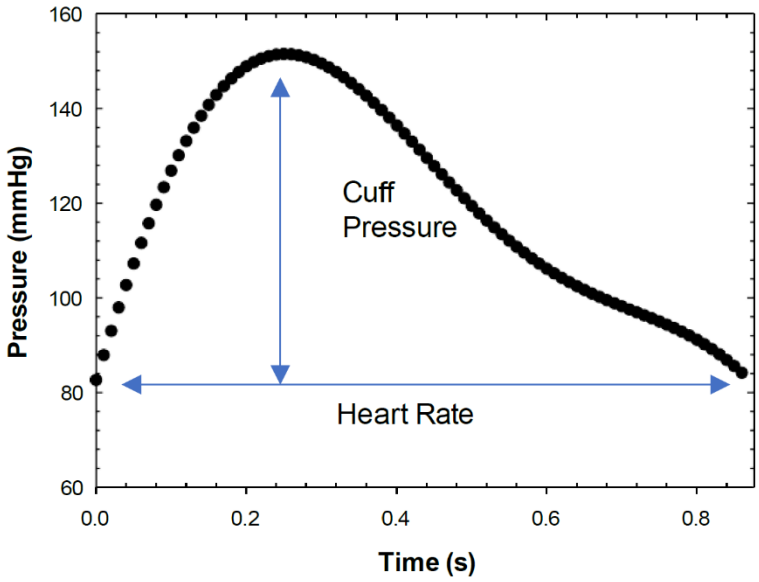

Figure 5.1 Pressure waveform employed for the development of patient-specific pressure boundary conditions.

A uniform pressure load was applied to the native leaflets ventricular side corresponding to the value of pressure gradient detected from the echocardiography. The distal and proximal ends of the aorta were constrained in longitudinal directions, while embedded contact conditions were used to constraint the calcification to native valve leaflets.

To implement the inverse analysis, the outputs of interest resulted from the pre-TAVI cardiac beat simulations were for the aorta, the maximum principal stress and the peak systole maximum principal strain at three analysed sections (i.e., STJ, Sinus, Annulus), while for the native valve leaflets were the geometric orifice area (GOA), the maximum principal stress, and the maximum principal strain. Element set at annulus, sinus and STJ levels of the aortic root were defined in order to export the corresponding nominal strains during peak systole. Given the adoption of linear elastic material for the aorta and native leaflets, an algorithm with the Grasshopper plugins of Rhinoceros (v.7.0, McNeel & associates) was developed to compute after the simulation the strain in circumferential direction for the aorta in order to compare it with the circumferential strain measured from the medical imaging analysis. By means of the aortic centerline, longitudinal and circumferential vessel direction were obtained for each element of the aortic mesh. The evaluation of the GOA encompassed the development of a Python script which automatically computes the area in Rhinoceros CAD software for each patient simulation. The script along with an algorithm written in Rhinoceros Grasshopper (Figure 5.2) allowed to automatically extrapolate the nodal coordinates of the valve leaflet free edges and then calculated the valve orifice area by spline interpolation of the extracted points.

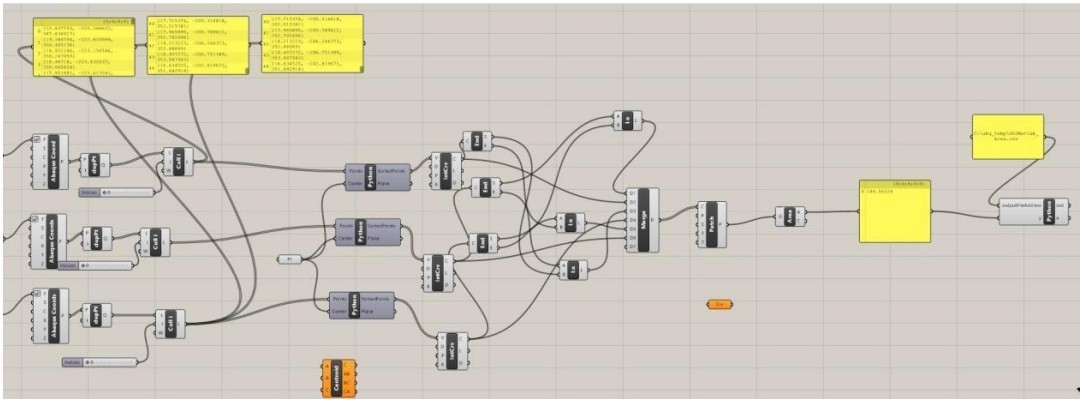

Figure 5.2. Grasshopper algorithm for orifice valve area estimation.

5.2 Inverse Analysis

The inverse analysis aims to derive the material parameters that minimize the discrepancy between the aortic wall strain and the aortic valve orifice area in the pre-TAVI FEA and the actual imaging measurements after simulating an entire cardiac beat.

A regression model was assumed to link the input variables (i.e., material properties) to the output variables (i.e., aortic wall strain or orifice area for the stenotic valve). From the CT scans, the peak systolic strain was calculated as:

$$Strain_{CT} = \frac{D_{sys} - D_{dias}}{D_{dias}} \qquad \text{Eq.1}$$

Where D_{sys} and D_{dias} represent the systolic and diastolic aortic diameters measured from the ECG-gated CT scans. The orifice area of the aortic valve was calculated during peak systole in the aortic valve plane.

Under the assumption of linear elastic material properties, the unknown material parameters were exclusively characterized by the elastic moduli of the aortic wall and native valve leaflets. The minimization was executed with a least-squares approach based on the subsequent quadratic regression model:

$$f(E) = \beta_1 E + \beta_2 E^2 + \beta_3 \qquad \text{Eq. 2}$$

Where E is the unknown constitutive parameter under study and β are the regression coefficients. For each patient, fifteen patient-specific FEAs were performed to simulate the cardiac cycle with the material properties randomly varied within the range of 0.8-15 MPa for each simulation. In this setting, an automated Matlab (v.2021a, MathWorks Inc) algorithm has been created to sequentially vary the value of the material parameters and then run the simulations. Following the FEAs, a matrix was assembled in Matlab software (v.2021a, MathWorks Inc) to correlate the input (i.e., material parameters for each random

value of Young's modulus) with the output (i.e., systolic strain/orifice area). Consequently, the cost function for both the aortic wall and calcific valve leaflets can be expressed as:

$F = f(E) - Strain_{STJ,\ Sinus,\ Annulus}$ Eq. 3

$F = f(E) - Area_{CT}$ Eq. 4

The cost functions must converge to zero, indicating that the output variable predicted by the regression function for each patient aligns with the corresponding value obtained from CT imaging. The quadratic regression function resulted in two distinct sets of material parameters. The optimal set is chosen on the base of its being within the range of the elastic modulus variation. If both values fall within the range, a single value is selected as the best material parameter.

Once the optimal parameter is identified for each patient, a new simulation of the pre-TAVI heartbeat was conducted with the optimal parameter for both the aortic wall and valve leaflets. The distorted configuration of the aorta wall at peak systole was subsequently compared to its corresponding CT representation utilizing the Jaccard index to measure the degree of concordance between vessel shapes. The orifice area of native valve leaflets, estimated using optimal material characteristics, was compared to measurements obtained through imaging.

5.3 Results for the aortic wall

The optimal Young's modulus found was 5.6±1.3 MPa for the patient study group here investigated. The distorted configurations of the aorta wall, derived from simulations of the cardiac beat utilizing optimal Young's modulus, were juxtaposed with those from pre-TAVI angio-CT segmentations at peak systole for each patient using the Jaccard index to quantify the level of agreement among vessel shapes (Figure 5.3).

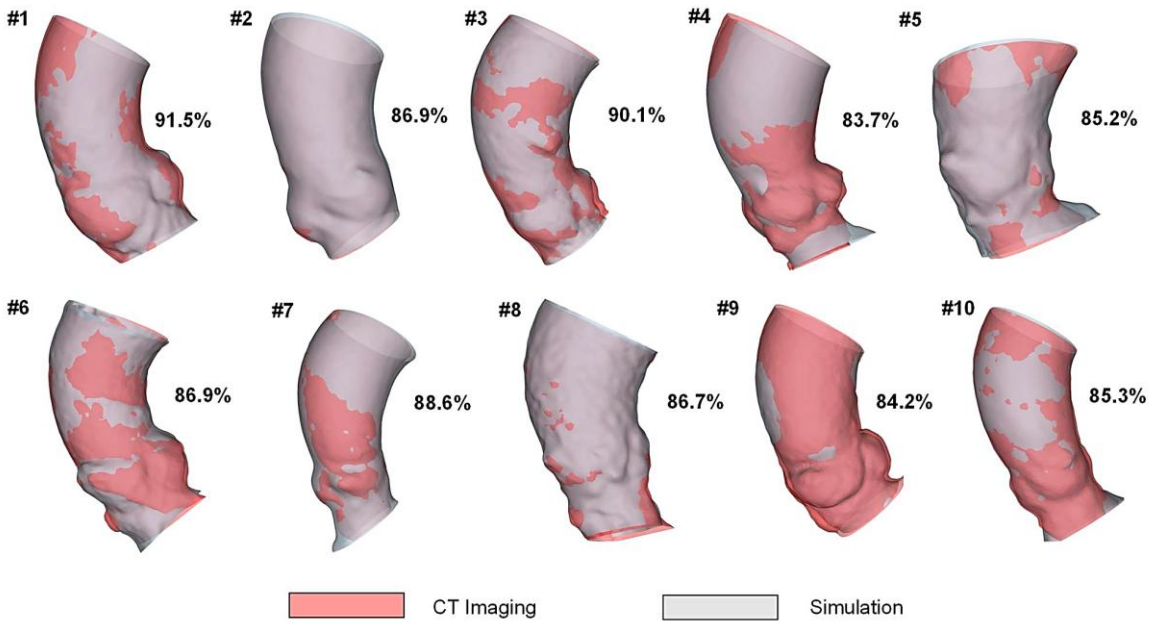

Figure 5.3. Comparison of peak systolic configuration between predictions and CT imaging for each patient and corresponding Jaccard index.

The most significant disparity was qualitatively noted in the left ventricular outflow tract, presumably attributable to the heart's kinematics distorting and twisting the aortic root. The Jaccard score demonstrated a substantial concordance between predictions and image-derived forms, reflecting a resemblance ranging from 83.7% to 91.5% within the patient cohort. Pearson's analysis revealed a negative linear correlation between the ideal elastic parameters for each patient and the strain derived from the pre-TAVI angio-CT ($R=-0.86$ and $p<0.001$, Figure 5.4).

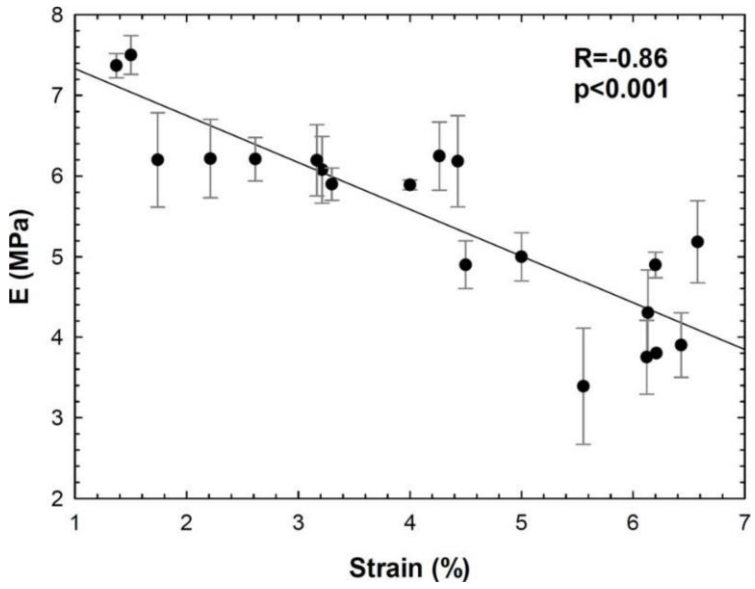

Figure 5.4 Pearson's analysis between optimized Young's moduli and CT-derived strain measurements.

5.4 Results for the calcified aortic valve

For the patient study group, the mean value of the elastic modulus was 10.4±3.1 MPa. Relative errors between predictions and CT measurements were in the range of 0.08% to 11.86%, suggesting a realistic biomechanical response of the modelled stenotic valve. No statistically significant difference was observed between the predicted and imaging observations. Figure 5.5 illustrates the opened configuration of the calcified valve at peak systole for three example individuals exhibiting moderate to severe calcification volumes.

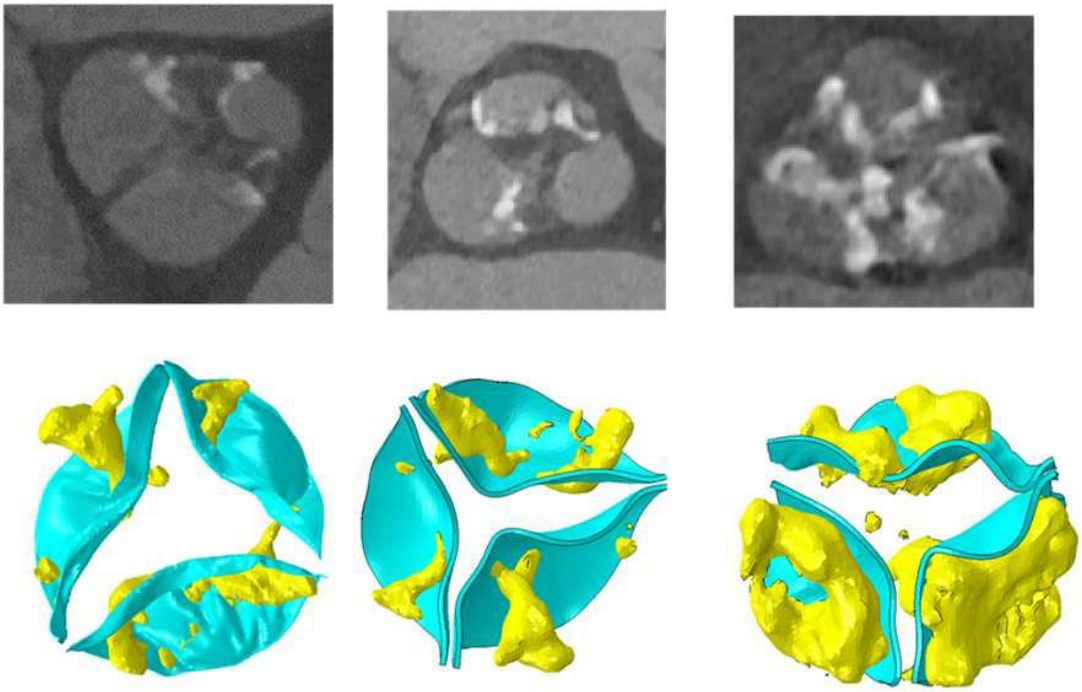

Figure 5.5. Qualitative assessment of the level of agreement between predicted and actual pre-TAVI configuration.

A negative correlation (Figure 5.6) was found between the optimal material parameter and the valve orifice area measured from the imaging ($R=-0.84$ and $p<0.001$).

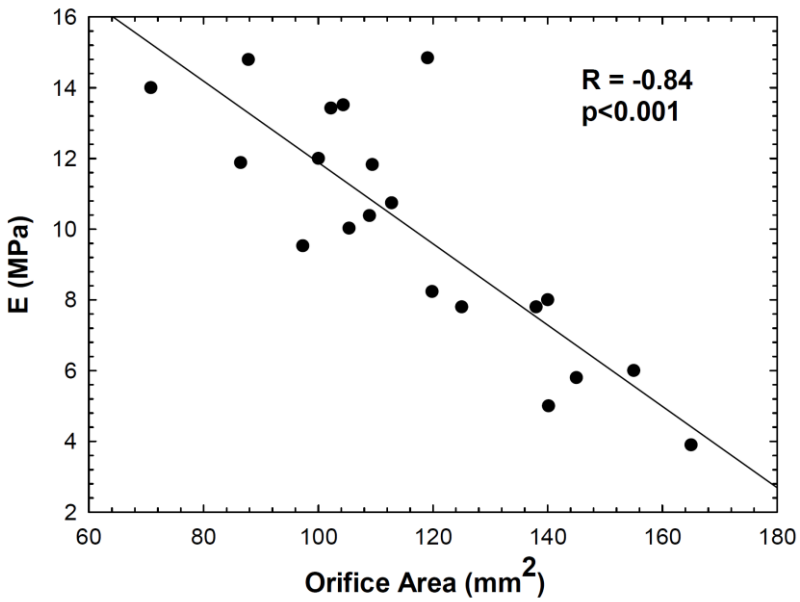

Figure 5.6. Pearson's analysis between optimized Young's moduli and CT-derived valve orifice area measurements.

5.6 Discussion

This study presents an innovative, non-invasive inverse method for accurately evaluating the material properties of the aortic root and calcified valve leaflets in patients with severe aortic valve stenosis undergoing TAVI. The proposed approach utilizes pre-TAVI angio-CT images at peak-systole and end-diastole, to optimize patient-specific elastic parameters through a regression model, aiming to minimize the discrepancies between predicted and CT-derived measurements of aortic wall strain and orifice area. The predicted systolic configurations of the vessel wall demonstrated strong agreement with real CT data, and similar outcomes were observed for the open configuration of stenotic valve leaflets, comparing predictions with imaging assessments.

Upon determining the optimal set of material parameters, TAVI simulations were performed to validate the inverse analysis by comparing the predicted S3 device diameter with post-TAVI angio-CT images. The predicted device diameters at various anatomical levels closely matched those obtained from medical imaging, with a diameter deviation of less than 10.5%. This suggests that the proposed inverse analysis method holds significant promise for improving patient care by facilitating the optimization of material parameters in an elderly population, where current material descriptors may be insufficient. Trabelsi at al. [102] previously demonstrated the efficacy of inverse analysis using imaging data to estimate the material parameters of the two-term Demiray constitutive model. Unlike the methodology here described, they used three cardiac phases (systole, mid-cycle, and diastole) to infer the

material properties, using the aortic wall volume as the output parameter. Their inverse analysis, performed on five individuals with aortic aneurysms, revealed a maximum relative error of 0.019% between numerically predicted and CT-derived measures of luminal vessel volume. However, there remains limited knowledge regarding the material properties of elderly individuals, as ex-vivo mechanical testing is typically unfeasible for this demographic [103, 104]. Martin et al. [105] conducted biaxial testing on eight fresh-frozen human cadaver hearts aged 80 to 98 years, revealing that human aorta tissue exhibits significantly greater stiffness than pig tissue in both circumferential and longitudinal orientations. These findings underscore the need for advancements in non-invasive inverse analysis. This study demonstrates a strong concordance between predictions and CT-derived measurements of biomechanical and morphological characteristics of the vascular wall before TAVI, as well as the structural arrangement of the implanted device after TAVI. While linear elastic models may adequately capture the biomechanical response in elderly TAVI patients, they also provide reliable computational predictions for TAVI simulations.

5.7 Challenges and Future Directions

Notwithstanding the advancements achieved in the material calibration and computational modeling of TAVI, several challenges persist. The non-invasive inverse analysis was limited to individuals who received the 23-mm S3 TAVI device. Though this approach may be applicable to various device types and sizes, a primary concern is the inconsistency in material properties among diverse patient populations, which may influence the precision of the simulations. Additionally, the assumption of equal material properties across the aortic root may inadequately represent the intricate biomechanical behavior of the tissue, which may differ in some region and may present thickness variation along the aorta's longitudinal axis. Subsequent research should concentrate on creating more advanced models that consider regional disparities in tissue characteristics and on incorporating uncertainty quantification into the modeling framework. This would enable more tailored simulations that could better predict clinical outcomes for specific individuals.

Chapter 6

Verification and validation of high-fidelity TAVI computational models

Establishing the credibility of TAVI models is essential, and verification and validation (V&V) are critical steps in achieving reliable and accurate computational simulations.

To accomplish this, a hierarchical approach must be taken, rigorously applying V&V activities at component level, ensuring that each part of the model is accurately represented. In this chapter, the methodologies used to verify and validate patient-specific computational models of TAVI are discussed. First, the V&V workflow is applied to each individual model component of the pre-TAVI scenario. Consequently, structural and fluid dynamic TAVI models were then evaluated using the ASME V&V40 protocol to ensure their overall credibility and reliability in clinical applications. The results of the study here discussed were published in [106, 107].

6.1 V&V Requirements

The ASME V&V40 framework was used to assess the credibility of the patient-specific TAVI structural and fluid dynamical model. The verification process ensures that the computational model accurately represents the underlying mathematical model and that the numerical methods used are implemented correctly. The evaluation criteria employed the relative error (RE) as defined by ASME V&V 10 [108]:

$$\varepsilon = \frac{(\omega_1 - \omega_2)}{\omega_1} \qquad \text{Eq. 5}$$

With $\omega_{i=1,2}$ referring respectively to the measured (or calculated) output of interest and the true (or reference) output of interest.

The question of interest (QoI) was defined as “Is the patient-specific model capable of accurately simulating the function of the stenotic aortic valve before TAVI?” From a clinical standpoint, the severity of calcified aortic valve failure is contingent upon the configuration of calcific plaques and the diminution of the orifice area during cardiac contraction.

The context of use (CoU) was established to predict the biomechanics of the aortic wall based on individual patient data. Due to the considerable heterogeneity in calcification patterns, annulus dimensions, and patient demographics, employing patient-specific

modeling to simulate the patient's situation prior to TAVI facilitates the prediction of aortic wall biomechanics.

Model risk definition accounted for the concepts of decision consequence and model influence. Decision consequence refers to the severity of the adverse outcome if the decision based on the model is incorrect, and model influence refers to the contribution of the model to the final decision [109]. Given the high variability in the patient cohort, the decision's impact was deemed significant: misjudging the valve size might substantially increase the patient's risk. Therefore, both the model's influence and the decision's consequence were classified as "high" and the model was designated a risk level of 5 on a 1-5 scale, signifying the necessity for elevated credibility objectives in the V&V plan. As a result, relevant parameter variations derived from simulations were limited to relative errors RE under 1%. However, considering the inherent accuracy of the adopted Smoothed Particle Hydrodynamics (SPH) method compared to conventional CFD methods, the verification requirement for the FSI model was set at 5%, balancing accuracy and computational feasibility. Errors arising from user input were not included in the analysis. Table III shows the credibility factors and associated level of rigor identified for the following V&V activities on the TAVI model.

Table III. Credibility factors and associated level of rigor employed.

Activity	Credibility Factor	Level of Rigor		Credibility Level
		Selected	Maximum	
Verification				
Code	Software Quality Assurance (SQA)	c	c	high
	Numerical Code Verification (NCV)	c	d	medium-high
Calculation	Discretization Error	c	c	high
	Numerical Solver Error	c	c	high
	Use Error	-	-	-
Validation				
Computational Model	Model Form	b	c	medium
	Model Input			
	Quantification of Sensitivities	c	c	high
	Quantification of Uncertainties	c	c	high
Comparator	Test Samples			
	Quantity	c	c	high
	Range of Characteristics	c	d	medium-high
	Measurements	c	c	high
	Uncertainty of Measurements	d	d	high
	Test Conditions			
	Quantity	b	c	medium
	Range	c	d	medium-high
	Measurements	c	c	high
	Uncertainty of Measurements	d	d	high
Assessment	Equivalency of Input Parameters	c	c	high
	Output Comparison			
	Quantity	b	b	high
	Equivalence of Output Parameters	c	c	high
	Rigor of Comparison	d	d	high
	Agreement of Comparison	c	c	high
Applicability of the Validation Activities to the COU				
Relevance of the QOIs		c	c	high
Relevance of the Validation Activities to the COU		c	d	medium-high

6.2 Case study 1: patient-specific TAVI structural model

A prospective clinical trial involving 20 patients was conducted, all of whom underwent TAVI using the Sapien 3 (S3) Ultra device. Pre- and post-TAVI ECG-gated CT scans were used to capture images during both the diastolic and systolic phases. As previously described, the aorta and calcification models were developed by segmenting the CT images using semi-automatic and fully automatic thresholding respectively. The aortic native leaflets were modeled by means of a parametric methodology relying upon anatomical landmarks and measurements. FEA of the pre-TAVI cardiac cycle was performed with Abaqus/Explicit. The aortic wall and valve leaflets were modelled with linear-elastic material characteristics, with Young's moduli obtained from the inverse analysis discussed in Chapter 5, while calcifications were represented using a neo-Hookean constitutive model with parameters C1= 67.7 MPa and D1 = 7.5E-3 MPa. Pressure waveforms were calibrated according to each patient's brachial pressure, and boundary conditions were applied to simulate the biomechanical behavior of the aortic root before TAVI [110]. The patient-specific heart rate was utilized to calibrate the duration of the pressure waveform. The native valve leaflets were exposed to a consistent pressure load, equivalent to the transvalvular pressure gradient assessed using echocardiography. The aorta wall's distal and proximal ends were restricted in longitudinal orientations, while tie connections were established between calcifications and valve leaflets.

Verification and validation activities were conducted on a component-level basis of the patient-specific TAVI platform.

6.2.1 Apply the ASME V&V 40 Framework

Verification activities were conducted for each structural component, i.e., aortic root, valve leaflets and calcification. The workflow included discretization error (DE), numerical solver error (NSE), and numerical code verification (NCV) estimation. These activities were performed in 5 patients from the subgroup of 20 patients. Mesh refinement and element formulation were investigated for each anatomical component to assess the effects of model discretization. The NSE analysis aimed to estimate the impact of different solver parameters on certain quantities of interest with respect to a baseline simulation. The solver parameters investigated were a) penalty factor, b) damping, c) viscous pressure, d) bulk viscosity, and e) contact parameters. For the NCV analysis, a representative benchmark problem was designated for each anatomical component of the patient-specific model. The benchmarks were then compared with analytical solutions to assess the model's ability to appropriately solve the fundamental mathematical equations governing vessel biomechanics. ECG-gated

CT scans at the systole were used as a comparator to validate the simulations for each patient. Specifically, the quantities of interest extrapolated were peak systolic strain and the valve orifice area, as previously defined in Chapter 5.

6.2.2 Discretization error assessment

Aortic root – The grid convergence analysis involved the assessment of both element type and size. The Von Mises stresses at mid-level of the ascending aorta were accounted as output parameter. The computational time was also regarded for the identification of the optimal element size. DE analysis for aortic wall was conducted with element size of 0.5 mm, 0.8 mm, 1.2 mm, and 1.5 mm and resulted in errors on Mises's stress of RE=0.25%, 0.87%, 6.4%, and 1.25%, respectively. An element size of 0.8 mm was considered acceptable to optimize both model accuracy and computational costs. Similarly, the triangular shell (S3) and the quadrilateral shell (S4) were investigated, leading to the identification of the S3 as the optimal element type, with RE of 0.76% for S3-tri versus RE of 1.25% for S4. Additionally, the S3 type effectively captured the complex geometric changes of the aortic wall.

Native valve leaflets – The DE involved the assessment of both element type and size. The mesh generation required the solid extrusion of shell elements outward to create 4 layers of prismatic elements. To prevent folding during simulations, element refinements along the thickness direction were tested with 2, 4, and 6 layers. The orifice area was used as parameter for comparison. The investigated element sizes (and RE) were 0.5 mm (0.29%), 0.6 mm (0.38%), 0.8 mm (5.1%) and 1.0 mm. Therefore, the element size of 0.6 was adopted. Three types of solid elements were investigated, including a) unstructured prismatic (C3D6), b) unstructured hexahedral and c) structured hexahedral (C3D8R) elements. Given the high morphological complexity, there was a prone tendency to significant element distortions with structured and unstructured hexahedral elements. For one representative case, the RE was 0.67% for the unstructured prismatic element, 24.1% for unstructured hexahedral and 23.3% for structured hexahedral element. Figure 4 shows the element mesh and the comparison between predicted and CT-based measurements. Therefore, prismatic elements were considered the optimal choice to better follow the leaflets shape that at the same time allowed to avoid element distortions.

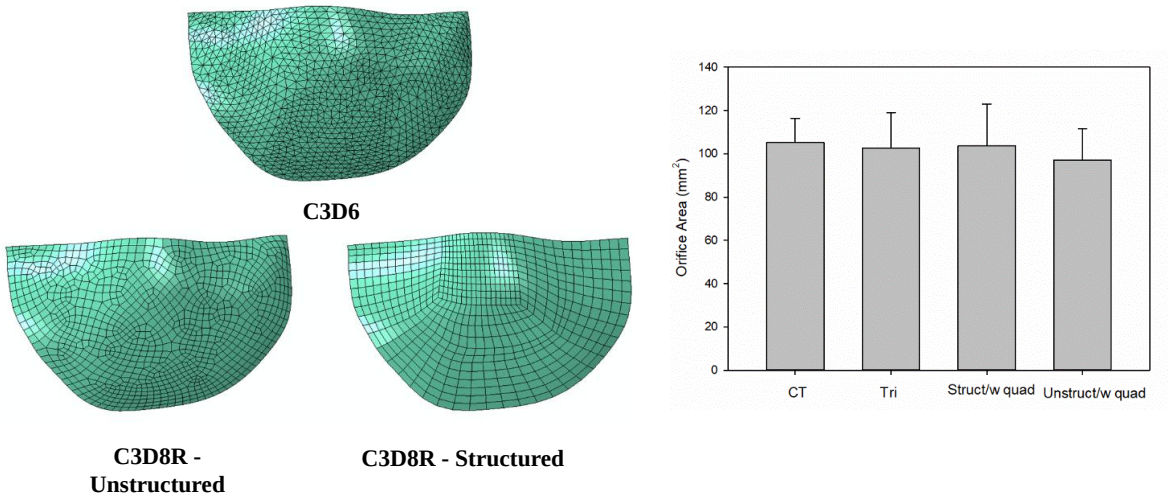

Figure 6.1. investigated element type (left) and orifice area comparison between the investigated typology and the real CT measurements.

Calcifications – Since calcifications exhibited a complex and irregular shape the tetrahedral solid elements (C3D4) were adopted as this were the only element type that reasonably described the calcific plaques. The investigated element mesh sizes and corresponding REs were 1 mm, 0.8 mm (61.25%), 0.6 mm (20.74%), and 0.5 mm (0.92%), using the principal Cauchy stress as the output parameters. Therefore, the element size of 0.5 mm was selected.

6.2.3 Numerical solver error assessment

NSE analysis examined the effect of different values of solver parameters, i.e., penalty factors, damping, and bulk viscosity, with respect to a baseline model. The baseline model, whose main features are presented in Table IV, simulates the patient's cardiac beat using clinical data to specify the boundary conditions as described in Chapter 4. Main solver parameters were identified by keeping the REs below 1%. The analyzed FEA was developed using grid refinements resulting from the discretization investigation. A default time increment value of 1 was selected due to the low loading rate. Mass scaling with values of 5.0e-6 and 1.0e-6 and frequencies of 1 and 10 were tested and resulted in a ratio of kinetic to internal energy <1% in both cases. Raleigh damping was investigated varying the value from 40 to 2000 and observing the oscillations (i.e., displacement) occurring at the early diastolic phase. Analysis demonstrated that a damping factor of 250 allows to mitigate undesired high-frequency oscillations while preserving model credibility (RE=0.85%). Though not altering the wall-clock time, the increase in the viscous pressure applied to both the aortic wall and calcific valve leaflets resulted to model response deviations with RE>1%. Changes in the bulk viscosity parameter did not significantly affect the model response, except for a magnitude of 0.6 slightly impacting the wall-clock time. Varying friction

coefficients in contact interaction did not result in deviations in the system response or computational time.

Table IV. Baseline reference simulation main parameters.

Mass scaling [-]	None
Penalty scale factor [-]	None
Friction coefficient [-]	0.0
Mass proportional damping [s-1]	0.0
Stiffness proportional damping [s]	0.0
Number of CPUs [-]	60
Viscous pressure [MPa]	0
Bulk viscosity	0.06 (Default)

6.2.4 Numerical Code Verification

NCV was performed to evaluate the goodness of the mathematical implementation. This was accomplished by solving representative problems with known analytical solutions for each tested part maintaining the same solving parameters adopted for the simulations.

Aortic root – Given the physiological working conditions of the aortic wall the Laplace's law analytical solution was compared to the benchmark problem of a thin cylindrical shell under hydrostatic pressure and small deformation:

$$\sigma = \frac{P*r}{t} \qquad \text{Eq. 6}$$

where P is the internal pressure on the cylindrical surface, r is the radius of the vessel (i.e., 10 mm) and t is the vessel thickness. For the NCV study, a hollow shell cylindrical geometry was generated based on element type, mesh refinement, boundary conditions and other parameters determined by DE and NSE analyses for the aorta. Upon solving the computational problem, a RE of 0.6% was observed between numerical (31.82 kPa) and analytical (31.66 kPa) solutions.

Native valve leaflets – During cardiac cycle, the calcified valve leaflets can experience stretching, bending and shearing; however, the bending was considered as the predominant stress loading condition. Therefore, the representative problem of a cantilever beam was proposed. The cantilever beam (25 mm as length, 0.25 mm as height and 0.5 mm as width)

was discretized as determined by DE. Similarly to what was done for the leaflets modeling, the beam was realized by solid extrusion of a shell mesh with 4 layers through the thickness. One edge of the beam was constrained in all directions, while a concentrated force was applied to the free end of the cantilever beam. The simulation yielded a maximum deflection of 7.944 mm as compared to the analytical solution of 8.010 mm, with a RE=0.771%.

Calcifications – As calcifications being primarily compressed by the surrounding tissues during TAVI, a cube model under a uniform displacement condition was used for numerical validation. The solid model was meshed with tetrahedral elements and then subjected to an arbitrary displacement (i.e., compression) to calculate the resulting elastic deformation (i.e., nominal strain). After solution, the RE was 0.77% between predicted (0.0200) and analytical solutions (0.0198) of the nominal strain.

6.3 Case study: patient-specific TAVI SPH models

Starting from the structural patient-specific TAVI platform described previously, an FSI model underwent V&V is here presented. The FSI approach relied upon the smoothed-particle hydrodynamics (SPH) technique implemented in ABAQUS.

6.3.1 Patient-specific FSI TAVI model description

SPH is a comprehensive Lagrangian modeling technique that discretizes continuous equations by interpolating particle attributes within the solution domain via a kernel function W. This method computes values at a designated position by employing the characteristics of adjacent particles [111, 112]. The whole workflow entailing the patient-specific SPH TAVI model is shown in Figure 6.2.

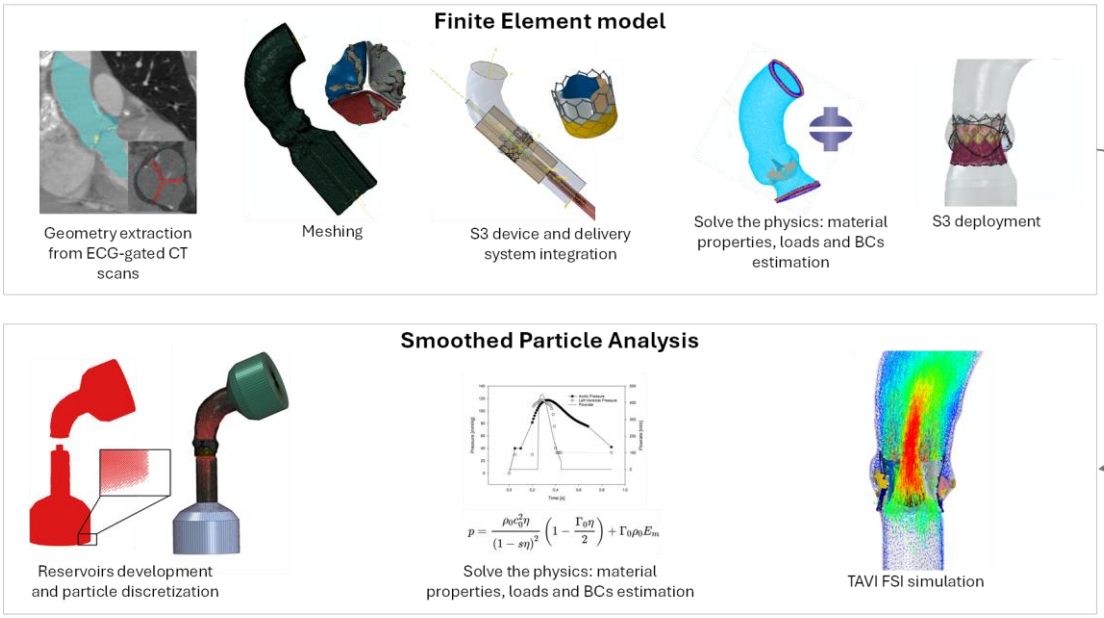

Figure 6.2. comprehensive patient-specific SPH TAVI model workflow.

Upon completing the patient-specific structural TAVI simulations, described in the previous chapters, the SPH TAVI model is generated. The latter was also implemented in ABAQUS receiving as input the deformed geometries of the patient model featuring the deployed S3 Ultra device.

Beginning with the deformed anatomical configuration of the deployed S3 Ultra device, patient-specific SPH simulations were conducted using the Abaqus solver, maintaining the default cubic kernel formulation. A dummy model was created to facilitate particle discretization and collection, with two fluid reservoirs strategically attached to each end of the aorta using tie constraints. The geometries of the reservoirs were designed in the CAD software Rhinoceros (v.5.5, McNeel & associates, SP), utilizing the plugin Grasshopper to create a parametric model that configures the reservoir shape and attachment to each patient's anatomy. Both reservoirs, namely the aorta reservoir and left ventricle (LV) reservoir were discretized with surface elements lacking assigned stiffness, allowing their volumes to fluctuate during cardiac simulations. The assembly of aorta and reservoirs were also discretized with solid tetrahedral elements (C3D4), enabling the creation of the SPH particles. Indeed, once the reservoir geometries were modelled, the fluid domain was defined by generating the SPH particles by converting the solid domain in discrete particle elements. The SPH particles were created through background grid conversion in a data-check job. The solid model through which particles are generated and the full patient-specific TAVI SPH model are shown in Figure 6.3.

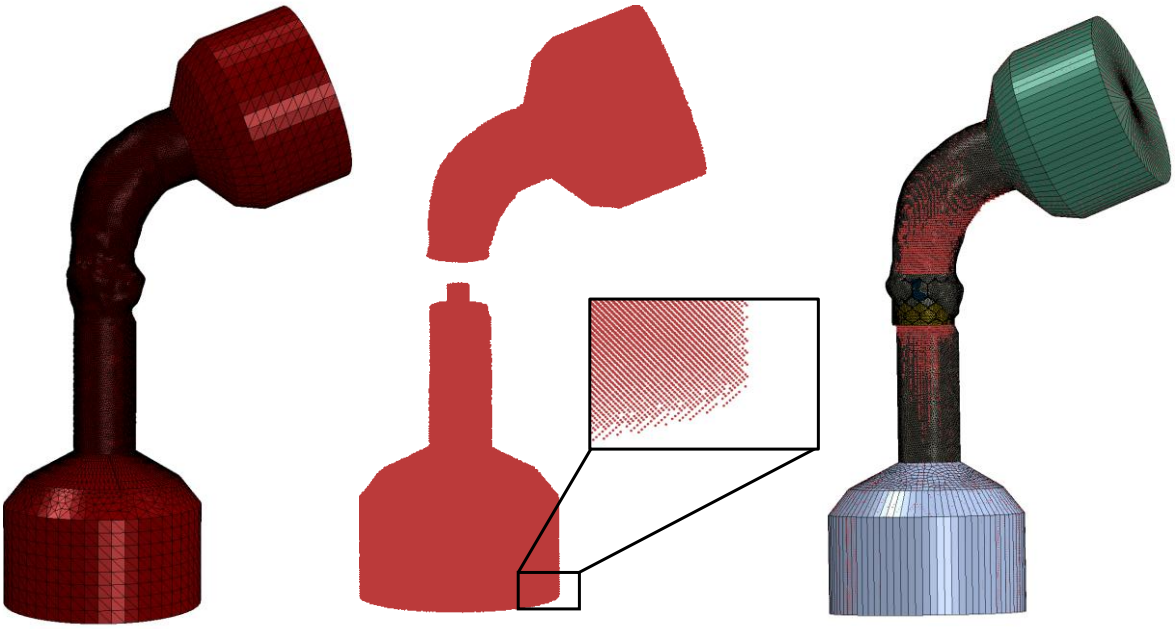

Figure 6.3. Solid mesh of aorta and reservoirs and particle distribution (left); Patient-specific TAVI SPH full model (right).

The fluid domain, i.e. the blood, was defined by an equation of state with the linear Hugoniot form. Blood was assumed incompressible and Newtonian. Particle discretization and material properties were summarized in Table V.

Table V. Particle discretization and material properties of the fluid domain.

Particle diameter	0.9 mm
Density, ρ	1.0E-09 tonne/mm^3
Wave speed, c_0	7.5E+04 mm/s
Grüneisen ratio, Γ_0	0
Hugoniot curve slope, s	0
Viscosity, η	3.0E-09 Mpa*s
Bulk viscosity damping coefficient	0.006

Interactions between the fluid particles and the patient-specific TAVI model were defined as contact pairs within the general contact definition, enabling the interaction between solid parts and particles and ensuring a realistic simulation of post-TAVI hemodynamic.

Heart rate, cuff pressure, and aortic jet velocity specific to the patient, obtained via transthoracic echocardiography, were employed to calibrate the duration and offset of physiological waveforms related to pressure and flow. Figure 6.4 displays pressure and flow rate waveforms tailored for a representative patient.

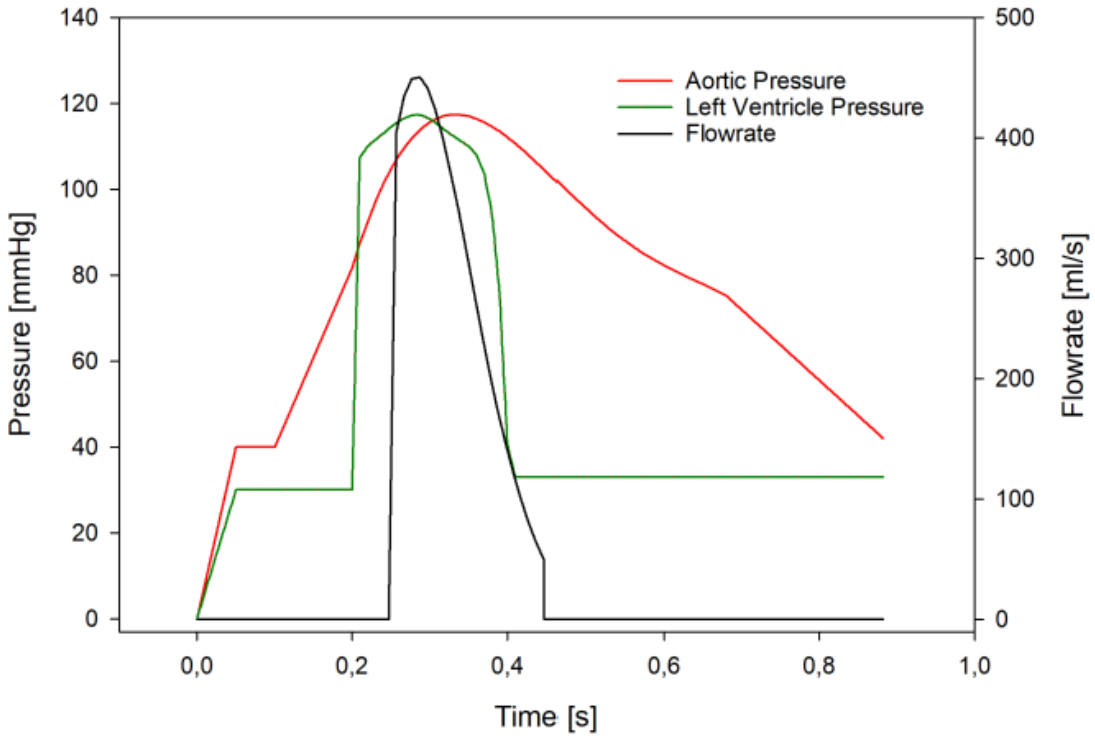

Figure 6.4. Physiological pressure and flow rate waveforms derived from patient-specific clinical data.

During the systolic phase, the flow is governed by the flow rate curve, which is converted to a velocity boundary condition on the LV reservoir. This determined blood particle motion towards the deployed device by mimicking LV chamber contraction. During the diastolic phase, the velocity boundary condition is deactivated, and LV and aortic pressures control the flow due to the pressure difference to favour the development of a reverse flow and valve leaflet closure. The aortic reservoir behaved as a fluid collector during systole and contracts during diastole to simulate in-vivo arterial compliance. Switching the flow boundary condition on and off is achieved by using a single truss element with temperature-dependent stiffness properties. The vessel is initialized with a load condition derived from the structural TAVI simulation, which is then imported into the SPH model using a predefined field. Specifically, at the start of the fluid simulations, the device leaflets are in a stress-free state, while the elastic recoil of the aortic root and calcified valve leaflets is balanced by the radial force exerted by the expanded device frame.

6.3.2 Model output of interest

Flow sensor points were strategically employed to detect flow pressure and velocity variations over time on both the left ventricle and aortic sides of the post-TAVI patient-specific model. By exploiting the flow pressure and velocity curves obtained from the simulation, main quantities assessing valve performance were computed according to ISO 5840-1 standard [113]. Specifically, outputs of interest were systolic jet velocity, effective

orifice area (EOA), mean and peak pressure gradient (PG), and stent diameter at inflow, midflow and outflow levels. Geometric orifice area (GOA) over time is presented Figure 6.5.

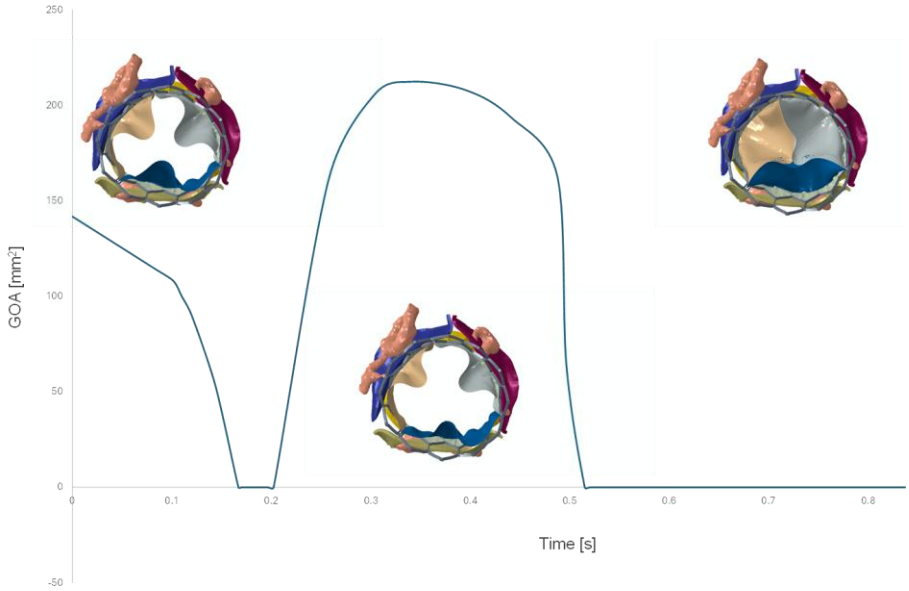

Figure 6.5. GOA computed over time.

The EOA (cm^2) was computed using Gorlin's equation [38]:

$$EOA = \frac{Q_{RMS}}{51.6\sqrt{PG}} \qquad \text{Eq. 7}$$

Where PG (mmHg) denotes the transvalvular pressure gradient during forward flow, and Q_{RMS} (ml/s) represents the root mean square value of aortic flow over the same averaging interval.

6.3.3 Apply the ASME V&V 40 Framework

The SPH model was verified and validated following the ASME V&V40 framework. REs were kept under 5% for SPH simulations due to the inherent method limitations compared to traditional CFD techniques. DE was evaluated to analyse the influence of different particle sizes on the outputs of interests. As an extensive NSE estimation has been already conducted for the TAVI structural model, here the investigated parameters were mass scaling and viscous pressure.

Discrete validation was carried out for estimating the discrepancy between the predicted outputs of interest and the actual measurements. Post-TAVI echocardiography data and post-TAVI CT scans were chosen as the comparators. Aortic jet velocity, peak and mean PG,

EOA, and stent diameter at inflow, midflow and outflow levels were analysed and compared against the patient-specific simulation results.

To estimate accuracy, empirical cumulative distribution functions (ECDFs) were plotted and compared between the real data and the simulation observations. The degree of agreement between the simulation and the empirical data was numerically quantified by computing the area metric:

$$Area\ Metric\ (\%) = \frac{|A_{Simulation} - A_{Clinical}|}{A_{Clinical}} * 100 \qquad \text{Eq. 8}$$

This approach provided a robust measure of the model's predictive accuracy, ensuring that the simulation results closely align with clinical observations.

Applicability analysis is accounted to evaluate the relevance of a credibility assessment activity (e.g., validation activities) to support the use of the computational model for a given CoU. In the context of TAVI SPH models, the relevance of the quantities of interest accounted in the validation and the relevance of the validation activities to the CoU were assessed [114].

6.3.4 Results

Velocity fields and pressure distributions during systole and diastole phases exhibited consistent patterns with expected physiological behaviour. Flow velocities at different phases of the cardiac cycle are shown in Figure 6.6 for a representative patient-specific TAVI SPH model. Notably, a strong flow jet emerges during the systole phase from the opened device valve leaflets, while at diastole, an efficient sealing of the leaflets is achieved, preventing reverse flow.

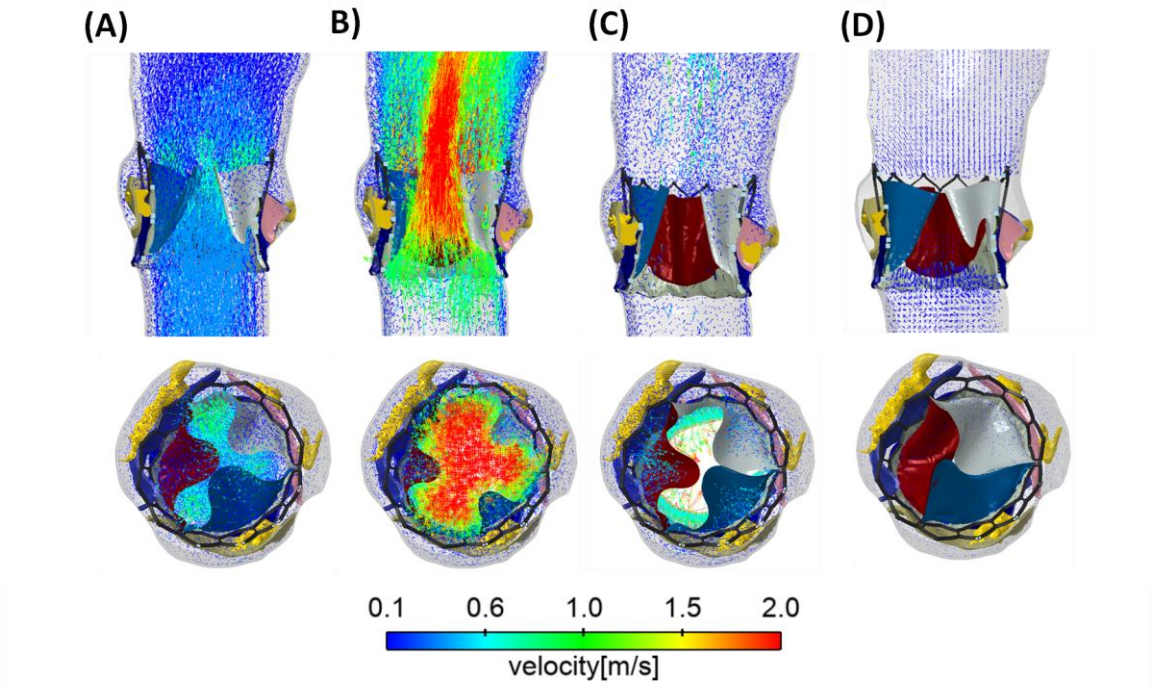

Figure 6.6. Flow velocities for a representative patient case at A) acceleration, B) systole, C) deceleration and D) diastole phases.

For n.20 patient-specific SPH simulations, the peak velocity was 2.44±0.45 m/s compared to the echocardiographic evaluation of 2.50±0.41 m/s, the SPH-related EOA was 1.47±0.45 cm2 with respect to the echocardiographic evaluation of 1.40±0.37 cm2, the SPH-related mean PG was 15.30±4.75 mmHg versus the clinical estimation of mean PG 13.67±4.55 mmHg, while the peak PG was 29.96±8.30 mmHg against the clinical estimation of peak PG 27.35±7.5 mmHg.

A grid convergence analysis was performed for particle sizes of 0.9 mm, 1.15 mm, 1.4 mm, and 1.7 mm, with 0.9 mm as the reference size. Computation of REs did not show a monotonic increase with the size, with exception of GOA, which presented a positive correlation with values of 5.6%, 7.44%, and 13.79% for sizes of 1.15 mm, 1.4 mm, and 1.7 mm respectively.

For the NCV, the parabolic velocity profile at the left ventricular outflow tract level was compared to the parabolic velocity profile of a pipe under laminar flow, as defined by Poiseuille's Law [115]. Given the elliptical nature of the left ventricular outflow tract (L=50 mm), the minor radius of 6 mm was used for the theoretical calculation of blood velocity. All settings were derived from DE and NSE estimations. Assuming a PG of 4 mmHg, the peak velocity was computed with an RE of 9% between the numerical and analytical solutions.

NSE was carried out to assess the impact of solver settings on the response of the S3 device within the patient-specific scenario. Specifically, stable target time increments of 0.5e-6 s, 1.0e-6 s (reference), and 2.5e-6 s and viscous pressures of 1.4e-5 MPa, 1.0e-6 MPa (reference), and 9.0e-6 MPa were investigated. Table VI presented the different model configurations adopted, and the REs obtained in the SPH outputs of interest for the parameters under study. Overall, mass scaling did not show significant influence on GOA and EOA with neglectable deviations among the configurations. Instead, velocity and PG significantly varied among configurations, leading to the adoption of 2.5e-6 value for the target time increment. Viscous pressure presented a reference value of 1.4e-5 MPa with deviations neglectable among the configurations, therefore the reference value was adopted, indicating its efficacy in accurately capturing relevant dynamics without introducing significant deviations.

Table VI. Simulations run for NSE assessments and outputs of interest with related REs.

Case ID	Mass Scaling (s)	Viscous Pressure (MPa)	Particle Diameter (mm)	CPUs (-)
#1 Baseline	1.0e-6	1.0e-6	0.9	60
#2 Mass Scaling 2.5	2.5e-6	1.0e-6	0.9	60
#3 Mass Scaling 0.5	0.5e-6	1.0e-6	0.9	60
#4 Viscous Pressure 1.4	1.0e-6	1.4e-5	0.9	60
#5 Viscous Pressure 9	1.0e-6	9.0e-6	0.9	60

Case ID	Velocity (m/s)	RE (%)	PG (mmHg)	RE (%)	GOA (mm^2)	RE (%)	EOA (mm^2)	RE (%)
#1 Baseline	3.53	-	49.84	-	206.40	-	169.84	-
#2 Mass Scaling 2.5	3.13	11.33	39.19	21.38	208.12	0.83	175.05	3.06
#3 Mass Scaling 0.5	2.73	22.66	29.82	10.48	206.02	0.10	173.28	2.02
#4 Viscous Pressure 1.4	3.34	22.66	44.62	10.48	206.02	0.18	171.94	1.23
#5 Viscous Pressure 9	3.27	7.37	42.77	14.19	209.73	1.61	180.44	6.23

Validation was performed by comparing the simulated results with clinical data obtained from the patient cohort. Key parameters were (a) EOA, (b) peak PG, (c) mean PG, (d) inflow diameter, (e) midflow diameter and (f) outflow diameter. Figure 6.7 illustrates the empirical ECDF functions plotted for each patient for both the real clinical measurement and the corresponding model prediction. A visual comparison of these curves demonstrated that the

simulation resulted closely aligned with the patient observations. The area metric values achieved were reported in Table VII.

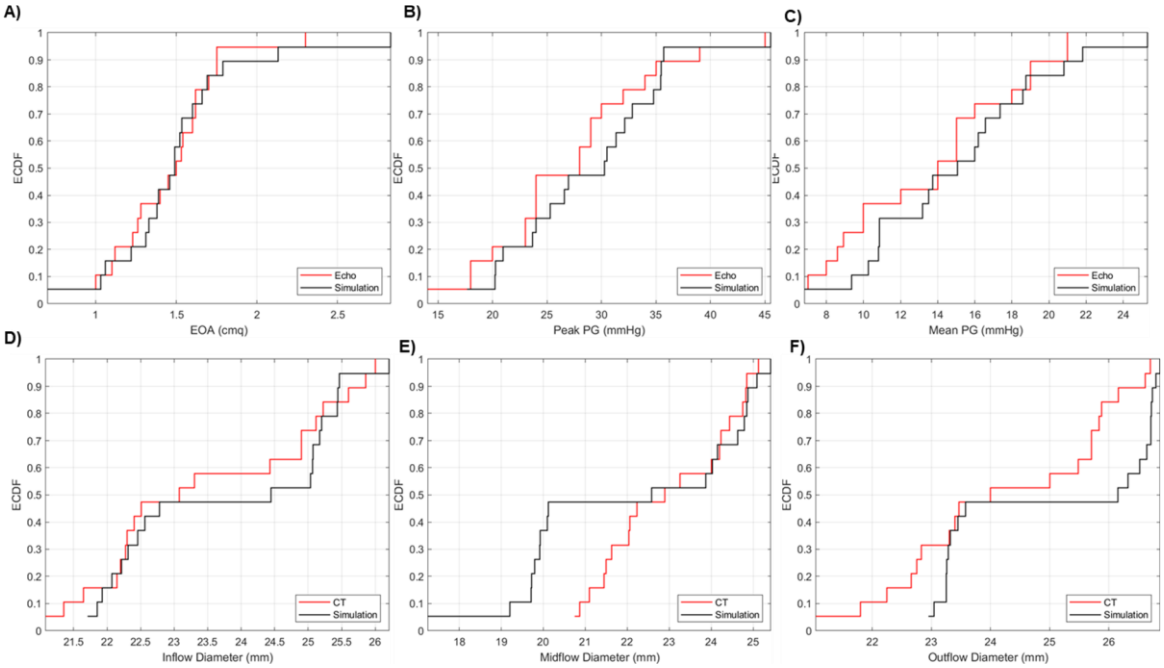

Figure 6.7. Empirical CDF plots for both the actual measurements and the predictions of (A) EOA, (B) peak PG, (C) mean PG, (D) inflow diameter, (E) midflow diameter and (F) outflow diameter.

In Figure 6.8 the RE of each quantity of interest was evaluated with respect to a needed confidence, i.e., probability.

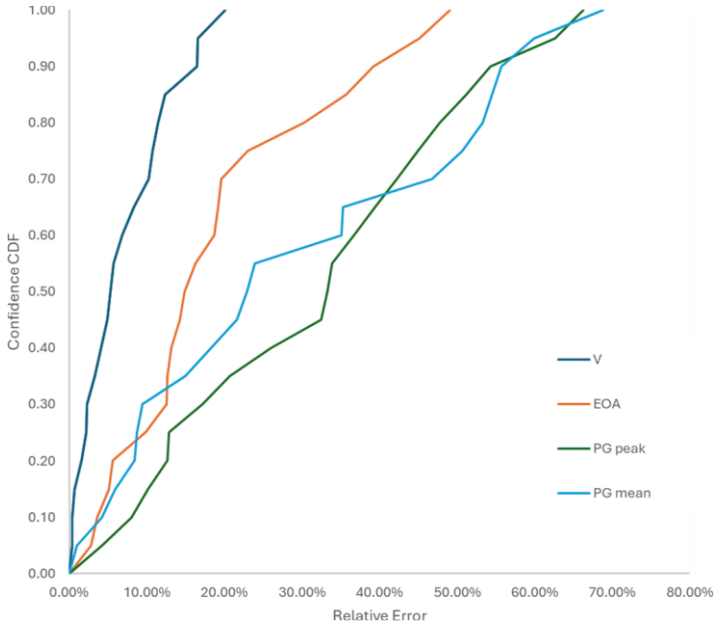

Figure 6.8. Predictions probability confidence against associated REs computed among the different variables.

Relevance of the quantities of interest: The quantities of interest accounted for the prediction accuracy were the EOA, mean and peak PG, inflow, midflow and outflow stent diameter.

These variables were considered related to the declared CoU. Relevance of the validation activities to the CoU: The validation activities outlined in the study are highly relevant to the CoU as they ensure that the TAVI computational model is reliable and accurate in predicting clinically significant outcomes. By focusing on critical hemodynamic parameters, comparing simulation results with clinical data, and using robust statistical measures, the validation process supports the credibility and applicability of the model in clinical practice.

Table VII. Output of interest and corresponding area metric (M).

Output of interest	**M (%)**
Velocity	5
EOA	6.3
Peak PG	9.6
Mean PG	12.2
Inflow Diameter	1.5
Midflow Diameter	5.15
Outflow Diameter	3.13

6.4 Discussion

This study demonstrated the successful application of ASME V&V 40 standard to patient-specific computational models of TAVI on both structural and SPH models. By following the ASME V&V40 framework, a rigorous credibility evaluation is of these models is provided. Very few studies applied the standard to cardiac in-silico models. Pathmanathan et al. [114] suggested a systematic approach for evaluating the relevance of validation evidence to the proposed context of use, focusing on the applicability of in-silico models to specific engineering domains. Ramella et al. [116] performed an applicability analysis of numerical models of thoracic endovascular aortic repair. Luraghi et al. [90] conducted verification activities for structural simulations of thrombectomy operations using idealized tri-leaflet heart valve models. Tango et al. [91] focused on verifying a computational flow model of the aortic valve by juxtaposing predicted velocity fields with in-vitro data.

The main findings of this study were an accurate depiction of the biomechanical response of the pathologic aortic root and valve before TAVI, validated through comparison with imaging data as well as the accurate acute structural and hemodynamic response for a given patient-specific geometry following TAVI. In the case of the structural TAVI model, the model's reliability was strengthened through mesh refinement and solver error analyses, yielding REs of less than 1%, which aligns with high-risk clinical and regulatory standards.

The patient-specific SPH TAVI model enabled the accurate simulation of post-TAVI hemodynamic. The SPH technique captured key hemodynamic features, such as peak systolic velocity, effective orifice area (EOA), and pressure gradients, demonstrating a strong agreement with clinical echocardiographic data, with area metric values in the range of 1.5%-12.2%. The measurements demonstrated a high degree of accuracy in the simulation findings, affirming the reliability of our computational model in mirroring the actual clinical outcomes following TAVI. Velocity estimations maintained high confidence at very low values of REs, suggesting a good balance of model's confidence and performance. According to the author's knowledge this is the first work presenting a complex and precise SPH TAVI simulation that incorporates fluid-solid interaction and has undergone stringent verification and validation activities to enhance the model's reliability. Our findings underscored the importance of incorporating patient-specific anatomical and boundary conditions in computational modeling to accurately simulate post-TAVI hemodynamic. The developed in-silico tool not only enhances the understanding of post-TAVI hemodynamic but also holds promise for future applications in biomedical device testing and computer-based clinical decision support systems. These advancements have the potential to improve patient outcomes by informing the design and testing of cardiovascular devices. V&V activities conducted for both structural and SPH TAVI models, guided by the ASME V&V40 framework, confirm the reliability and robustness of these patient-specific simulations. These models not only provide a strong foundation for pre-procedural planning but also offer insights into post-procedural outcomes, potentially improving patient care and supporting regulatory decisions in cardiovascular interventions.

6.5 Challenges and Future Directions

However, current models, though accurate, are still limited by assumptions about tissue mechanics and model simplifications. Future research should focus on refining these models by incorporating more advanced material models and machine learning techniques to improve their predictive capabilities. Uncertainty quantification will also be crucial to further enhance model credibility, ensuring they can handle the diversity of patient profiles encountered in clinical practice. As computational models increasingly integrate into clinical practice, continuous attempts to standardize verification and validation methods and to develop more robust models will be crucial for maintaining their dependability and utility.

Chapter 7

Transcatheter mitral valve replacement simulations

TAVI is also increasingly being used in "off-label" scenarios, for treating mitral valve pathologies. This procedure, known as transcatheter mitral valve replacement (TMVR), has emerged as a viable alternative for patients with severe mitral regurgitation, particularly for those at elevated surgical risk or those who have not succeeded with previous surgical procedures. Despite its potential, TMVR presents considerable difficulties owing to the intricate anatomy and dynamic function of the mitral valve, which may result in life-threatening complications due to left ventricular outflow tract (LVOT) obstruction. This chapter explores the computational methodologies used to assess TMVR, with a focus on understanding and mitigating the risks associated with LVOT obstruction. Results of this study were published in [117, 118].

7.1 Background and Challenges

Mitral regurgitation (MR) is among the most prevalent valvular heart disorders, affecting 10% of the general population. Conventional surgical repair or replacement is frequently impractical for patients with elevated surgical risk due to comorbidities or advanced age, potentially resulting in mortality rates between 7.4% to 15.1% [119]. In this setting, transcatheter mitral valve replacement (TMVR) has gained increased interest as a novel and less invasive treatment for patients with significant regurgitation and high risk of conventional mitral valve surgery [120, 121]. This procedure is typically conducted to address individuals who have experienced several instances of mitral valve failure, which may include the existence of failed bio-prostheses (valve-in-valve, ViV), unsuccessful annuloplasty (valve-in-ring, ViR), and mitral annular calcification (valve-in-MAC, ViMAC).

TMVR is performed with THVs designed for the aortic valve used “off-label”, representing a challenging procedure as the mitral valve has a unique annulus structure which highly differentiates from the AV [122-124]. Thus, simulating TMVR is more challenging than simulating TAVI because of the complex structure of the mitral valve and its dynamic function. Unlike the aortic valve, the mitral valve is a large saddle-shaped structure that experiences significant dynamic forces during the cardiac cycle. The presence of a defective ring or bioprosthesis, or substantial calcification can increase the process complexity.

Generally, the procedure consists of implanting in mitral position an aortic THV that allows for adequate sealing and anchoring, allowing to accommodate the failed mitral valve annulus and its motion during the beating of the heart. As the device permanently displaces the native anterior mitral leaflet (AML) towards the basal septum, this technique poses the adverse risk of narrowing the left ventricular outflow (LVOT) tract [125, 126]. The newly created elongation is known as neo-LVOT and is a major concern of TMVR procedure threatening hemodynamic complications (Figure 7.1).

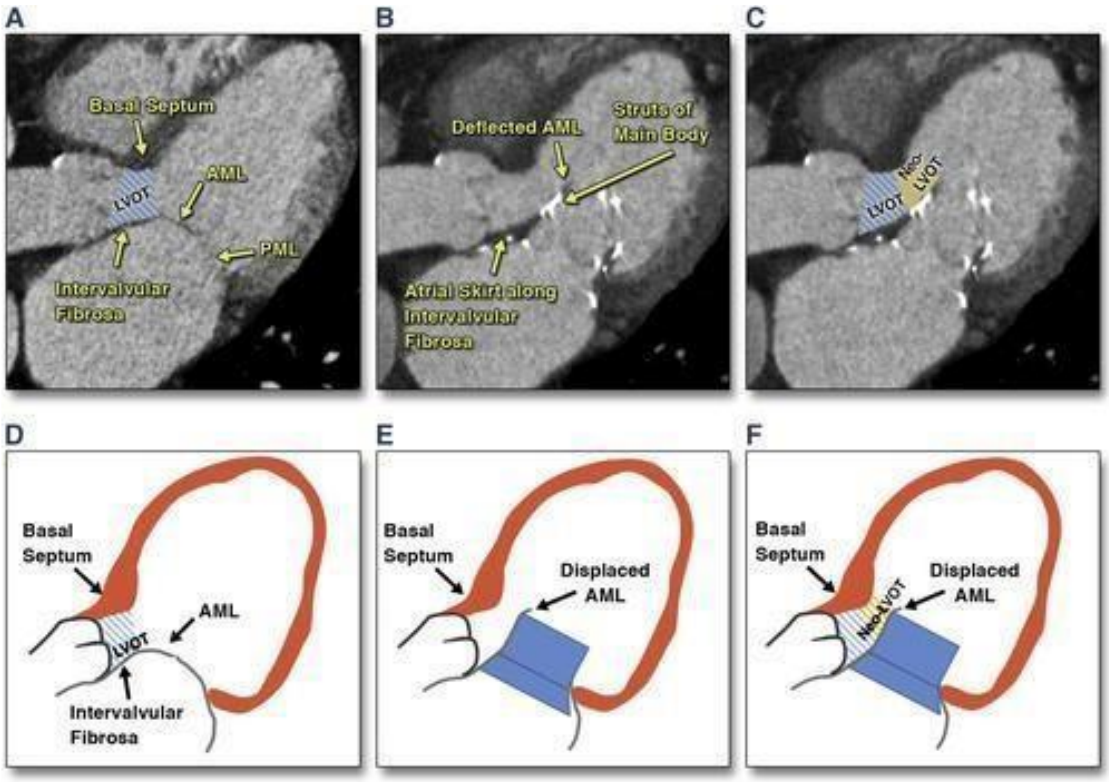

Figure 7.1. LVOT narrowing process following THV implantation in mitral position. With permission from Blanke et al. (2017).

This protrusion of the device into the original LVOT is a potentially fatal complication, occurring in around 7% to 9% of total TMVR procedures [127]. According to current clinical trials, about 50% of patient candidates for TMVR are excluded based on LVOT obstruction [128]. Additionally, the risk of LVOT obstruction may vary among specific patient populations [129]. In the setting of failed bioprosthesis (i.e., ViV), the risk of LVOT obstruction is strongly related to the initial implant, with height rather than size significantly influencing the extent of the obstruction. The incidence of LVOT obstruction in this cohort of TMVR patients ranges from 2.2% to 2.6% [130]. Similarly, mitral ViR is associated with increased obstruction rates, occurring in 5% to 8% of procedures in a multicenter study [84]. The characteristics of the annuloplasty band ring (i.e., rigidity versus flexibility) can influence the extent of device adaptation to the dysfunctional mitral valve; nevertheless, ring

compliance appears to have no impact on patient outcomes. In patients with ViMAC, LVOT obstruction is the principal factor influencing negative outcomes, with post-TMVR clinical trials revealing a mortality rate up to 45% [129].

The only method for risk stratification of patients with borderline anatomies at high risk of developing LVOT obstruction is pre-procedural CT imaging. Successful predictions of risk rely on the utilization of CT images to measure the minimal area confined by the implanted device and the basal septum corresponding to the LVOT obstruction. This region, known as the "neo-LVOT", is a reliable indicator of TMVR-related complications.

7.2 Modeling TMVR

Although the importance of exploiting CT data to create anatomically precise models for in-vitro device bench testing has been proven [131], there has been limited research on predictive models of neo-LVOT using in-silico methods [118, 132-134]. Undoubtedly, patient-specific simulations can overcome the limitations of a conventional geometric analysis, as the one suggested by Blanke and colleagues [125] to estimate the neo-LVOT region based on the virtual implantation of the THV within the patient's anatomy. Kohli and collaborators [131] developed computational flow analysis to simulate TMVR, observing an increase in flow velocity and a pressure drop across the neo-LVOT. Similarly, De Vecchi et al. [135] conducted multiple CFD analyses for varying levels of LVOT obstruction. A substantial rise in left ventricular afterload was observed to sustain cardiac output, indicating a decline in systolic flow efficiency relative to the severity of LVOT obstruction. Nevertheless, these investigations did not incorporate heart wall compliance or consider unique THV properties and designs. In a different way, Pasta et al. [134] simulated LVOT obstruction in transcatheter mitral ViR replacement and showed strong concordance between the numerically anticipated and CT-derived measures of the neo-LVOT region created by the Sapien 3 device. These findings are pertinent to bridging the knowledge gap regarding TMVR when the bioprosthesis is utilized off-label for mitral valve disorders [134]. As technology progresses, an enhanced comprehension of these processes will further optimize treatment strategies and advance patient outcomes.

7.3 Case study 1: In-silico and in-vitro assessment of neo-LVOT area in ViR, ViV and ViMAC

This study integrated in-silico computational modeling and 3D printing to estimate the neo-LVOT area and evaluate the biomechanical performance of implanted devices in patients with ViR, ViV, and ViMAC. The correlation between neo-LVOT area measurements obtained from post-TMVR CT imaging and in-silico predictions, as well as 3D printed

models, was evaluated. Computational fluid dynamics was employed to measure the pressure drop adjacent to the narrowed LVOT, thereby assessing the hemodynamic dysfunction caused by the device implantation. Results of the following study have been published in [117].

7.3.1 Patient study population

The study cohort included seven patients who received transapical TMVR using the Sapien 3 Ultra device (Edwards Lifesciences, Irvine, CA) at the ISMETT IRCCS organ transplant institute. The TMVR cohort comprised 2 patients with ViR, 3 patients with ViV, and 2 patients with ViMAC. Patients with ViR had a prior history of annuloplasty with the Sorin Memo 3D ring (Sorin Group Italia SrL, Italy), subsequently experiencing multiple instances of mitral valve failure (ViR-Case#1) or left ventricular dysfunction (ViR-Case#2). Patients with ViV exhibited mitral valve dysfunction of a prior bioprosthetic heart valve (Carpentier-Edwards Perimount Magna, Edwards Lifesciences, Irvine, CA) and faced a significant risk of reoperation. Elderly patients with ViMAC exhibited significant mitral valve calcification (MAC). Pre-operative ECG-gated CT imaging was performed on all patients to measure the mitral valve annulus diameter and determine the appropriate size of the intended Sapien 3 Ultra. In each case, the Sapien 3 Ultra was positioned with one-third of its height in the left atrial region and the remainder within the left ventricular outflow tract, as per the manufacturer's recommendations[136]. Post-TMVR CT imaging was conducted for five patients to assess the neo-LVOT region. For the remaining patients, a further CT scan during the brief follow-up interval was impractical due to renal impairment associated with senior age. The neo-LVOT area was determined utilizing the Mimics Enlight TMVR structural design tool (Materialise, BE) and pre-TMVR CT images. The local ethical committee approved the trial, and all patients provided informed consent before enrolment.

7.3.2 Patient-specific model

ECG-gated CT images during the end-systolic phase were segmented for all patients utilizing the medical imaging software Mimics (v21, Materialise, BE) [137]. Semiautomatic thresholding was utilized to reconstruct the left heart, encompassing both the atrium and ventricle, as well as the proximal aortic root. The left myocardial wall was segmented, and solid models of the left atrium and aorta were created, extruding the shell luminal surface mask by 4 mm and 2 mm of thickness, respectively. Segmentation was also created for the band ring and the bioprosthesis for the ViR and ViV cases respectively. In ViMAC, the pronounced calcification pattern adjacent to the mitral valve annulus was clearly delineated

from the left heart mask. Smoothing and refinement were implemented to enhance mesh quality while maintaining an accurate reconstruction.

For ViR and ViMAC, the mitral valve was represented utilizing a parametric model and anatomical measurements previously delineated by our team [96]. The length of the mitral valve leaflets was quantified via CT scan and subsequently utilized to model the free edges of the mitral valve in the Grasshopper toolbox of Rhinoceros (v.7.1, McNeel & Associates, WA, USA). Consequently, two surfaces were created to interpolate the margins of the mitral valve, modeling both the anterior and posterior mitral leaflets. Table VIII reports clinical and procedure information for each patient case.

Table VIII. Demographic data, device size and post-TMVR measurement of neo-LVOT.

Procedure	Age (yrs)	Annulus Size (mm)	Mitral Valve Length (mm)	Device Size (mm)	neo-LVOT (mm^2)
ViR-Case#1	70	20.4 - 25.3	15.7 - 12.7	26	348.4
ViR-Case#2	71	23.2 - 25.4	18.0 - 10.3	23	455.8
ViV-Case#1	84	29.1 - 31.2	/	29	318.1
ViV-Case#2	74	24.5 - 25.2	/	26	462.1*
ViV-Case#3	78	21.9 - 22.7	/	26	147.3
ViMAC-Case#1	71	12.7 - 24.9	8.7 – 10.9	23	154.4
ViMAC-Case#1	82	22.7 - 21.1	7.4 – 9.2	26	110.2*

Note: minimum and maximum size of annulus size are reported; mitral valve length comprises the posterior and anterior leaflets dimensions; *indicates measurements based on pre-TMVR CT images by Mimics software.

All anatomical components were subsequently meshed with tetrahedral elements of varying refinements with the ICEM meshing tool (v2021, Ansys Inc, PA, USA).. The left atrium and aorta were regarded as a quasi-incompressible Neo-Hookean material with parameters C10=0.17 MPa and D1=0.3 MPa-1. Linear elastic material properties were employed for calcification, consistent with prior research (E=10 MPa and n=0.475) [59, 103]. Both active and passive material characteristics were employed for the myocardial wall, similarly to [138, 139]. The active tension in the direction of cardiac fibers was produced using a time-varying elastance model, which was stimulated by a hypothetical temperature field during the simulation of the cardiac cycle. The passive left-ventricular response was replicated utilizing the Ogden and Holzapfel anisotropic hyperelastic constitutive law [140], which has been employed in numerous cardiac simulation investigations [141, 142]. The direction of myocardial fibers was defined using a local coordinate system, with a fiber angle of ±60 degrees from the epicardium (positive) to the endocardium (negative).

The anisotropic hyperelastic material model of Holzapfel–Gasser–Ogden was utilized for the mitral valve, employing material values derived from literature and a fiber orientation of 13 degrees [69]. Table IX summarizes the material descriptors for the involved anatomical parts and devices. Table X shows the material descriptors of mitral valve and left ventricle.

Table IX. Material parameters adopted for the device, left atrium, aorta and calcifications.

	E (MPa)	ν	C10 (MPa)	D1 (MPa^{-1})	σ_y (MPa)	σ_{ult} (MPa)	ε_p	η (Pa s)	D (kg/m^3)
Left Atrium		0.49	0.17	0.3					1060
Aorta			0.17	0.3					1060
Calcification	10	0.47							2000
Band Ring									8000
Bioprosthesis			1.7	0.65					1060
S3 Ultra Stent	233e+3	0.35			414	930	0.45		8000
Sealing Skirt	55	0.49			6.6	6.6	0.6		8000
Balloon	600	0.3							1060
Fluid								3.7e-3	1060

Note: E = Young modulus; ν = Poisson coefficient; C10 = material constant; D1=incompressibility factor σy = yield stress; σult = ultimate tensile stress; εp = plastic strain; η = viscosity; D = density.

Table X. Material parameters adopted for mitral valve (MV) and left ventricle (LV).

	C10 (MPa)	k_1 (MPa)	k_2 (MPa)	k	a (MPa)	b	a_f (MPa)	b_f	a_s (MPa)	b_s	a_{fs} (MPa)	b_{fs}	C_{a0} (mmol/L)
MV	1.2 e-4	1.1 e-3	8.4 e-3	8.0 e-2									
LV					4.0 e-1	12.0	5.0 e-1	5.0	2.0 e-1	2.0	1.1 e-2	2.0	2.66

Note: C10 = material constant of isotropic response; k1 and k2 = material constant of fiber response; k = fiber dispersion parameter; a and b = material constants of isotropic response; af and bf = material constants of stiffness in fiber direction; afs and bfs = material constants of stiffness in sheet direction.

7.3.3 Band ring, bioprosthesis and Sapien 3 Ultra models

For patients with ViR, the band geometry was reconstructed by sweeping the protrusion of a circular curve perpendicular to the band ring centerline, as calculated from ECG-gated CT images. The circular curve's cross-section measured 3 mm in diameter. The material descriptors established by Morganti et al. [143] were utilized to simulate the Nitinol material. Tetrahedral elements measuring 0.8 mm were employed to discretize the band ring geometries. Wire connections were established to connect the band ring to the left cardiac anatomies.

In patients undergoing ViV, the bioprosthesis stent wire was designed with a spline curve aligned with the bioprosthesis mask observed in CT imaging. The stent wire's cobalt-chromium alloy was simulated employing Von Mises plasticity and isotropic hardening based on literature data [144]. Besides the stent wire, the bioprosthesis was presumed to be composed of a polyester fabric, modeled using a Neo-Hookean model (C10=1.7 MPa and D1=0.65 MPa-1) [145]. The device was further meshed using tetrahedral elements, while the beam elements represented the stent wire connected to the bioprosthesis model.

The Sapien 3 Ultra and balloon delivery systems were employed to replicate the TMVR previously delineated by our team [51]. The metallic stent of the 26 mm Sapien 3 Ultra was composed of about 60,000 structured hexahedral solid parts with reduced integration (C3D8R). The 23 mm device were derived as scaled variants of the 26 mm type. The bioprosthesis stent frame, composed of cobalt-chromium alloy, was believed to exhibit Von Mises plasticity and isotropic hardening. The sealing skirt was created by enclosing the structural cell geometries with several surfaces designed at the mid-thickness of the device frame during the crimping phase. The surfaces were discretized with triangular shell elements, assuming a thickness of 0.1 mm, and subsequently linked to the device frame via tie contact conditions. Elasto-plastic material characteristics were utilized to model the polyethylene terephthalate (PET) of the sealing skirt [145]. Reverse engineering was employed to obtain the balloon profile with a laser scanner (Hexagon Manufacturing Intelligence, Cobham, Great Britain), followed by revolving the generative curve around the balloon axis in Rhinoceros (Robert McNeel & Associates, USA). Membrane elements (M3D4) with a thickness of 0.1 mm were employed for the balloon, which was presumed to be a linear-elastic material (E=600 MPa and v=0.3).

7.3.4 Simulation of TMVR procedures

The Sapien 3 Ultra deployment followed by one cardiac beat was simulated in Abaqus/Explicit FEA solver (v.2021, Dassault Systèmes, FR). The Sapien 3 Ultra was crimped utilizing a rigid dodecahedral surface and progressively advanced in the radial direction from the nominal device diameter to the final diameter (e.g., 4.5 mm for the 26 mm device). A simulation step of 0.1 seconds was incorporated to accommodate the elastic recoil resulting from the elasto-plastic characteristics of the device frame. A comparable method was employed to deflate the balloon delivery system by restricting the distal ends in all directions. Both frictionless and rigid normal contact conditions were employed to represent the interaction between the device and the balloon.

The fluid-cavity method was employed to accurately replicate the expansion of a volume-controlled device during deployment. The fluid material parameters were calibrated to guarantee the balloon's filling with the manufacturer's suggested nominal capacity (e.g., 21 mL for the 26 mm device). The distal extremities of the left atrium and aorta were constrained in all directions as boundary conditions. The deployment was executed with the mitral valve in the open position and under steady-state conditions. Tie contacts were established between the anatomical components, while the general contact algorithm in Abaqus/Explicit was employed to address the interactions among the anatomical parts. Following the deployment phase (0.5 s), an extra step was incorporated to accommodate the elastic recoil of the device resulting from the hyperelastic properties of the soft tissue components. Mass scaling was employed to decrease computing expenses while preserving the ratio of kinetic energy to internal energy within limits of less than 10%. A Rayleigh damping factor was employed to regulate the dynamic response of the anatomical models and device delivery systems.

After performing a cardiac beat with the implanted device within the mitral landing zone, deformed geometries of the left heart and deployed devices were exported at the end-systolic phase to create the fluid domain. The elements were subsequently meshed into tetrahedral configurations with a dimension of 0.6 mm. Laminar flow conditions and non-Newtonian viscosity, as delineated by the Carreau model, were presumed [146]. Computational flow analyses were conducted utilizing an implicit algorithm in FLUENT (v21, ANSYS Inc., Canonsburg, PA, USA), employing SIMPLE for pressure correction and the second-order accurate upwind scheme. A flow velocity profile was established at the left atrium, whereas a pressure outlet profile was applied at the aortic root [16]. Three cardiac cycles were simulated to mitigate the impact of transient flow on the resultant hemodynamic, with the final cycle designated for flow investigation.

7.3.5 3D Printing

The superior segment of the left ventricle in each patient was fabricated using 3D printing to measure the neo-LVOT area. The left atrium and aorta were excluded to provide an open geometry, enabling the direct visualization of the implantation. In the ViR and ViMAC cases, the band ring and bioprosthesis were incorporated into the left heart architecture of each patient. Stereolithography (SLA) rapid prototyping technique (Form 3B+, Formlabs, MA, USA) was employed to fabricate the phantoms by means of a stiff grey resin. Layer thickness was set at 0.05 mm to maintain the curvature variations on the heart model. A cylindrical surface with the same dimensions of Sapien 3 Ultra was fabricated using an elastic resin and

subsequently positioned manually within the rigid 3D printed anatomical components. A CT scan was then performed on the 3D printed model to assess the neo-LVOT area.

7.3.6 Results and findings

Figure 7.2 shows the end-systolic actual configurations of the left heart with implanted devices for three representative individuals with ViR, ViV, and ViMA C and corresponding neo-LVOT, computed according to the methodology suggested by Blanke et al. [8].

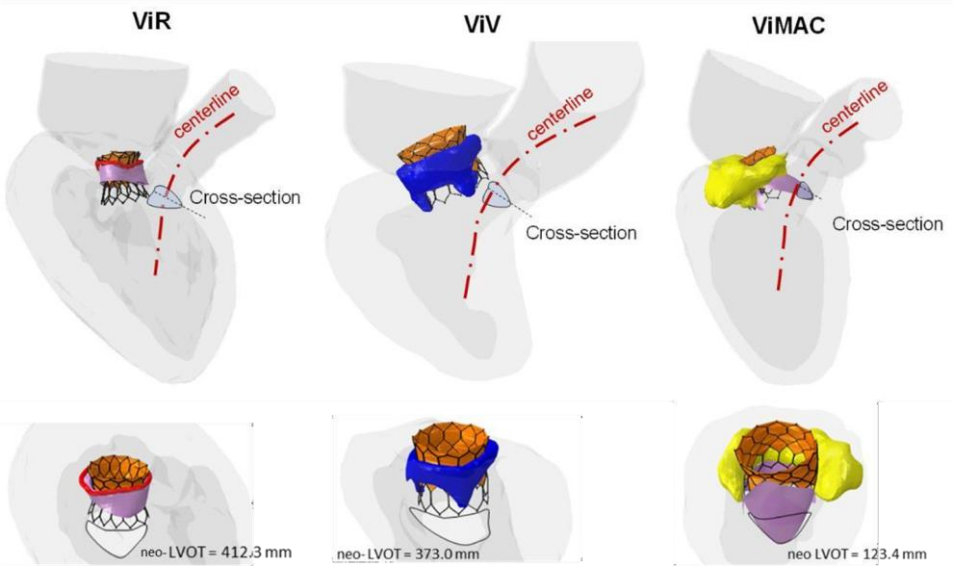

Figure 7.2. Sagittal view of LVOT obstruction and its neo-LVOT area for three TMVR patients with ViR, ViV and ViMAC.

After establishing the centerline of the aortic root and natural LVOT, the anatomical geometry was sectioned using a cross-sectional plane perpendicular to the centerline, positioned around the minimal neo-LVOT region observed between the device frame and the myocardial wall. ViR patients exhibited the highest neo-LVOT area values (453.4±58.1 mm^2) in contrast to those with significant MAC (155.6±46.1 mm^2) and with ViV (246.6±109.5 mm^2). During an entire cardiac beat, it was found that the neo-LVOT was smaller in concomitance with end-systole, whereas end-diastole exhibited an approximate 48% rise in the neo-LVOT area magnitude (Figure 7.3).

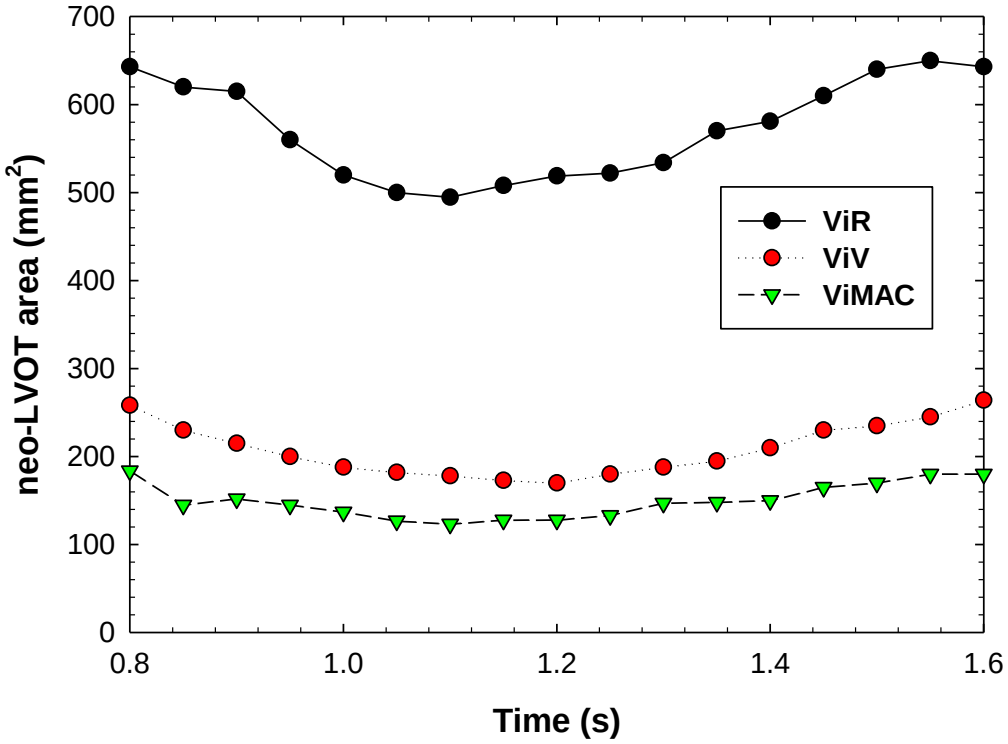

Figure 7.3. Neo-LVOT area fluctuations over an entire cardiac beat for three representative cases of ViMAC, ViR and ViV.

From the flow analysis, the pressure gradient was computed across the LVOT. From the obtained pressure distribution (Figure 7.4), it is shown this narrowed region experiences significant pressure drops, which may vary across the analysed cohort.

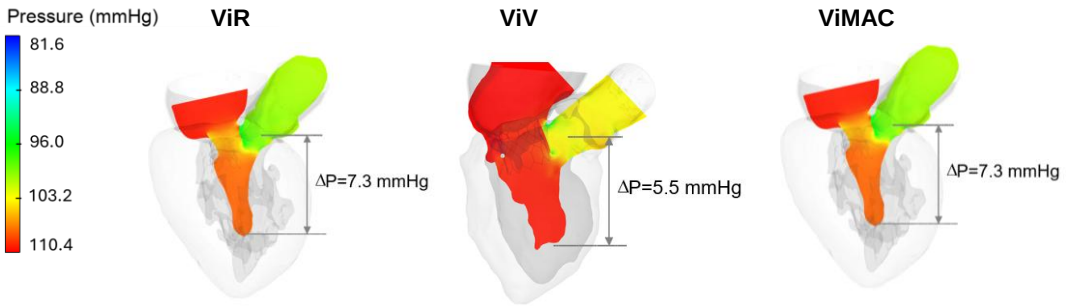

Figure 7.4. Blood pressure map at end-systolic phase with computed pressure drops across the LVOT for three representative cases.

The 3d printed replica and its CT scan are presented in Figure 7.5.

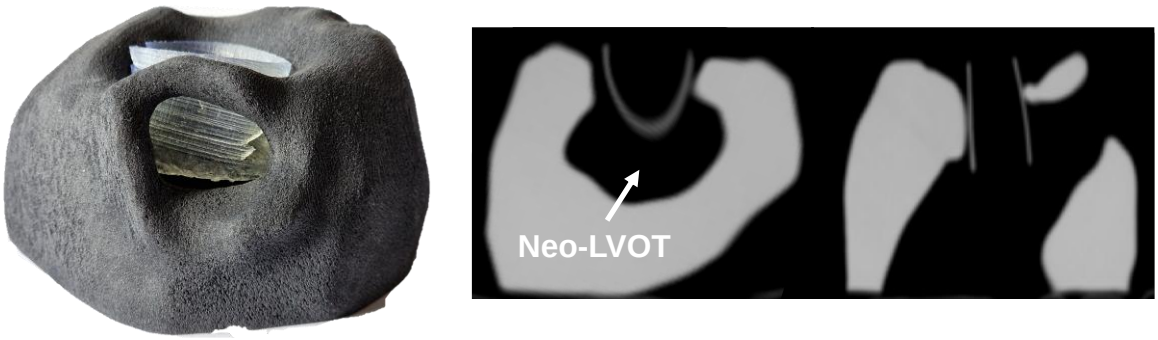

Figure 7.5. 3D printed models and related CT imaging of the left heart for the patient with ViR.

Correlation coefficient was R=0.992 between post-TMVR CT and computational measurements (95% confidence interval, CI = 0.990-0.996, P<0.001) and R=0.965 between post-TMVR CT and 3D printed models (95% confidence interval, CI=0.982-0.988, P<0.001). The Neo-LVOT assessed via post-TMVR CT imaging exhibited a bias of ±37.1 units relative to computational predictions (limits of agreement = 2.9 - 71.3) and a bias of ±30.0 units in comparison to 3D printed replicas (limits of agreement = -55.0 – 115.2).

7.4 Case study 2: Valve-in-Ring TMVR procedure with LHHM

The dynamic implications of ViR TMVR procedure were investigated by conducting computational flow analysis of the procedure using the Living Heart Human Model (LHHM). Specifically, a parametric analysis was performed to evaluate the procedure performance in presence of stiff band ring, balloon overexpansion and high implantation depth. Results from this research has been published in [138].

7.4.1 LHHM Adaptation

The Living Human Heart Model (LHHM) is a high-fidelity, multiphysics model of the heart developed by Dassault Systèmes. It captures the electrical, structural, and fluid dynamics of heart function and can be adapted to simulate patient-specific scenarios [147]. In this study, the mitral valve regurgitation was simulated by altering the left ventricular material characteristics in the myocardial wall region, referred to ischemic region next to the posterior papillary muscle (Figure 7.6). Active contraction was suppressed in the region adjacent to the papillary muscle during the cardiac cycle to replicate a heart failure scenario.

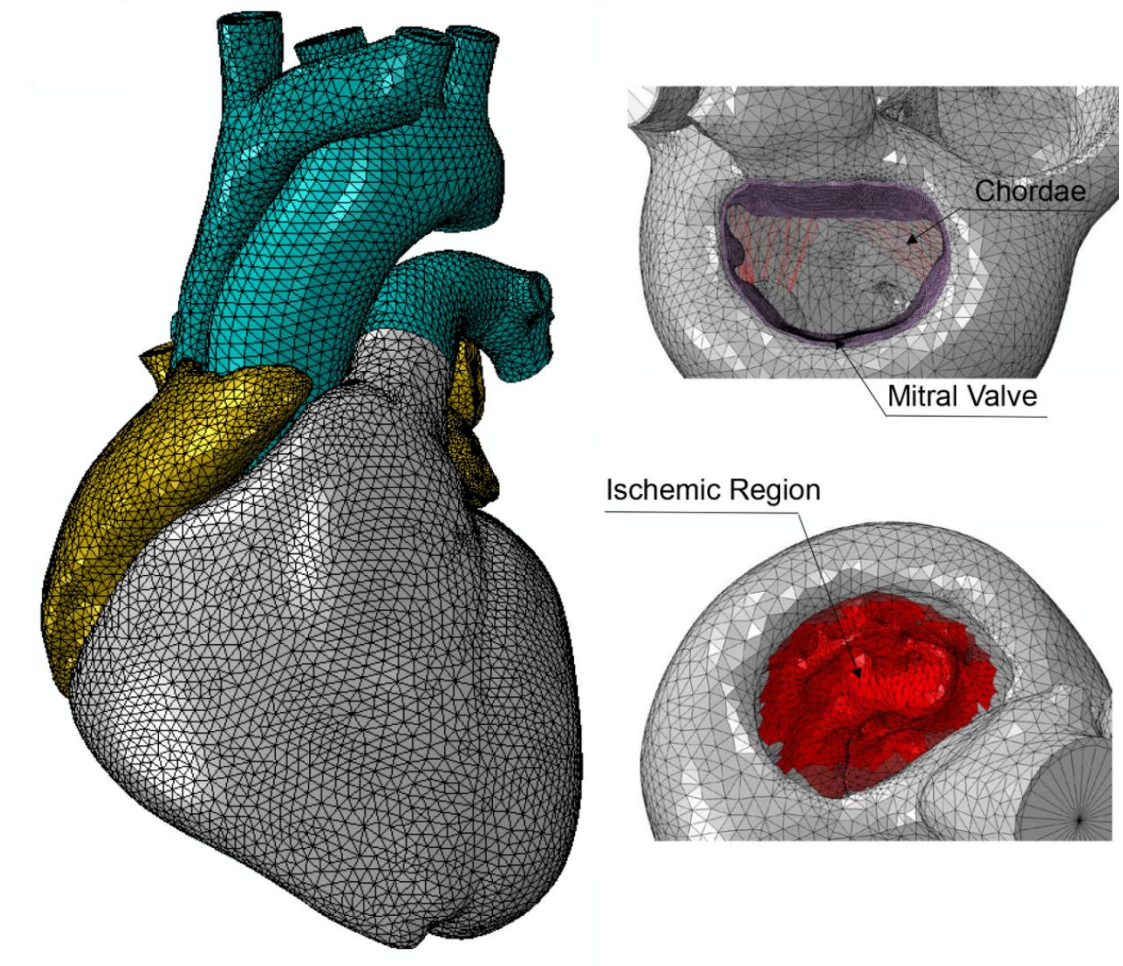

Figure 7.6. LHHM system and views of the mitral valve, chordae and ischemic region.

The passive behaviour of heart chambers is modelled with the anisotropic hyperelastic constitutive model proposed by Ogden and Holzapfel [140]. The dysfunctional area was modelled by increasing the isotropic response by 30%, as previously executed [148]. Similarly, the end-systolic dysfunction was modelled by reducing the parameter representing the peak intracellular calcium concentration (Ca0) of 20 %. The mitral valve was modelled with the following strain energy function:

$$\psi_{dev} = \frac{a}{2b} exp[\mathrm{b}(I_1 - 3)] + \sum_{i=f,s} \frac{a_i}{2b_i} \{exp[b_i((I_{4i} - 1)^2)] - 1\} + \frac{a_{fs}}{2b_{fs}} \left[exp\left(b_{fs} I_{8fs}^2 - 1\right)\right]$$

Eq. 9

Expressed in terms of the strain invariants I1, I4f, I4s, and I8fs and eight material parameters a, b, af, bf, as, bs, afs, bfs. The material descriptors were determined by MayNewman and Yin from biaxial mechanical testing of the porcine aorta [149]. Chordae tendineae were characterized by hyperelastic behavior described by a Marlow form of strain energy potential fitted on uniaxial test results from Kunzelmann and Cochran [150].

The material parameters adopted are summarized in Table XI.

Table XI. Material parameters for mitral valve (MV), left ventricle (LV) and ischemic region.

	a (MPa)	**b**	**a_f (MPa)**	**b_f**	**a_s (MPa)**	**b_s**	**a_{fs} (MPa)**	**b_{fs}**	**C_{a0} (mmol/L)**
MV	8.7e-4	2.7	5.0e-4	12.0	3.8e-3	7.6e-1	3.8e-3	7.6e-1	
LV	4.0e-1	12.0	5.0e-1	5.0	2.0e-1	2.0	1.1e-2	2.0	2.66
Ischemic region	5.2e-1	12.0	5.0e-1	5.0	2.0e-1	2.0	1.1e-2	2.0	2.12

7.4.2 Band ring and Sapien 3 Ultra models

The band ring was modelled as described previously, with a circular cross-section of 3 mm and Nitinol material parameters [143]. The shape was scaled to suit the MV of the LHHM and was meshed with tetrahedral elements.

The 23 mm Sapien S3 Ultra was also integrated in the system and aligned into the mitral annulus according to the guidelines [136]. The design was realized through an inverse engineering approach by acquiring the morphological features with micro-CT scanning. The part was then discretized with 60,000 structured hexahedral solid pieces featuring reduced integration and hourglass control. The sealing skirt was developed after the device crimping in order to avoid element distortion. The S3 stent frame and skirt material were modeled with elasto-plastic behaviour. THV leaflets exihibited a linear elastic biomechanical response (ρ = 1060 kg/m3, E = 8 MPa, and ν = 0.45) [98]. The balloon was modeled using membrane elements (M3D4) with a thickness of 0.1 mm and linear-elastic material parameters (ρ = 1060 kg/m^3, E = 600 MPa, and ν = 0.3) [55].

7.4.3 Simulation of TMVR procedure

The cardiac cycle simulation was performed in Abaqus/Explicit. Frictionless contact conditions were defined between the band ring the MV annulus, while sutures were simulated by means of wire connections between the periphery of the ring and the MV annulus in a radial direction.

S3 crimping and ballon folding were accomplished with a surface that progressively reduce its diameter with frictionless contacts as previously reported (see 7.3.4). Implantation was realized according to the manufacturer's guidelines, with one-third of the device in the left atrium. The fluid cavity approach was implemented to correlate inflation with the specified volume of 17 ml. A parametric analysis was conducted in order to determine the effect of several factors with respect to the baseline model. In particular, the effect of high implantation depth was considered by creating an analogous model with the device

translated into the atrium of additional 5 mm. Additionally, a third model accounted for a bad ring l with stiffer material properties to replicate the procedure with different mechanical behaviour of the ring. Finally, as balloon overexpansion may occur to enhance the device's adhesion to the band ring, a further simulation was conducted, increasing the fluid volume by 1 ml relative to the reference value.

The deformed geometries at end-systole phase resulting from the TMVR simulation, i.e., the heart and deployed device, were the starting point of CFD analysis. The heart was discretized with 3,715,183 tetrahedral elements with ICEM CFD (v21.0, ANSYS Inc., Canonsburg, PA). The blood was assumed as a laminar-flow fluid with non-Newtonian viscosity represented by the Carreau model and density of 1060 kg/m3 [96]. CFD was performed using an implicit scheme in FLUENT (v21, ANSYS Inc., Canonsburg, PA, USA). Flow velocity profiles were imposed at each inlet, i.e., pulmonary vein, maintaining the proportionality to the cross-sectional area at the level of the bifurcations. Pressure was imposed to the outlet of the aortic root. Three cardiac cycles were simulated to mitigate instabilities associated with transient flow, with the final cycle utilized for flow analysis to get a steady state solution.

7.4.4 Results

After deployment, the TMVR biomechanical performance was evaluated in terms of contact pressure and device-anchoring contact area during an entire cardiac cycle for band ring and mitral valve (Figure 7.7).

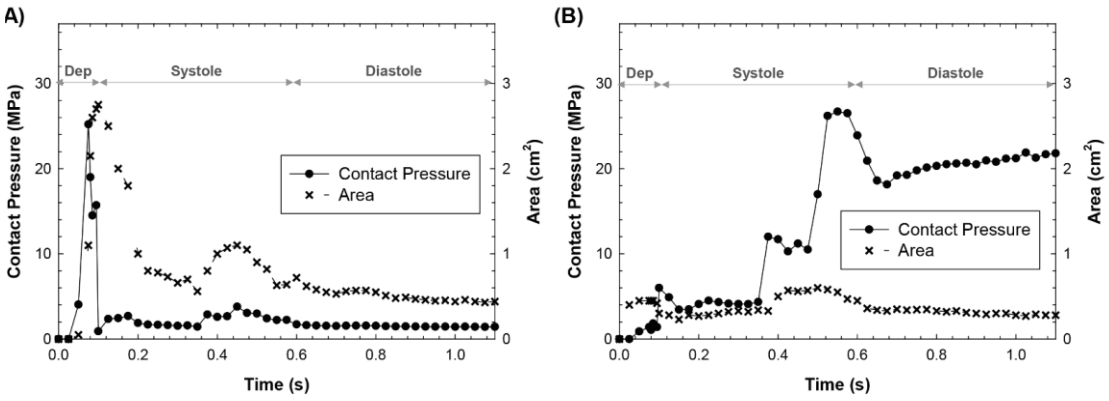

Figure 7.7. Contact pressure and area over an entire cardiac beat exerted on A) bad ring and B) MV.

During the S3 deployment, both the contact pressure and area of the band ring experienced a significant increase, followed by a decline during heart contraction. During passive left ventricular filling, contact pressure for the mitral valve was elevated.

The neo-LVOT area was computed according to the methodology proposed by Blanke and collaborators [125]. Specifically, the geometric centerline of the aortic root and native left

ventricular outflow tract anatomy was delineated and consequently the cross-sectional area perpendicular to the centerline and at the level of the smallest LVOT tract was established ad neo-LVOT area. Thought all the models achieved average neo-LVOT areas within acceptable values (367.7 mm2 for the reference model), dynamic effects significantly changed their value over the cardiac cycle, with an approximate 40% decrease at maximal systolic myocardial contraction compared to the end-diastole. The smallest neo-LVOT was found in the case of the balloon overexpansion while the most significant decrease iver the cardiac cycle was obtained by the model with high implantation depth.

Figure 7.8 showed the results of the CFD analysis computed for the reference case. The narrow region of the LVOT presented significant values of flow velocities. Nested helical flow was detected adjacent to the S3 skirt and the anterior mitral valve leaflet. A pressure differential of 4.5 mmHg was calculated between the left ventricle and the neo-LVOT area.

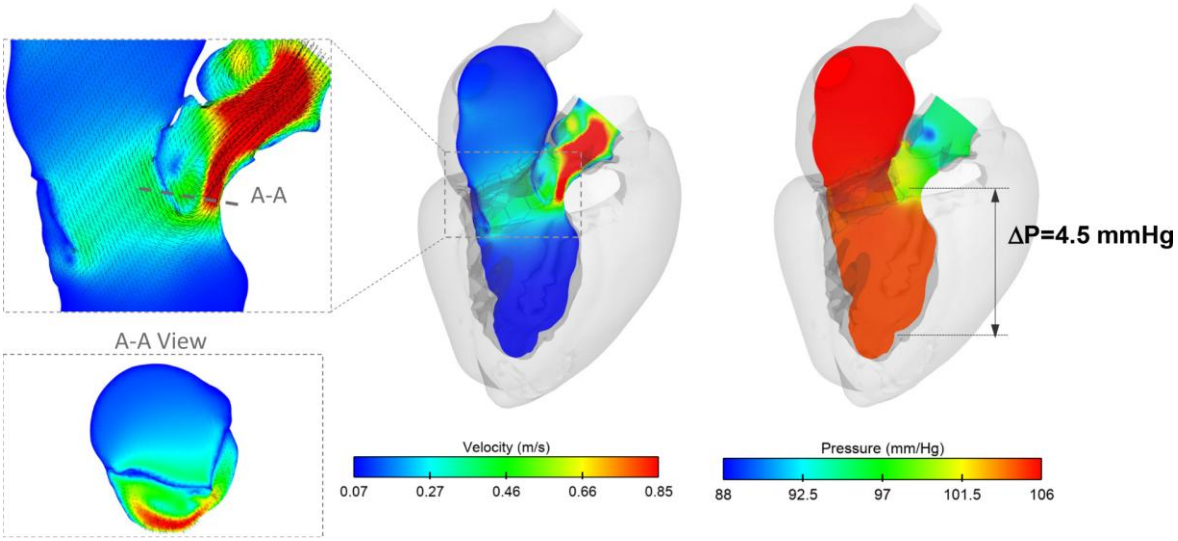

Figure 7.8. Blood flow velocity and pressure distribution at end-systole showing subaortic flow stenosis in the neo-LVOT with the drop computed across neo-LVOT area.

7.5 Discussion

The 2 case studies here presented greatly contributed to advancing the knowledge of TMVR procedures and related life-threatening risk of LVOT obstruction. By providing valuable insights on neo-LVOT biomechanics and hemodynamic, the developed in-silico and in-vitro models can effectively enhance the prediction of adverse events in a wide range of patients, including complex cases as ViR, ViV, ViMAC. The precise pre-procedural evaluation of

patient eligibility for TMVR is crucial in reducing the incidence of clinically significant LVOT obstruction and, consequently, adverse events.

The first study highlighted the potential of integrating in-silico models and 3d prototyping for predicting morphological and hemodynamic consequences after TMVR on the neo-LVOT. Patient-specific models representing the entire spectrum of patients requiring TMVR were developed. Specifically, the virtual implantation of the THV and subsequent cardiac beat was simulated in ViV, ViR, ViMAC, followed by the creation of 3d printed replicas of each patient model. Assessing the procedure for each patient category is pivotal as the differences in anatomical and physiological characteristics across patient groups can lead to a wide range of procedural outcomes in TMVR. By anticipating the risk for each procedural scenarios, clinicians can better predict the risk of LVOT obstruction and accordingly tailor the operating strategy. As noted by Ooms et al. [151] in-silico and 3D printed models enhance the ability to assess the device's effect on life-sized anatomical models.

In this study, the finding of elevated neo-LVOT area values in patients with ViRs compared to those with ViV and ViMAC aligned with clinical outcomes [12]. Imaging measurements highlighted that patients with ViR have significantly higher values of neo-LVOT areas compared to patients with ViMAC [11, 12]. The pressure drop also significantly differs among various types of TMVR procedures. The patient with ViR and a neo-LVOT area of 412.3 mm^2 saw a pressure drop of 7.3 mmHg, surpassing the patient with ViMAC, who had an obstruction of 188.2 mm^2 and a pressure drop of 5.6 mmHg, indicating that multiple factors may contribute to the hemodynamic disturbances caused by the implanted device. It has been shown that the annulus-to-septal distance, the dimensions and mass of the left ventricle at end diastole, and myocardial thickness are predisposing variables for a heightened risk of LVOT obstruction [11].

By confirming the influence of these variables in larger patient cohort, there will be unequivocal proof that individualized approaches for assessing anatomic suitability for TMVR are essential to quantify the multifactorial risk of LVOT obstruction.

The second study employed a sophisticated and highly accurate heart model, i.e., LHHM, to virtually implant the THV in a ViR case and consequently assess the biomechanics and hemodynamics implications of neo-LVOT obstruction. Although patient-specific anatomies were not used, the advanced computational modeling offered by the LHHM provided significant insights into the dynamic behavior of the neo-LVOT area throughout the cardiac cycle. Results indicated that the neo-LVOT area can reduce up to 50% during peak systole

compared to diastole, leading to the presumption that the risk stratification of patients undergoing TMVR should not just rely on pre-TMVR imaging criteria at end-systole.

The employment of LHHM allowed to evaluate for a single idealistic patient case, i.e., ViR, several factors that may contribute to the occurrence of hemodynamic impairments linked to LVOT obstruction. It was shown that rigid rings and high implantation depth were associated with smaller neo-LVOT areas and increased contact pressures, thus increasing the risk of adverse events. Although element convergence was not executed, the LHHM yielded a steady-state solution with stable stress levels following three cardiac cycles using the specified mesh volume. Validation was performed for the constitutive model for passive and active contraction, along with the electrical model, using experimental data. Recent validation investigations using LHHM have demonstrated strong concordance with clinical data about left and right ventricular ejection, maximum and minimum blood pressure across the four heart chambers, and maximum left ventricular apex-base shortening [147]. In this study, the predicted neo-LVOT values aligned well with those reported by Yoon et al. [130], with estimations ranged between 220 mm^2 and 430 mm^2 in a large cohort of ViR patients. In line with previous findings from both clinical studies and basic science [130, 152, 153], the neo-LVOT area can be evaluated by means of baseline CT datasets and sophisticated computer simulations combined with 3D printing methodologies. A careful CT-based patient analysis is the standard approach for risk stratification after TMVR. Blanke and collaborators [125] established a workflow to virtually implant the device model in the mitral valve and measure the smallest neo-LVOT area on the CT image. Though a universal cutoff value for all transcatheter heart valves does not exists, a neo-LVOT area between 1.7 and 1.9 cm^2 is considered safe for the deployment of the Sapien 3 device in cases of failing mitral valves [129]. The threshold for adverse outcomes associated with LVOT obstruction was determined to be an area $\leq$170.0 mm^2 [12].

However, the CT-based methodology alone is insufficient to account for the dynamic variations of the estimated neo-LVOT throughout the cardiac cycle. 3d printed models enable visual assessment of device protrusion into the left heart, overcoming the limit of 2D imaging and permitting the examination of various depths and angles of device deployment. Additionally, in-silico models may provide important insight on the hemodynamic implication of neo-LVOT variations over the cardiac cycle, overcoming the issue related to the static imaging measurements. In the case study of ViR with LHHM resulted a significant alteration in the neo-LVOT area, varying from a peak of 472.1 mm^2 during early systole to

a trough of 183.0 mm² at end-systole, with the minimum neo-LVOT area being close to the threshold of 170 mm².

Significant results from the in-silico analysis demonstrated the capability of CFD in estimating the stenotic flow caused by the protruding device within the left ventricular chamber [131, 154, 155]. An increase in left ventricular afterloads and the occurrence of systolic flow disruptions in proximity to the neo-LVOT region within models exhibiting optimal LVOT obstruction geometries has been shown [135]. Hill and collaborators [156] have demonstrated in three patients with ViMAC the correlation between neo-LVOT area and pressure gradient raise across the obstruction. Their findings underscored the risk of thrombus formation adjacent to the device implanted in the calcified mitral valve leaflets, as the interplay of high shear stress levels and prolonged exposure to shearing may induce platelet activation, potentially resulting in premature device failure. A FSI analysis focused on the hemodynamic environment after THV deployment [134]. However, the simulation encompassed the deployment phase, neglecting the importance of the beating heart.

The computational flow analyses here presented were computed after a cardiac beat and revealed a sub-stenotic aortic stenotic flow and a pressure drop at the neo-LVOT region. This knowledge can certainly improve procedural planning to achieve superior clinical outcomes and guide the design of the next generation of transcatheter heart valves. Current THVs are primarily designed for aortic valve replacement and may not be optimal for the unique challenges presented by the mitral valve. Future research should focus on the design and testing of mitral-specific THVs that can better accommodate the anatomical and functional complexities of the mitral valve, thereby reducing the risk of complications and improving patient outcomes.

7.6 Limitations

Though the first case study provided the patient-specific TMVR simulations over the entire spectrum of patient categories, the findings require validation in a larger patient cohort. A multicentre clinical trial is recommended to increase the sample size to consequently increase the understanding on the specific patient populations for ViR, ViV, and ViMAC. Additionally, post-TMVR CT imaging was impracticable for two of our patients; thus, the neo-LVOT regions were calculated utilizing the pre-TMVR CT and a virtual device model. This may have affected the comparisons of neo-LVOT areas across various techniques. The biomechanical response of the left heart during cardiac contraction was not validated against clinical data from a computational perspective. Finally, 3D printed models were constructed

from a hard material that did not account for cardiac compliance or the deformation that occurs during manual implantation of the device.

Despite employing the most sophisticated cardiac instrument for an in-depth analysis of neo-LVOT biomechanics, the second case study exhibits several limitations due to the intricacies of TMVR. The anatomic geometry and function of the LHHM are presumably distinct from those of the patient undergoing TMVR. The mitral valve leaflets of LHHM are comparatively short, despite being classified within the normal physiological range. A frictionless contact state was presumed between the device and the human host, but literature indicates a friction coefficient ranging from 0.1 to 0.2. The current computer simulation lacks a validation and verification assessment to evaluate the correctness of the model predictions, but this is impractical as the LHHM relies on optimal adult geometry.

Chapter 7

Particle Image Velocimetry Analysis in valve-in-MHV

Given the technological advancement and their level of accuracy, numerical models are becoming essential in predicting hemodynamic behavior and device-host interactions in TAVI. However, experimental validation remains a critical step for ensuring accuracy and reliability of these simulations. One of the most advanced and adopted experimental methodologies is Particle Image Velocimetry (PIV), a non-invasive flow visualization technique. However, this methodology is costly and requires strict safety measures due to the use of lasers. The present chapter aims to describe a conducted study employing backlight PIV, a cost-reduced and effective technique, to evaluate the hemodynamic performance of TAVI.

8.1 Introduction

Assessing TAVI and SAVR hemodynamic performances is essential for improving procedural outcomes. Notwithstanding huge advancements in valve designs since their first implantations, concerns still persist for both procedure regarding valve failure and related processes [157]. Bioprosthetic valves are preferred for their physiological flow characteristics but are constrained by a shorter lifespan, often necessitating reoperation due to structural valve degeneration [158, 159]. On the other hand, mechanical devices, especially bileaflet mechanical heart valves (MHVs), provide long-term durability, which makes them suitable for younger patients. However, they see a prevalence of thromboembolic events, requiring lifelong anticoagulation therapy and carrying a heightened risk of bleeding [23, 160].

The importance of hemodynamic assessment following aortic valve replacement procedures has been widely demonstrated [161-164]. Yoganathan et al. [159] delineated a span of turbulent stresses considered relevant to blood platelet activation and thrombus formation in heart valves. Additionally, washout phenomena have been linked to thrombus formation, prompting numerous studies to quantify these effects [163, 165].

The central hypothesis of this study is that implanting a THV into a mechanical valve with removed leaflets could reduce the need for anticoagulation therapy while simultaneously enhancing hemodynamic in the aortic root. To explore this, in-vitro experiments utilizing backlight PIV were conducted in a cardiac flowloop to quantify the flow performance and

thrombogenic potential of the Medtronic CoreValve THV when implanted in the annulus of a St. Jude MHV with its mechanical leaflets removed. The hemodynamic performance of this procedure, referred to as valve-in-MHV, was compared to that of a single MHV and THV to elucidate the hemodynamic factors that may influence clinical outcomes when implementing the proposed configuration in cardiac surgery.

8.2 Pulse duplicator system

In this study, a cardiac flowloop was employed to simulate physiological flow conditions of the left heart [166]. Three valve configurations were investigated: i) 21-mm St. Jude Medical™ bileaflet mechanical valve (SJM MHV), ii) 26-mm Medtronic CoreValve (CoreValve THV), and iii) valve-in-MHV configuration with the CoreValve THV implanted in the SJM MHV. Specifically, the latter configuration was configured by constraining the THV with a 3d printed replica of the SJM MHV annulus to avoid the breaking and removal of the real leaflets. These configurations were evaluated under two different hemodynamic conditions: (i) 72 bpm with an aortic pressure of 120/80 mmHg and cardiac output of 5.0 L/min, and (ii) 72 bpm with an aortic pressure of 100/60 mmHg and cardiac output of 3.0 L/min.

The main function of the employed flowloop was to reproduce physiological boundary conditions so that the tested valves could experience pressure and flow rates similar to those provided by the cardiac pulse. This pulse duplicator, schematized in Figure 8.2, is composed of many components. The piston pump (ViVitro Inc., Victoria, BC, Canada) enables the compression of a silicone membrane in the left ventricle chamber, acting as a contracting ventricle and driving the flow towards the test bench where the aortic valve was located. The flow then passes through the Windkessel chamber, i.e., compliance chamber, which emulate the elastance of the aorta, and is recirculated via a resistance element simulating systemic resistance, to the fluid reservoir, i.e., left atrium chamber. The hydraulic loop is closed by the presence of a bileafleat valve, i.e., the mitral valve, connecting the left atrium and left ventricle chambers. By regulating these components, i.e., the orifice of the resistance, the air trapped in the compliance chamber, the fluid level in the reservoir, and the piston pump's amplitude, physiological hemodynamic conditions can be achieved. Additionally, this system comprised a high-speed camera and a LED light enabling the backlight PIV measurements.

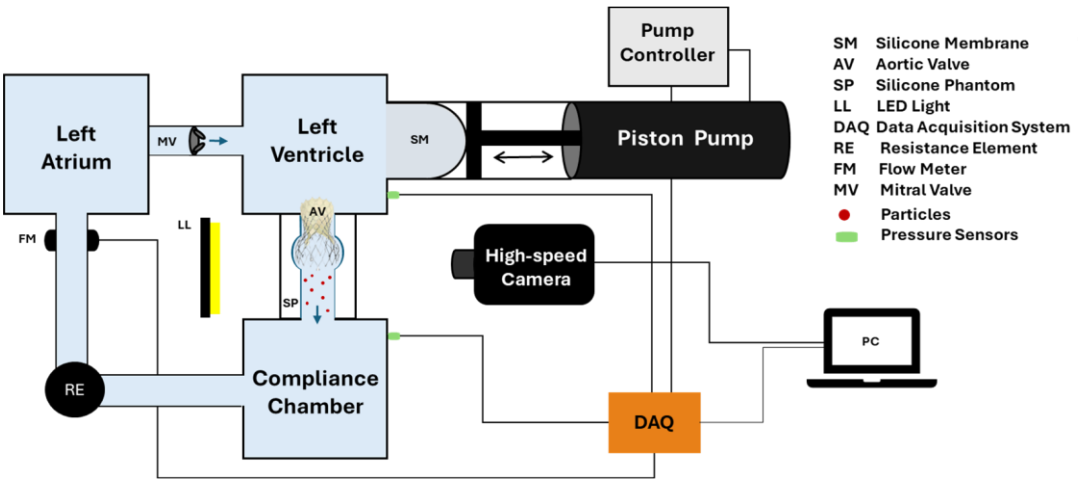

Figure 8.1. Schematic view of the pulse duplicator and backlight PIV systems.

The piston pump position, from which stroke volume was derived, was recorded by a linear variable differential transformer (LVDT) sensor. Two pressure transducers (PX600F 150B, Edwards Lifesciences, CA, USA) were positioned to measure left ventricular and aortic pressures. Additionally, two ultrasonic flow probes (TS410/ME-11PXL, Transonic Systems, Inc., Ithaca, NY) were positioned upstream of the mitral valve and downstream of the Windkessel chamber to measure mitral valve flow and cardiac output. All signals were synchronized using a trigger signal from the pump. All measurements were captured at a frequency of 1000 Hz using a NI 6221 data acquisition (DAQ) device (National Instruments), employing an in-house developed Matlab script.

The aortic test cell consisted in an optimally clear thick-walled silicone model to replicate the aortic root. It was fabricated by casting a clear silicone (Sylgard 184, The Dow Chemical Company, Midland, MI, USA) with a refractive index (RI) of 1.410 nD. The mold required for casting the silicone, along with the casting setup, was designed using Rhinoceros CAD software (McNeel & Associates, USA) and 3D printed using a stiff resin material.

A mix of water, glycerol, and sodium chloride (49.4%, 34%, and 16.6%, respectively) was used as the blood-mimicking fluid (BMF), resulting in rheological properties similar to those of blood (at 22°C: density $\rho = 1200$ kg/m³, dynamic viscosity $\mu = 5.6$ mPa s) while matching the refractive index of the silicone model to reduce image distortion [167].

The systolic performance was evaluated in terms of transvalvular pressure gradient (PG), defined as the positive pressure difference between the ventricular and aortic pressure curves during forward flow, and effective orifice area (EOA), calculated using Gorlin's equation [38]. The diastolic performance was associated with the regurgitant fraction (RF), calculated as the ratio of leakage volume (LV) to the total forward stroke volume (SV) [168].

8.3 Backlight PIV

Backlight PIV analysis was performed to measure flow velocities and turbulence dissipation across the valve. This method tracks the movement of particles in the flow by detecting their shadows in a series of high-speed image sequences to compute velocity vectors, enabling the reconstruction of flow fields within the experimental setup.

The working fluid was accordingly seeded with fluorescent red microspheres (density ρ = 1200 kg/m³), composed of polyethylene (PE) with diameters ranging from 355 to 425 µm. To overcome the hydrophobic nature of the seeded fluid, the microspheres were combined with Tween 80 Biocompatible Surfactant (Cospheric LLC) to disperse the particles within the aqueous solution.

The images were recorded using a Photron FASTCAM Mini AX 100 camera equipped with a Samyang fixed-focus lens (100 mm focal length, f/2.8 aperture). The analysis was performed using PIVlab (Matlab v2021, MathWorks, USA) [169]. Time-resolved PIV images were captured using an external trigger provided by the pump controller. Velocity vectors were computed from the spatial time-series cross-correlation of images within an interrogation window of 128 x 128 pixels with a 50% overlap, followed by additional passes with smaller window sizes (64 x 64 and 32 x 32 pixels) to enhance the correlation signal. A pixel pitch of 67.95 µm/pixel was achieved for the measurement field.

From the obtained velocity field, vorticity measurement is derived, to stress rotational aspects within blood flow shear, highlighting areas of high vorticity perpendicular to the plane axis, indicating both fluid particle shear and rotation. The vorticity is determined by the following equation:

$$\omega_z = -\left(\frac{dv_x}{dy} - \frac{dv_y}{dx}\right) (s^{-1}) \qquad \text{Eq. 11}$$

Where v_x and v_y represent the axial and lateral components of the computed velocity vectors, respectively, measured in meters per second (m/s).

Turbulent kinetic energy (TKE) and Reynolds shear stress (RSS), extensively associated with turbulence and platelet activation [170, 171], were also computed and are defined as follows:

$$TKE = \frac{1}{2}\left(\overline{v_x{'^2}} + 2\overline{v_y{'^2}}\right) \quad \text{Eq. 12}$$

$$RSS = \rho\sqrt{\left(\frac{\overline{v_x{'^2}} - \overline{v_y{'^2}}}{2}\right)^2 + \left(\overline{v_x{'}v_y{'}}\right)^2} \quad \text{Eq. 13}$$

Where vx' and vy' are the instantaneous velocity fluctuations in the x and y direction respectively and ρ is the blood density [172].

Statistical analysis was conducted using SigmaPlot 14.0, with data presented as mean ± standard deviation. A one-way ANOVA test followed by Tukey's pairwise comparison was used to compare hemodynamic parameters across groups. All analyses were performed using averages from 60 cardiac cycles.

8.4 Results

Table XII shows the baseline hemodynamic parameters obtained from flow and pressure data across the different valve configurations and protocol. A statistically significant difference in the hemodynamic parameters was seen among all groups ($P < 0.001$). Notably, the valve-in-MHV configuration displayed markedly higher mean and peak PG compared to both the Corevalve THV and the SJM MHV, consequently leading to a reduced EOA.

Table XII. Main hemodynamic parameters for the different valve configurations under various test conditions.

		Peak TVPG [mmHg]	**Mean TVPG [mmHg]**	**EOA [cm^2]**	**RF [-]**
SJM MHV	3	7.89 ± 1.12	4.33 ± 1.6	1.56 ± 0.43	0.15 ± 0.18
	5	15.20 ± 1.01	10.25 ± 0.38	1.6 ± 0.07	0.09 ± 0.3
CoreValve THV	3	9.48 ± 0.35	8.13 ± 0.65	2.13 ± 1.5	0.12±0.1
	5	12.49 ± 0.11	8.40 ± 1.03	2.1± 0.05	0.17 ± 0.2
Valve-in-MHV	3	17.36±1.08	9.21±0.87	1.53±0.87	0.14±1.02
	5	19.50 ± 2.24	13.41±1.84	1.4 ±0.32	0.31 ±0.87

Note: CO, cardiac output; TVPG, transvalvular pressure gradient; EOA, effective orifice area; RF, regurgitant fraction.

The velocity distributions were phase-averaged across the acceleration, peak systole and early-diastole phase (Figure 8.3). For the CO of 5 L/min condition, a central jet originating from the valve was observed at systole and values reached 1.81 m/s, 2.1 m/s and 2.66 m/s, for SJM BHV, CoreValve and valve-in-MHV configurations respectively. Similarly, at 3 L/min, peak velocities were 1.09 m/s for the SJM MHV, 1.35 m/s for the CoreValve THV,

and 1.74 m/s for the valve-in-MHV. During diastole at 5 L/min, velocities converged near zero across all configurations.

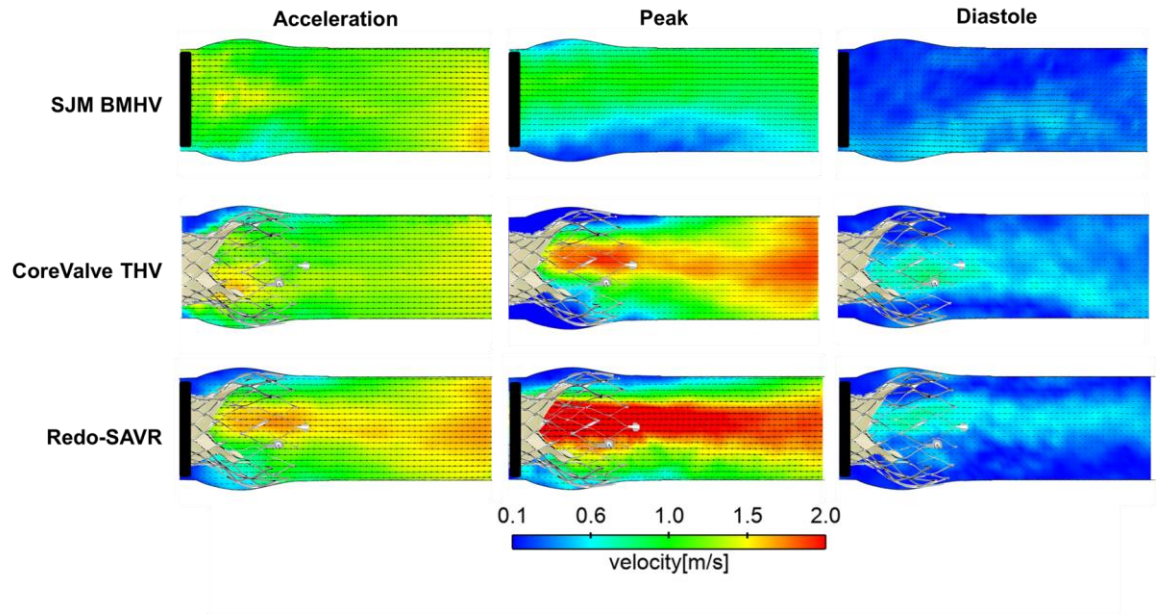

Figure 8.2. Phase-averaged velocity distribution for the SJM MHV, CoreValve THV and valve-in-MHV at CO=5 L/min.

Figure 8.4 shows the TKE, RSS, velocity vectors and vorticity contours at peak systole for the three configurations tested at 5 L/min. Similar patterns were found for the 3L/min configuration.

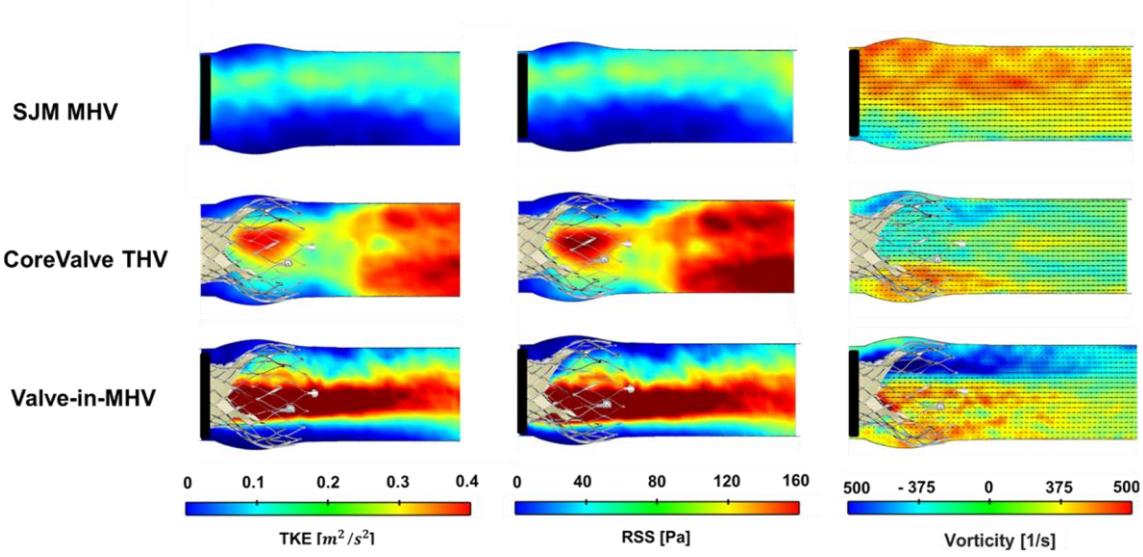

Figure 8.3. From left, TKE, RSS, velocity vectors and vorticity contours at 5L/min for SJM MHV, CoreValve and valve-in-MHV configurations.

At 5 L/min, the CoreValve and valve-in-MHV reached RSS values of 261 Pa and 377 Pa, respectively, and TKE values of 0.31 m^2/s^2 and 0.53 m^2/s^2, respectively. In contrast, the MHV had RSS and TKE values of 120 Pa and 0.26 m^2/s^2. High TKE values propagated conically

in the x-direction for the CoreValve THV and valve-in-MHV configurations, peaking near the valve opening and becoming more homogeneous further downstream, while the SJM MHV exhibited a skewed flow jet that impinged on the vessel wall, showing a dispersed distribution with the lowest magnitudes of both RSS and TKE.

8.4 Discussion

Backlight PIV was employed along with a pulse duplicator to assess the feasibility of valve-in-MHV procedure. The latter involved the surgical removal of pyrolytic carbon leaflets and subsequent implantation of the CoreValve THV in the metallic annulus.

Flow patterns were investigated to evaluate whether this configuration could reduce the need for anticoagulation therapy while improving hemodynamic performance. The primary finding of the study was that valve configuration have a main influence of the hemodynamic. Significant differences were found between the bileaflet valve, the THV and the valve-in-MHV configuration. The latter exhibited the highest mean and peak transvalvular pressure, and reduced EOA, resulting in more resistance opposed to the blood flow, increased turbulence and shear stresses possibly affecting the blood platelets and leading to platelet activation and thrombus formation. The distribution of RSS closely mirrored the velocity

and vorticity fields, with peak values occurring near the valve leaflets, where flow disturbances were most pronounced. These findings indicate that though the valve-in-MHV configuration provide a physiological flow pattern, as those of the bioprosthesis, it also may predispose the patient to increased risks of thrombotic events due to higher turbulence near the valve leaflets. The elevated pressure gradients, TKE (i.e., 1.5 folder) and reduced EOA, observed in the valve-in-MHV configuration can be explained by the limited expansion of the THV within the stiff metallic ring. The reduced sinus space provided by the ideal model and stiff material in the test bench further potentially contributed to the creation of flow stagnation regions. Our findings are consistent with those of Hatoum et al [173-175] who reported turbulent wakes impinging on the aortic walls and observed peaks in TKE and RSS for the CoreValve THV. These studies have shown that shear stress can exceed the 10–100 Pa range during peak systole, which is considered as the cut-off value of blood damage and thrombus formation risk [38]. After ViV procedures, the shear stress further increases 2- to 3-fold [176] to cause thrombus formation and hemolysis [177, 178]. In this study, increased flow velocity and turbulence in the valve-in-MHV configuration further highlight the need for careful consideration of device-device interactions and their hemodynamic consequences.

The principle of backlighting here implemented relied upon the employment of a LED source rather than a conventional laser. Though conventional PIV typically provides a precise measurement of flow filed within the thin lighted plane, its experimental set-up is costly, complex and hazardous to utilize. In contrast, our set-up illuminates a broader area, capturing shadows of particles across multiple layers, which can result in depth ambiguity and overlapping shadows, potentially providing averaged flow field estimations and less accurate characterization of flow patterns. However, the integrated backlight PIV-pulse duplicator system suggested in this work resulted particularly effective due to its ability to replicate the physiological conditions and provide an estimation of the hemodynamic performance in a cost-effective and versatile way.

Few studies have explored alternative PIV systems to conventional methods in the cardiovascular field. Recently, Bardi et al. [179] proposed a low-cost, LED-based PIV system to assess abdominal aortic flows using compliant, clear, ideal, and patient-specific aortic phantoms. Similarly, Torta and colleagues compared a conventional PIV system with a smartphone-based setup for the in-vitro characterization of fluid dynamics in realistic phantoms of healthy and diseased coronary arteries [180], emphasizing the growing trend to employ more sustainable technologies to assess cardiovascular flows.

From a clinical perspective, findings underscore the need for continued research to optimize heart valve therapies as valve-in-MHV procedure and reduce adverse hemodynamic effects. Although the study demonstrated that the valve-in-MHV configuration can provide a physiological flow pattern, the increased turbulence and reduced washout raise concerns about thrombotic risk and blood damage. Procedure optimization and improved patient selection are critical to improving outcomes and reducing the need for anticoagulation therapy. There is limited research on the in-vitro hemodynamics of ViV procedures [168, 175, 181, 182]. Existing studies indicated factors as device types, sizes, and implantation depths greatly affect the post-ViV hemodynamic. A thorough investigation of various combinations of device size and implantation depths is essential to fully understand the feasibility and outcomes of the valve-in-MHV procedure. By gaining a deeper understanding of the complex interplay between valve design, flow dynamics, and thrombogenicity, clinicians can make more informed decisions that enhance patient outcomes and minimize the risk of adverse This research contributes to the ongoing efforts to optimize valve interventions and improve long-term clinical outcomes in patients undergoing complex ViV procedures.

Chapter 9

Conclusions and Outlook

This research project sought to address critical challenges and broaden the understanding of transcatheter aortic valve implantation by instituting a novel computation model.

Given the state-the-art, the objective of this research focused on addressing key-limitations in patient-specific in-silico modeling and establishing trust in the developed TAVI simulation. To do so, an inverse material calibration was established to identify the most suitable patient-specific material descriptors for the analyzed population to adopt in the TAVI modeling. Additionally, the TAVI model here proposed strictly underwent at each level components verification and validation (V&V) activities according to requirements identified by ASME V&V 40. A quasi-automatic computational framework to model patient-specific TAVI scenarios derived from this work. The here developed workflow not only offer the opportunity to develop accurate patient-specific structural and fluid dynamic models of TAVI scenarios but also allow to perform it in the more time-effective way, resulting in a significant versatile tool that can be extended to various range of population and to a wider number of cases.

The utilization of transcatheter heart valves (THVs) in specific scenarios, including off-label applications, was also examined using computational and experimental methods, showcasing their efficacy in enhancing understanding of transcatheter therapies.

The principal findings of the thesis are reported hereafter:

Material parameters were obtained by an inverse calibration procedure customized for specific patient anatomies, guaranteeing that the model accurately represents the patient-specific mechanical properties of the aortic root and calcified valve leaflets starting from the assessment of the CT imaging. From a clinical perspective this is of utmost importance since a standard measurement for the clinical practice can lead to the patient-specific characterization of the tissue involved in the pathology investigated.

The model complied with the ASME V&V 40 standard for medical devices, integrating verification and validation operations throughout the development process for both the TAVI system and patient-specific platform. This guaranteed the model's credibility and reliability for clinical and regulatory applications. Outcomes from the FEA and FSI TAVI computational models exhibited minimal error margins relative to actual patient data,

validating the model's accuracy in accordance with the associated clinical risk. This degree of accuracy is essential for guiding pre-procedural planning and reducing adverse events.

Furthermore, the thesis offered novel insights into the "off-label" application of aortic transcatheter heart valves in the mitral position, employing patient-specific modeling and the advanced Left Heart Human Model (LHHM) to examine the trancatether mitral valve replacement (TMVR) performance related to the whole spectrum of patient cathegory as well as according to key implantation features.

The efficacy of a self-expandable THV within a bileaflet mechanical heart valve (MHV) annulus was assessed, yielding significant data for prospective clinical uses.

This research provides a robust basis for enhancing the comprehension of TAVI processes and directing the innovation of new devices, owing to the adaptability and accuracy of computational modeling. The patient-specific simulation platform developed in this study shows potential for improving clinical outcomes and expanding individualized treatment approaches in cardiovascular medicine. Posing a step-forward in the development and validation of patient-specific TAVI models.

However, some limitations must be recognized. The intricacy of fluid-structure interaction simulations and patient-specific modeling necessitates substantial processing resources, potentially constraining the broad implementation of these techniques in clinical practice. Future efforts should concentrate on enhancing the computational process to facilitate real-time or near-real-time clinical decision-making. Despite validation against actual patient data, the long-term durability of TAVI devices was neglected since no fatigue testing simulations were employed and this, especially in younger and lower-risk patients, necessitates more exploration. Although this study concentrated on a wide range of patient anatomies and scenarios, there always exists the potential to broaden the modeling framework to encompass more intricate cases, therefore enhancing the model's usefulness and robustness in clinical practice.

The incorporation of machine learning techniques may augment the predictive capacities of the models, facilitating immediate and more precise projections of patient outcomes. This may assist in the advancement of real-time decision assistance systems for healthcare professionals. In conclusion, although problems remain, the findings of this thesis signify a significant advancement in enhancing the reliability of TAVI techniques via sophisticated computational modeling. Future work must concentrate on addressing existing constraints

and broadening the applicability of these models to a wider array of clinical situations, thereby enhancing patient outcomes and encouraging innovation in cardiovascular care.

List of Publications

Peer-reviewed Article

1. **Catalano, C**., Agnese, V., Gentile, G., Raffa, G. M., Pilato, M., & Pasta, S. (2022). Atlas-based evaluation of hemodynamic in ascending thoracic aortic aneurysms. Applied Sciences-Basel, 12(1). https://doi.org/ARTN 39410.3390/app12010394
2. **Catalano, C**., Cannata, S., Agnese, V., Gentile, G., Gandolfo, C., & Pasta, S. (2023). On the spectrum of transcatheter mitral valve replacement: in silico and in vitro assessment of neo-LVOT area in ViR, ViV and ViMAC. Bioprinting, 32, e00285.
3. **Catalano, C**., & Pasta, S. (2022). On the modeling of transcatheter therapies for the aortic and mitral valves: a review. Prosthesis, 4(1), 102 - 112.
4. **Catalano, C**., Turgut, T., Zahalka, O., Götzen, N., Cannata, S., Gentile, G., Agnese, V., Gandolfo, C., & Pasta, S. (2024). On the material constitutive behavior of the aortic root in patients with transcatheter aortic valve implantation. Cardiovascular Engineering and Technology, 15(1), 95-109.
5. Pasta, S., **Catalano, C**., Cannata, S., Guccione, J. M., & Gandolfo, C. (2022). Numerical simulation of transcatheter mitral valve replacement: The dynamic implication of LVOT obstruction in the valve-in-ring case. Journal of Biomechanics, 144. https://doi.org/ARTN 11133710.1016/j.jbiomech.2022.111337
6. Pasta, S., **Catalano, C**., Crascì, F., & Scuoppo, R. (2023). A custom-built planar biaxial system for soft tissue material testing. HardwareX, 16, e00475.
7. **Catalano, C**., Crascì, F., Puleo, S., Scuoppo, R., Pasta, S., & Raffa, G. M. (2024). Computational fluid dynamics in cardiac surgery and perfusion: A review. Perfusion, 02676591241239277.
8. **Catalano, C**., Turgut, T., Zhalka, O., Götzen, N., Cannata, S., Gentile, G., Agnese, V., Gandolfo, C., & Pasta, S. (2024). Establishing in-silico credibility of patient-specific finite-element model in a virtual cohort. In Lecture Notes in Computational Vision and Biomechanics (Vol. 39, pp. 311-318). https://doi.org/10.1007/978-3-031-55315-8_34

Conference Paper

1. **Catalano, C**., Cannata, S., Agnese, V., Buffa, G., Fratini, L., Pasta, S., & Gandolfo, C. (2022). 3D printing and computational modeling for the evaluation of LVOT obstruction in transcatheter mitral valve replacement. V Cirp Conference on Biomanufacturing, 110, 273-278. https://doi.org/10.1016/j.procir.2022.06.049
2. **Catalano, C**., Cannata, S., Gandolfo, C., & Pasta, S. (2023a). Establishing computational modeling credibility in patients undergoing TAVI. Eighth National Congress of Bioengineering–Proceedings 2023.
3. **Catalano, C**., Cannata, S., Gandolfo, C., & Pasta, S. (2023b). An inverse analysis for the assessment of material properties of TAVI patients. Eighth National Congress of Bioengineering–Proceedings 2023.
4. Zahalka, O., Catalano, C., Turgut, T., Gotzen, N., Cannata, S., Gandolfo, C., & Pasta, S. (2023). Mechanical properties of polyamide 12 for the use in balloon- expandable transcatheter heart valves. Eighth National Congress of Bioengineering–Proceedings 2023.
5. **Catalano, C**., Zahalka, O., Turgut, T., Bouwman, V., & Pasta, S., (2024). Fluid-structure interaction simulation of transcatheter aortic valve implantation using smoothed particle hydrodynamics. Nineth European Congress on Computational Methods in Applied Sciences and Engineering – ECCOMAS Congress 2024.

Appendix

Details on numerical verification for the patient-specific TAVI structural simulation.

Time increment

Run number	Time scaling factor	Wall-clock time	Aortic Valve Area	Maximum Principal Strain	Maximum Principal Stress
1	0.4	29584	104.58	0.150	3.64
2	0.6	21122	104.50	0.149	3.63
3	0.8	16711	104.59	0.150	3.64
4	1.0	11203	104.57	0.149	3.64
5	1.2	20126	104.57	0.149	3.63

Relative error Aortic valve area vs CT area	Relative error maximum principal strain	Relative error maximum principal stress
0.24%	0.06%	0.00%
0.16%	0.00%	0.19%
0.25%	0.06%	0.19%
0.23%	0.00%	0.05%
0.24%	0.00%	0.19%

Mass Scaling

Run number	Mass Scaling	Wall-clock time	Aortic Valve Area	Maximum Principal Strain	Maximum Principal Stress
6	5.00E-06	257	99.98	0.119	1.593
7	1.00E-06	1255	104.34	0.148	1.959
8	5.00E-07	2437	104.56	0.149	1.976
9	1.00E-07	11262	104.60	0.149	1.973
10	5.00E-08	12429	104.59	0.149	1.973
11	1.00E-08	12855	104.59	0.149	1.973

Relative error Aortic valve area vs CT area	Relative error maximum principal strain	Relative error maximum principal stress
4.17%	20.68%	19.260%
0.01%	1.07%	0.710%
0.22%	0.07%	0.152%
0.26%	0.00%	0.000%
0.25%	0.00%	0.000%
0.25%	0.00%	0.000%

Material Damping

Run number	Material Damping	Wall-clock time	Aortic Valve Area	Maximum Principal Strain	Maximum Principal Stress
12	100	1290	104.58	0.1499	1.973
13	250	1097	104.57	0.1499	1.973

14	500	1246	104.58	0.1499	1.973
15	1000	1095	104.54	0.1498	1.971
16	2000	12262	104.54	0.1496	1.969

Relative error Aortic valve area vs CT area	Relative error maximum principal strain	Relative error maximum principal stress
0.241%	0.000%	0.000%
0.233%	0.000%	0.000%
0.238%	0.000%	0.000%
0.205%	0.067%	0.101%
0.205%	0.200%	0.203%

Viscous Pressure

Run number	Viscous Pressure Magnitude	Wall-clock time	Aortic Valve Area	Maximum Principal Strain	Maximum Principal Stress
17	0.00000301	1243	104.408652	0.149	1.965
18	6.01E-06	1278	104.239175	0.149	1.957
19	1.20E-05	1446	103.908726	0.147	1.941
20	2.40E-05	1248	103.257429	0.145	1.911
21	3.01E-05	1223	102.936291	0.144	1.895

Relative error Aortic valve area vs CT area	Relative error maximum principal strain	Relative error maximum principal stress
0.075%	0.400%	0.405%
0.087%	0.801%	0.811%
0.404%	1.668%	1.622%
1.028%	3.269%	3.142%
1.336%	4.069%	3.953%

Bulk Viscosity

Run number	Bulk Viscosity	Wall-clock time	Aortic Valve Area	Maximum Principal Strain	Maximum Principal Stress
22	0	11351	104.61	0.1497	1.977
23	0.03	11208	104.59	0.1499	1.974
24	0.09	13007	104.59	0.1499	1.973
25	0.6	22787	104.62	0.1499	1.967

Relative error Aortic valve area vs CT area	Relative error maximum principal strain	Relative error maximum principal stress
0.266%	0.133%	0.203%
0.250%	0.000%	0.051%
0.245%	0.000%	0.000%
0.276%	0.000%	0.304%

Friction Coefficient

Run number	Friction Coefficient	Wall-clock time	Aortic Valve Area	Maximum Principal Strain	Maximum Principal Stress
26	0	1235	104.590	0.1499	1.973
27	0.1	1285	104.591	0.1496	1.973
28	0.2	1349	104.575	0.1493	1.971
29	0.4	1332	104.534	0.1486	1.968

Relative error Aortic valve area vs CT area	Relative error maximum principal strain	Relative error maximum principal stress
0.249%	0.000%	0.000%
0.250%	0.200%	0.000%
0.235%	0.400%	0.101%
0.196%	0.867%	0.253%

Details on numerical verification for the patient-specific TAVI SPH simulations

Particle Size

Particle Size [mm]	Aortic Vel. [m/s]	Rel.Err. [%]	PG [mmHg]	Rel.Err. [%]	GOA [mm^2]	Rel.Err. [%]	EOA [mm^2]	Rel.Err. [%]
0.9 mm	3.53	-	49.84	-	206.40	-	169.84	-
1.15 mm	3.42	3.68	46.24	7.23	217.95	5.60	175.65	3.42
1.4 mm	3.14	12.18	38.44	22.88	221.75	7.44	176.79	4.08
1.7 mm	3.41	3.40	46.51	6.68	234.87	13.79	173.25	2.00

Mass Scaling

Mass Scaling [s]	Aortic Vel. [m/s]	Rel.Err. [%]	PG [mmHg]	Rel.Err. [%]	GOA [mm^2]	Rel.Err. [%]	EOA [mm^2]	Rel.Err. [%]
1.0e-6	3.53	-	49.84	-	206.40	-	169.84	-
5.0e-7	2.73	22.66	29.82	10.48	206.02	0.10	173.28	2.02
2.5e-6	3.13	11.33	39.19	21.38	208.12	0.83	175.05	3.06

Viscous Pressure

Viscous Pressure [MPa]	Aortic Vel. [m/s]	Rel.Err. [%]	PG [mmHg]	Rel.Err. [%]	GOA [mm^2]	Rel.Err. [%]	EOA [mm^2]	Rel.Err. [%]
1.4e-5	3.53	-	49.84	-	206.40	-	169.84	-
1.0e-6	3.27	7.37	42.77	14.19	209.73	1.61	180.44	6.23
1.4e-6	3.34	22.66	44.62	10.48	206.02	0.18	171.94	1.23

Bibliography

1. Cribier, A., et al., *Percutaneous transcatheter implantation of an aortic valve prosthesis for calcific aortic stenosis: first human case description. Circulation, 2002.* **106**(24): p. 3006-3008.
2. Chin, W.C. and J.A. Chin, *Biofluids Modeling: Methods, Perspectives, and Solutions*. 2023: Wiley-Scrivener, Bevery, USA.
3. Murillo, H., et al. *Imaging of the aorta: embryology and anatomy. in Seminars in Ultrasound*, CT and MRI. 2012. Elsevier.
4. Bissell, M.M., E. Dall'Armellina, and R.P. Choudhury, *Flow vortices in the aortic root: in vivo 4D-MRI confirms predictions of Leonardo da Vinci*. European heart journal, 2014. **35**(20): p. 1344-1344.
5. Fung, Y.C., *Biomechanics: Motion, Flow, Stress and Growth*, ed. N.Y. Springer Verlag. 1990.
6. Zipes, D.P., *Braunwald's heart disease e-book: A textbook of cardiovascular medicine*. 2018: Elsevier Health Sciences.
7. Nishimura, R.A., *Aortic valve disease*. Circulation, 2002. **106**(7): p. 770-772.
8. Vahanian, A., et al., *2021 ESC/EACTS Guidelines for the management of valvular heart disease: Developed by the Task Force for the management of valvular heart disease of the European Society of Cardiology (ESC) and the European Association for Cardio-Thoracic Surgery (EACTS).* European Journal of Cardio-Thoracic Surgery, 2021. **60**(4): p. 727-800.
9. Iung, B. and A. Vahanian, *Epidemiology of valvular heart disease in the adult*. Nat Rev Cardiol, 2011. **8**(3): p. 162-72.
10. Moncla, L.-H.M., et al., *Calcific aortic valve disease: mechanisms, prevention and treatment*. Nature Reviews Cardiology, 2023. **20**(8): p. 546-559.
11. Aikawa, E. and F.J. Schoen, *Calcific and degenerative heart valve disease, in Cellular and molecular pathobiology of cardiovascular disease*. 2014, Elsevier. p. 161-180.
12. Aikawa, E. and P. Libby, *A rock and a hard place: chiseling away at the multiple mechanisms of aortic stenosis*. 2017, Am Heart Assoc. p. 1951-1955.
13. Siu, S.C. and C.K. Silversides, *Bicuspid aortic valve disease*. Journal of the American College of Cardiology, 2010. **55**(25): p. 2789-2800.
14. Michelena, H.I., et al., *Bicuspid aortic valve: identifying knowledge gaps and rising to the challenge from the International Bicuspid Aortic Valve Consortium (BAVCon)*. Circulation, 2014. **129**(25): p. 2691-704.
15. Yutzey, K.E., et al., *Calcific aortic valve disease: a consensus summary from the Alliance of Investigators on Calcific Aortic Valve Disease*. Arteriosclerosis, thrombosis, and vascular biology, 2014. **34**(11): p. 2387-2393.
16. Verma, S. and S.C. Siu, *Aortic dilatation in patients with bicuspid aortic valve*. N Engl J Med, 2014. **370**(20): p. 1920-9.
17. Marijon, E., et al., *Rheumatic heart disease*. The Lancet, 2012. **379**(9819): p. 953- 964.
18. Vojacek, J., P. Zacek, and J. Dominik, *Aortic regurgitation*. 2018: Springer.
19. Bekeredjian, R. and P.A. Grayburn, *Valvular heart disease: aortic regurgitation*. Circulation, 2005. **112**(1): p. 125-134.

20. Baumgartner, H., et al., *Echocardiographic assessment of valve stenosis: EAE/ASE recommendations for clinical practice. European Journal of Echocardiography*, 2009. **10**(1): p. 1-25.
21. Thoenes, M., et al., *Patient screening for early detection of aortic stenosis (AS)—review of current practice and future perspectives*. Journal of thoracic disease, 2018. **10**(9): p. 5584.
22. Rajiah, P., et al., *Multimodality imaging of complications of cardiac valve surgeries*. Radiographics, 2019. **39**(4): p. 932-956.
23. Cannegieter, S., F. Rosendaal, and E. Briet, *Thromboembolic and bleeding complications in patients with mechanical heart valve prostheses*. Circulation, 1994. **89**(2): p. 635-641.
24. Tam, D.Y., et al., *Surgical valve selection in the era of transcatheter aortic valve replacement in the Society of Thoracic Surgeons Database*. The Journal of thoracic and cardiovascular surgery, 2020. **159**(2): p. 416-427. e8.
25. Sellers, S.L., et al., *Transcatheter Aortic Heart Valves Histological Analysis Providing Insight to Leaflet Thickening and Structural Valve Degeneration.* Jacc-Cardiovascular Imaging, 2019. **12**(1): p. 135-145.
26. Dasi, L.P., et al., *Fluid mechanics of artificial heart valves*. Clinical and experimental pharmacology and physiology, 2009. **36**(2): p. 225-237.
27. Huded, C., et al., *TCT-50 Incidence and Prognostic Significance of Heart Failure Hospitalization After Transcatheter or Surgical Aortic Valve Replacement: Results From the PARTNER Trials*. Journal of the American College of Cardiology, 2021. **78**(19_Supplement_S): p. B20-B20.
28. Leon, M.B., et al., *Transcatheter aortic-valve implantation for aortic stenosis in patients who cannot undergo surgery*. N Engl J Med, 2010. **363**(17): p. 1597-607.
29. Van Mieghem, N.M., et al., *Self-expanding transcatheter vs surgical aortic valve replacement in intermediate-risk patients: 5-year outcomes of the SURTAVI randomized clinical trial*. JAMA cardiology, 2022. **7**(10): p. 1000-1008.
30. Reardon, M.J., et al., *Surgical or transcatheter aortic-valve replacement in intermediate-risk patients*. New England journal of medicine, 2017. **376**(14): p. 1321-1331.
31. Rodés-Cabau, J., et al., *Transcatheter or surgical aortic valve replacement in patients with severe aortic stenosis and small aortic annulus: a randomized clinical trial*. Circulation, 2024. **149**(9): p. 644-655.
32. Thyregod, H.G.H., et al., *Transcatheter or surgical aortic valve implantation: 10-year outcomes of the NOTION trial*. European Heart Journal, 2024: p. ehae043.
33. Vinayak, M., et al*., Transcatheter Aortic Valve Replacement: Current Status and Future Indications*. Journal of Clinical Medicine, 2024. **13**(2): p. 373.
34. Van Belle, E., et al., *Balloon-expandable versus self-expanding transcatheter aortic valve replacement: a propensity-matched comparison from the FRANCE-TAVI registry.* Circulation, 2020. **141**(4): p. 243-259.
35. Braghiroli, J., et al., *Transcatheter aortic valve replacement in low risk patients: a review of PARTNER 3 and Evolut low risk trials*. Cardiovasc Diagn Ther, 2020. **10**(1): p. 59-71.

36. Frerker, C., S. Baldus, and S. Nitschmann, *[Transcatheter aortic valve replacement: PARTNER 3 trial and Evolut Low Risk Trial].* Internist (Berl), 2019. **60**(11): p. 1221-1224.
37. Claessen, B.E., et al., *Considerations for optimal device selection in transcatheter aortic valve replacement: a review*. JAMA cardiology, 2021. **6**(1): p. 102-112.
38. Dasi, L.P., et al., *On the mechanics of transcatheter aortic valve replacement*. Annals of biomedical engineering, 2017. **45**: p. 310-331.
39. Catalano, C., et al., *Computational fluid dynamics in cardiac surgery and perfusion: A review.* Perfusion, 2024: p. 02676591241239277.
40. Catalano, C. and S. Pasta, *On the Modeling of Transcatheter Therapies for the Aortic and Mitral Valves: A Review*. Prosthesis, 2022. **4**(1): p. 102 - 112.
41. Randall, M.H. and A.A. Bavry, *Update on transcatheter aortic valve replacement.*Cardiology and therapy, 2020. 9(1): p. 75-84.
42. Muñoz, A. and J.J. Gómez-Doblas, *Patient selection for TAVI.*
43. Kim, W.-K., et al., *Incidence and outcome of peri-procedural transcatheter heart valve embolization and migration: the TRAVEL registry (TranscatheteR HeArt Valve EmboLization and Migration)*. European heart journal, 2019. **40**(38): p. 3156-3165.
44. Hayashida, K., et al., *Potential mechanism of annulus rupture during transcatheter aortic valve implantation*. Catheterization and Cardiovascular Interventions, 2013. **82**(5): p. E742-E746.
45. Dowling, C., S. Firoozi, and S.J. Brecker, *First-in-Human Experience With Patient- Specific Computer Simulation of TAVR in Bicuspid Aortic Valve Morphology*. JACC Cardiovasc Interv, 2020. **13**(2): p. 184-192.
46. Lavon, K., et al., *Biomechanical modeling of transcatheter aortic valve replacement in a stenotic bicuspid aortic valve: deployments and paravalvular leakage*. Med Biol Eng Comput, 2019. **57**(10): p. 2129-2143.
47. Mao, W., et al., *Numerical Parametric Study of Paravalvular Leak Following a Transcatheter Aortic Valve Deployment Into a Patient-Specific Aortic Root*. J Biomech Eng, 2018. **140**(10).
48. Ghosh, R.P., et al., *Numerical evaluation of transcatheter aortic valve performance during heart beating and its post-deployment fluid-structure interaction analysis*. Biomech Model Mechanobiol, 2020. **19**(5): p. 1725-1740.
49. Bianchi, M., et al., *Patient-specific simulation of transcatheter aortic valve replacement: impact of deployment options on paravalvular leakage*. Biomech Model Mechanobiol, 2019. **18**(2): p. 435-451.
50. Basri, A.A., et al., *Fluid structure interaction on paravalvular leakage of transcatheter aortic valve implantation related to aortic stenosis: a patient-specific case.* Computational and mathematical methods in medicine, 2020. 2020.
51. Pasta, S., et al., *Simulation study of transcatheter heart valve implantation in patients with stenotic bicuspid aortic valve.* Med Biol Eng Comput, 2020.
52. Bosi, G.M., et al., *A validated computational framework to predict outcomes in TAVI.m*Scientific reports, 2020. **10**(1): p. 1-11.

53. Rocatello, G., et al., *Optimization of a transcatheter heart valve frame using patient- specific computer simulation*. Cardiovascular engineering and technology, 2019. **10**(3): p. 456-468.
54. Finotello, A., et al., *Finite element analysis of transcatheter aortic valve implantation: Insights on the modelling of self-expandable devices*. Journal of the Mechanical Behavior of Biomedical Materials, 2021. **123**: p. 104772.
55. Bailey, J., N. Curzen, and N.W. Bressloff, *Assessing the impact of including leaflets in the simulation of TAVI deployment into a patient-specific aortic root*. Comput Methods Biomech Biomed Engin, 2016. **19**(7): p. 733-44.
56. Pasta, S. and C. Gandolfo, *Computational Analysis of Self-Expanding and Balloon- Expandable Transcatheter Heart Valves*. Biomechanics, 2021. **1**(1): p. 43-52.
57. Nappi, F., et al., *CoreValve vs. Sapien 3 transcatheter aortic valve replacement: a finite element analysis study*. Bioengineering, 2021. **8**(5): p. 52.
58. Luraghi, G., et al., *On the Modeling of Patient-Specific Transcatheter Aortic Valve Replacement: A Fluid-Structure Interaction Approach*. Cardiovasc Eng Technol, 2019. **10**(3): p. 437-455.
59. Pasta, S., et al., *Transcatheter Heart Valve Implantation in Bicuspid Patients with Self-Expanding Device*. Bioengineering, 2021. **8**(7): p. 91.
60. Scuoppo, R., et al., *Parametric analysis of transcatheter aortic valve replacement in transcatheter aortic valve replacement: evaluation of coronary flow obstruction*. Front Bioeng Biotechnol, 2023. **11**: p. 1267986.
61. Caballero, A., et al., *Modeling Left Ventricular Blood Flow Using Smoothed Particle Hydrodynamics*. Cardiovasc Eng Technol, 2017. **8**(4): p. 465-479.
62. Mao, W., K. Li, and W. Sun, *Fluid-Structure Interaction Study of Transcatheter Aortic Valve Dynamics Using Smoothed Particle Hydrodynamics*. Cardiovasc Eng Technol, 2016. **7**(4): p. 374-388.
63. Brouwer, J., et al., *Insight on patient specific computer modeling of transcatheter aortic valve implantation in patients with bicuspid aortic valve disease*. Catheter Cardiovasc Interv, 2018.
64. Dowling, C., et al., *Patient-specific computer simulation of transcatheter aortic valve replacement in bicuspid aortic valve morphology*. Circulation: Cardiovascular Imaging, 2019. **12**(10): p. e009178.
65. Catalano, C., et al. *An Inverse Analysis for the Assessment of Material Properties of TAVI Patients*. in Eighth National Congress of Bioengineering–Proceedings 2023. 2023. Patron Editore Srl.
66. Bosi, G.M., et al., *Population-specific material properties of the implantation site for transcatheter aortic valve replacement finite element simulations*. Journal of biomechanics, 2018. **71**: p. 236-244.
67. Xu, F., et al., *Computational investigation of left ventricular hemodynamics following bioprosthetic aortic and mitral valve replacement*. Mechanics Research Communications, 2021. **112**: p. 103604.
68. Wald, S., A. Liberzon, and I. Avrahami*, A numerical study of the hemodynamic effect of the aortic valve on coronary flow*. Biomechanics and modeling in mechanobiology, 2018. **17**(2): p. 319-338.

69. Sun, W., W. Mao, and B.E. Griffith, *Computer modeling and simulation of heart valve function and intervention, in Principles of Heart Valve Engineering*. 2019, Elsevier. p. 177-211.
70. Scuoppo, R., et al. *Structural Simulation of Transcatheter Heart Valve in Transcatheter Heart Valve*. in EIGHTH NATIONAL CONGRESS OF BIOENGINEERING Proceedings. 2023. http://gnb2023. it/proceedings. html.
71. Lluch, È., et al., *Breaking the state of the heart: meshless model for cardiac mechanics*. Biomechanics and modeling in mechanobiology, 2019. **18**: p. 1549-1561.
72. Laha, S., et al., *Smoothed particle hydrodynamics based FSI simulation of the native and mechanical heart valves in a patient-specific aortic model*. Scientific Reports, 2024. **14**(1): p. 6762.
73. Bruno, A.G., et al., *Predicting and improving outcomes of transcatheter aortic valve replacement in older adults and the elderly*. Expert review of cardiovascular therapy, 2020. **18**(10): p. 663-680.
74. Généreux, P., et al., *Clinical outcomes after transcatheter aortic valve replacement using valve academic research consortium definitions: a weighted meta-analysis of 3,519 patients from 16 studies*. Journal of the American College of Cardiology, 2012. **59**(25): p. 2317-2326.
75. Généreux, P., et al., *Paravalvular leak after transcatheter aortic valve replacement: the new Achilles' heel? A comprehensive review of the literature.* Journal of the American College of Cardiology, 2013. **61**(11): p. 1125-1136.
76. Mas-Peiro, S., et al., *Current issues in transcatheter aortic valve replacement*. Journal of thoracic disease, 2020. **12**(4): p. 1665.
77. Luraghi, G., et al., *The impact of calcification patterns in transcatheter aortic valve performance: a fluid-structure interaction analysis*. Computer Methods in Biomechanics and Biomedical Engineering, 2020: p. 1-9.
78. Prisco, A.R., et al., *The native aortic valve reduces paravalvular leak in TAVR patients*. Front Physiol, 2022. **13**: p. 910016.
79. Heitkemper, M., et al., *Modeling risk of coronary obstruction during transcatheter aortic valve replacement*. The Journal of thoracic and cardiovascular surgery, 2020. **159**(3): p. 829-838. e3.
80. Chen, Y.H., et al., *Membranous septum length predicts conduction disturbances following transcatheter aortic valve replacement*. J Thorac Cardiovasc Surg, 2022. **164**(1): p. 42-51 e2.
81. Hamdan, A., et al., *Short membranous septum length in bicuspid aortic valve stenosis increases the risk of conduction disturbances*. J Cardiovasc Comput Tomogr, 2021. **15**(4): p. 339-347.
82. McGee, O.M., et al., *The impact of implantation depth of the Lotus™ valve on mechanical stress in close proximity to the bundle of His. Biomechanics and modeling in mechanobiology*, 2019. **18**(1): p. 79-88.
83. Rocatello, G., et al., *Patient-Specific Computer Simulation to Elucidate the Role of Contact Pressure in the Development of New Conduction Abnormalities After Catheter-Based Implantation of a Self-Expanding Aortic Valve*. Circ Cardiovasc Interv, 2018. **11**(2): p. e005344.

84. Yoon, S.H., et al., *Outcomes in Transcatheter Aortic Valve Replacement for Bicuspid Versus Tricuspid Aortic Valve Stenosis*. J Am Coll Cardiol, 2017. **69**(21): p. 2579- 2589.
85. Perlman, G.Y., et al., *Bicuspid Aortic Valve Stenosis: Favorable Early Outcomes With a Next-Generation Transcatheter Heart Valve in a Multicenter Study*. JACC Cardiovasc Interv, 2016. **9**(8): p. 817-824.
86. Viceconti, M., et al., *In silico trials: Verification, validation and uncertainty quantification of predictive models used in the regulatory evaluation of biomedical products*. Methods, 2021. **185**: p. 120-127.
87. V40, A., *Assessing credibility of computational modeling through verification and validation: application to medical devices*. The American Society of Mechanical Engineers, 2018.
88. Mulugeta, L., et al., *Credibility, replicability, and reproducibility in simulation for biomedicine and clinical applications in neuroscience*. Frontiers in Neuroinformatics, 2018. **12**: p. 18.
89. Steinman, D.A. and F. Migliavacca, *Special issue on verification, validation, and uncertainty quantification of cardiovascular models: towards effective vvuq for translating cardiovascular modelling to clinical utility*. Cardiovascular engineering and technology, 2018. **9**(4): p. 539-543.
90. Luraghi, G., F. Migliavacca, and J.F.R. Matas, *Study on the accuracy of structural and FSI heart valves simulations*. Cardiovascular engineering and technology, 2018. **9**(4): p. 723-738.
91. Tango, A.M., et al., *Validation and extension of a fluid–structure interaction model of the healthy aortic valve*. Cardiovascular engineering and technology, 2018. **9**(4): p. 739-751.
92. Yazdi, S.G., et al., *A review of arterial phantom fabrication methods for flow measurement using PIV techniques*. Annals of biomedical engineering, 2018. **46**(11): p. 1697-1721.
93. Cosentino, F., et al., *Statistical Shape Analysis of Ascending Thoracic Aortic Aneurysm: Correlation between Shape and Biomechanical Descriptors*. J Pers Med, 2020. **10**(2).
94. Scardulla, F., et al., *Shear stress alterations in the celiac trunk of patients with a continuous-flow left ventricular assist device as shown by in-silico and in-vitro flow analyses*. J Heart Lung Transplant, 2017. **36**(8): p. 906-913.
95. Krishnan, K., et al., *Ascending thoracic aortic aneurysm wall stress analysis using patient-specific finite element modeling of in vivo magnetic resonance imaging*. Interact Cardiovasc Thorac Surg, 2015. **21**(4): p. 471-80.
96. Pasta, S., et al., *Three-dimensional parametric modeling of bicuspid aortopathy and comparison with computational flow predictions*. Artif Organs, 2017. **41**(9): p. E92- E102.
97. Kronzon, I., et al., *Optimal Imaging for Guiding TAVR: Transesophageal or Transthoracic Echocardiography, or Just Fluoroscopy*? JACC: Cardiovascular Imaging, 2015. **8**(3): p. 361-370.
98. Auricchio, F., et al., *Simulation of transcatheter aortic valve implantation: a patient- specific finite element approach*. Comput Methods Biomech Biomed Engin, 2014. **17**(12): p. 1347-57.

99. Capelli, C., et al., P*atient-specific simulations of transcatheter aortic valve stent implantation.* Med Biol Eng Comput, 2012. **50**(2): p. 183-92.
100. Attinger-Toller, A., et al., *Age-Related Outcomes After Transcatheter Aortic Valve Replacement*. Jacc-Cardiovascular Interventions, 2021. **14**(9): p. 952-960.
101. Catalano, C., et al., *On the Material Constitutive Behavior of the Aortic Root in Patients with Transcatheter Aortic Valve Implantation*. Cardiovascular Engineering and Technology, 2024. **15**(1): p. 95-109.
102. Trabelsi, O., et al., *Predictive Models with Patient Specific Material Properties for the Biomechanical Behavior of Ascending Thoracic Aneurysms*. Ann Biomed Eng, 2016. **44**(1): p. 84-98.
103. Di Giuseppe, M., et al., *Identification of circumferential regional heterogeneity of ascending thoracic aneurysmal aorta by biaxial mechanical testing*. J Mol Cell Cardiol, 2019. **130**: p. 205-215.
104. Azadani, A.N., et al., *Comparison of mechanical properties of human ascending aorta and aortic sinuses*. Ann Thorac Surg, 2012. **93**(1): p. 87-94.
105. Martin, C., T. Pham, and W. Sun, *Significant differences in the material properties between aged human and porcine aortic tissues*. Eur J Cardiothorac Surg, 2011. **40**(1): p. 28-34.
106. Catalano, C., et al. *Verification and validation of transcatheter heart valve implantation in a virtual human cohort*. in *18th International Symposium on Computer Methods in Biomechanics and Biomedical Engineering*. 2023. Paris (FR).
107. Catalano, C., et al. *Establishing In-silico Credibility of Patient-Specific Finite-Element Model in a Virtual Cohort*. *in International Symposium on Computer Methods in Biomechanics and Biomedical Engineering*. 2023. Springer.
108. V, A. and V. 10-, *Guide for verification and validation in computational solid mechanics*. 2006, Performance Test Codes Standards Committee.
109. Aldieri, A., et al., *Credibility assessment of computational models according to ASME V&V40: Application to the Bologna biomechanical computed tomography solution*. Computer Methods and Programs in Biomedicine, 2023. **240**: p. 107727.
110. Catalano, C., et al., *Atlas-Based Evaluation of Hemodynamic in Ascending Thoracic Aortic Aneurysms*. Applied Sciences-Basel, 2022. **12**(1).
111. Monaghan, J.J., *Smoothed particle hydrodynamics*. In: Annual review of astronomy and astrophysics. Vol. **30** (A93-25826 09-90), p. 543-574., 1992. 30: p. 543-574.
112. Monaghan, J., *Smoothed particle hydrodynamics and its diverse applications*. Annual Review of Fluid Mechanics, 2012. **44** p. 323–46.
113. 5840-1:2021, I., *Cardiovascular implants—Cardiac valve prostheses—Part 1:General requirements* in *International Organization for Standardization*. 2021: Geneva, Switzerland.
114. Pathmanathan, P., et al., *Applicability analysis of validation evidence for biomedical computational models. Journal of Verification, Validation and Uncertainty Quantification*, 2017. **2**(2): p. 021005.
115. Sutera, S.P. and R. Skalak, *The history of Poiseuille's law. Annual review of fluid mechanics*, 1993. **25**(1): p. 1-20.

116. Ramella, A., et al., *Applicability assessment for in-silico patient-specific TEVAR procedures*. J Biomech, 2023. **146**: p. 111423.
117. Catalano, C., et al., *On the spectrum of transcatheter mitral valve replacement: In silico and in vitro assessment of neo-LVOT area in ViR, ViV and ViMAC*. Bioprinting, 2023. **32**: p. e00285.
118. Pasta, S., et al., *Numerical simulation of transcatheter mitral valve replacement: The dynamic implication of LVOT obstruction in the valve-in-ring case.* J Biomech, 2022. **144**: p. 111337.
119. Castillo-Sang, M., et al., *Outcomes of repeat mitral valve surgery in patients with pulmonary hypertension*. Innovations (Phila), 2015. **10**(2): p. 120-4.
120. Babaliaros, V.C., et al., *The Art of SAPIEN 3 Transcatheter Mitral Valve Replacement in Valve-in-Ring and Valve-in-Mitral-Annular-Calcification Procedures*. JACC Cardiovasc Interv, 2021. **14**(20): p. 2195-2214.
121. Muller, D.W.M., et al., *2-Year Outcomes of Transcatheter Mitral Valve Replacement in Patients With Severe Symptomatic Mitral Regurgitation*. J Am Coll Cardiol, 2021. **78**(19): p. 1847-1859.
122. Guerrero, M., et al., *Transcatheter Mitral Valve Replacement in Native Mitral Valve Disease With Severe Mitral Annular Calcification: Results From the First Multicenter Global Registry*. JACC Cardiovasc Interv, 2016. **9**(13): p. 1361-71.
123. Paradis, J.M., et al., *Transcatheter Valve-in-Valve and Valve-in-Ring for Treating Aortic and Mitral Surgical Prosthetic Dysfunction*. Journal of the American College of Cardiology, 2015. **66**(18): p. 2019-2037.
124. Yoon, S.H., et al., *Transcatheter Mitral Valve Replacement for Degenerated Bioprosthetic Valves and Failed Annuloplasty Rings*. J Am Coll Cardiol, 2017. **70**(9): p. 1121-1131.
125. Blanke, P., et al., *Predicting LVOT Obstruction in Transcatheter Mitral Valve Implantation: Concept of the Neo-LVOT*. JACC Cardiovasc Imaging, 2017. **10**(4): p. 482-485.
126. Alsidawi, S., et al., *Significant LVOT obstruction after mitral valve in ring procedure*. Eur Heart J Cardiovasc Imaging, 2015. **16**(12): p. 1389.
127. Eleid, M.F., et al., *Percutaneous Transvenous Transseptal Transcatheter Valve Implantation in Failed Bioprosthetic Mitral Valves, Ring Annuloplasty, and Severe Mitral Annular Calcification*. JACC Cardiovasc Interv, 2016. **9**(11): p. 1161-74.
128. Bapat, V., et al., *Early Experience With New Transcatheter Mitral Valve Replacement*. J Am Coll Cardiol, 2018. **71**(1): p. 12-21.
129. Reid, A., et al., *Neo-LVOT and Transcatheter Mitral Valve Replacement: Expert Recommendations*. JACC Cardiovasc Imaging, 2021. **14**(4): p. 854-866.
130. Yoon, S.H., et al., *Predictors of Left Ventricular Outflow Tract Obstruction After Transcatheter Mitral Valve Replacement*. JACC Cardiovasc Interv, 2019. **12**(2): p. 182-193.
131. Kohli, K., et al., *Transcatheter Mitral Valve Planning and the Neo-LVOT: Utilization of Virtual Simulation Models and 3D Printing*. Curr Treat Options Cardiovasc Med, 2018. **20**(12): p. 99.

132. Catalano, C., et al., *3D Printing and Computational Modeling for the Evaluation of LVOT obstruction in Transcatheter Mitral Valve Replacement*. V Cirp Conference on Biomanufacturing, 2022. **110**: p. 273-278.
133. Pasta, S., et al., *CAD Modeling for Evaluating LVOT Obstruction in Transcatheter Mitral Valve Replacement*. Lecture Notes in Mechanical Engineering, 2020: p. 776- 787.
134. Pasta, S., et al., *Simulation of left ventricular outflow tract (LVOT) obstruction in transcatheter mitral valve-in-ring replacement*. Med Eng Phys, 2020. **82**: p. 40-48.
135. De Vecchi, A., et al., *Left ventricular outflow obstruction predicts increase in systolic pressure gradients and blood residence time after transcatheter mitral valve replacement*. Sci Rep, 2018. **8**(1): p. 15540.
136. Lifesciences, E*., Edwards SAPIEN 3 Transcatheter Heart Valve with the Edwards Commander System 23 / 26 / 29 mm Sizes - Procedural Training Manual*. 2015.
137. Pasta, S. and C. Gandolfo, *Pre-Operative Modeling of Transcatheter Mitral Valve Replacement in a Surgical Heart Valve Bioprosthesis*. Prosthesis, 2020. **2**(1): p. 39- 45.
138. Pasta, S., et al., *Numerical simulation of transcatheter mitral valve replacement: The dynamic implication of LVOT obstruction in the valve-in-ring case*. Journal of Biomechanics, 2022. **144**.
139. Cutugno, S., et al., *Patient-Specific Analysis of Ascending Thoracic Aortic Aneurysm with the Living Heart Human Model*. Bioengineering-Basel, 2021. **8**(11).
140. Holzapfel, G.A. and R.W. Ogden, *Constitutive modelling of passive myocardium: a structurally based framework for material characterization*. Philos Trans A Math Phys Eng Sci, 2009. **367**(1902): p. 3445-75.
141. Walker, J.C., et al., *MRI-based finite-element analysis of left ventricular aneurysm*. American Journal of Physiology-Heart and Circulatory Physiology, 2005. **289**(2): p. H692-H700.
142. Guccione, J.M., L.K. Waldman, and A.D. McCulloch, *Mechanics of active contraction in cardiac muscle: Part II--Cylindrical models of the systolic left ventricle*. J Biomech Eng, 1993. **115**(1): p. 82-90.
143. Morganti, S., et al*., Prediction of patient-specific post-operative outcomes of TAVI procedure: The impact of the positioning strategy on valve performance*. J Biomech, 2016. **49**(12): p. 2513-9.
144. Mao, W., et al., *Fully-coupled fluid-structure interaction simulation of the aortic and mitral valves in a realistic 3D left ventricle model*. PLoS One, 2017. **12**(9): p. e0184729.
145. Morganti, S., et al., *Simulation of transcatheter aortic valve implantation through patient-specific finite element analysis: Two clinical cases*. Journal of Biomechanics, 2014. **47**(11): p. 2547-2555.
146. D'Ancona, G., et al., *Haemodynamic predictors of a penetrating atherosclerotic ulcer rupture using fluid-structure interaction analysis*. Interact Cardiovasc Thorac Surg, 2013. **17**(3): p. 576-8.
147. Baillargeon, B., et al., *The Living Heart Project: A robust and integrative simulator for human heart function*. Eur J Mech A Solids, 2014. **48**: p. 38-47.

148. Guccione, J.M., et al., *Myosplint decreases wall stress without depressing function in the failing heart: a finite element model study*. Ann Thorac Surg, 2003. **76**(4): p. 1171-80; discussion 1180.
149. May-Newman, K. and F.C. Yin, *Biaxial mechanical behavior of excised porcine mitral valve leaflets*. Am J Physiol, 1995. **269**(4 Pt 2): p. H1319-27.
150. Kunzelman, K.S., et al., *Finite element analysis of the mitral valve*. J Heart Valve Dis, 1993. **2**(3): p. 326-40.
151. Ooms, J.F., et al., *Computed Tomography-Derived 3D Modeling to Guide Sizing and Planning of Transcatheter Mitral Valve Interventions*. Jacc-Cardiovascular Imaging, 2021. **14**(8): p. 1644-1658.
152. Wang, D.D., et al., *Validating a prediction modeling tool for left ventricular outflow tract (LVOT) obstruction after transcatheter mitral valve replacement (TMVR).* Catheterization and Cardiovascular Interventions, 2018. **92**(2): p. 379-387.
153. Wang, D.D., et al*., Predicting LVOT Obstruction After TMVR*. JACC Cardiovasc Imaging, 2016. **9**(11): p. 1349-1352.
154. Kohli, K., et al., *Assessing the Hemodynamic Impact of Anterior Leaflet Laceration in Transcatheter Mitral Valve Replacement: An in silico Study.* Front Cardiovasc Med, 2022. **9**: p. 869259.
155. de Jaegere, P., et al., *Patient-Specific Computer Modeling for the Planning of Transcatheter Mitral Valve Replacement*. J Am Coll Cardiol, 2018. **72**(8): p. 956-958.
156. Hill, S.J., et al., *Patient-specific fluid simulation of transcatheter mitral valve replacement in mitral annulus calcification*. Front Cardiovasc Med, 2022. **9**: p. 934305.
157. Glaser, N., et al., *Loss in life expectancy after surgical aortic valve replacement: SWEDEHEART study*. Journal of the American College of Cardiology, 2019. **74**(1):p. 26-33.
158. Patel, P.M., et al., *Isolated redo aortic valve replacement versus valve-in-valve transcatheter valve replacement*. The Annals of Thoracic Surgery, 2021. **112**(2): p. 539-545.
159. Yoganathan, A.P., Z. He, and S. Casey Jones, *Fluid mechanics of heart valves*. Annu. Rev. Biomed. Eng., 2004. **6**: p. 331-362.
160. Alperi, A., S. Garcia, and J. Rodes-Cabau, *Transcatheter valve-in-valve implantation in degenerated surgical aortic and mitral bioprosthesis: Current state and future perspectives*. Progress in Cardiovascular Diseases, 2022. **72**: p. 54-65.
161. Quinlan, N.J. and P.N. Dooley, *Models of flow-induced loading on blood cells in laminar and turbulent flow, with application to cardiovascular device flow*. Annals of biomedical engineering, 2007. **35**: p. 1347-1356.
162. Becsek, B., L. Pietrasanta, and D. Obrist, *Turbulent systolic flow downstream of a bioprosthetic aortic valve: velocity spectra, wall shear stresses, and turbulent dissipation rates*. Frontiers in physiology, 2020. **11**: p. 577188.
163. Midha, P.A., et al., *The Fluid Mechanics of Transcatheter Heart Valve Leaflet Thrombosis in the Neosinus*. Circulation, 2017. **136**(17): p. 1598-1609.

164. Raghav, V., et al., *Transcatheter aortic valve thrombosis: a review of potential mechanisms*. Journal of the Royal Society Interface, 2021. **18**(184): p. 20210599.
165. Hatoum, H., et al., *Impact of patient-specific morphologies on sinus flow stasis in transcatheter aortic valve replacement: an in vitro study*. The Journal of thoracic and cardiovascular surgery, 2019. **157**(2): p. 540-549.
166. Jahren, S.E., et al., *Aortic root stiffness affects the kinematics of bioprosthetic aortic valves*. Interactive cardiovascular and thoracic surgery, 2017. **24**(2): p. 173-180.
167. Hasler, D. and D. Obrist, *Three-dimensional flow structures past a bio-prosthetic valve in an in-vitro model of the aortic root*. PloS one, 2018. **13**(3): p. e0194384.
168. Midha, P.A., et al., *Valve type, size, and deployment location affect hemodynamics in an in vitro valve-in-valve model*. JACC: Cardiovascular Interventions, 2016. **9**(15): p. 1618-1628.
169. Stamhuis, E. and W. Thielicke, *PIVlab–towards user-friendly, affordable and accurate digital particle image velocimetry in MATLAB*. Journal of open research software, 2014. **2**(1): p. 30.
170. Giersiepen, M., et al., *Estimation of shear stress-related blood damage in heart valve prostheses-in vitro comparison of 25 aortic valves*. The International journal of artificial organs, 1990. **13**(5): p. 300-306.
171. Morbiducci, U., et al., *Blood damage safety of prosthetic heart valves. Shear-induced platelet activation and local flow dynamics: A fluid–structure interaction approach*. Journal of Biomechanics, 2009. **42**(12): p. 1952-1960.
172. Gunning, P.S., T.J. Vaughan, and L.M. McNamara, *Simulation of self expanding transcatheter aortic valve in a realistic aortic root: implications of deployment geometry on leaflet deformation*. Annals of biomedical engineering, 2014. **42**: p. 1989-2001.
173. Hatoum, H., et al., *Flow dynamics of surgical and transcatheter aortic valves: Past to present*. JTCVS open, 2022. **9**: p. 43-56.
174. Hatoum, H., et al., *In-vitro characterization of self-expandable textile transcatheter aortic valves*. Journal of the mechanical behavior of biomedical materials, 2020. **103**:p. 103559.
175. Hatoum, H., et al., *The hemodynamics of transcatheter aortic valves in transcatheter aortic valves*. J Thorac Cardiovasc Surg, 2021. **161**(2): p. 565-576 e2.
176. Hatoum, H., et al., *The hemodynamics of transcatheter aortic valves in transcatheter aortic valves*. Journal of Thoracic and Cardiovascular Surgery, 2021. **161**(2): p. 565.
177. Rosseel, L., O. De Backer, and L. Søndergaard, *Clinical valve thrombosis and subclinical leaflet thrombosis following transcatheter aortic valve replacement: is there a need for a patient-tailored antithrombotic therapy?* Frontiers in cardiovascular medicine, 2019. **6**: p. 44.
178. Marwan, M., et al., *Leaflet thrombosis following transcatheter aortic valve implantation*. Journal of cardiovascular computed tomography, 2018. **12**(1): p. 8-13.

179. Bardi, F., et al., *A hybrid mock circulatory loop integrated with a LED-PIV system for the investigation of AAA compliant phantoms*. Frontiers in Bioengineering and Biotechnology, 2024. **12**: p. 1452278.
180. Torta, E., et al., *Smartphone-based particle tracking velocimetry for the in vitro assessment of coronary flows*. Medical Engineering & Physics, 2024. **126**: p. 104144.
181. Hatoum, H., et al., *Impact of leaflet laceration on transcatheter aortic valve-in-valve washout: BASILICA to solve neosinus and sinus stasis*. JACC: Cardiovascular Interventions, 2019. **12**(13): p. 1229-1237.
182. Midha, P.A., et al., *The effect of valve-in-valve implantation height on sinus flow*. Annals of biomedical engineering, 2017. **45**: p. 405-412.